Dunkelflaute events: characterization, prediction and future projection

Dunkelflaute events: characterization, prediction and future projection

Proefschrift

ter verkrijging van de graad van doctor
aan de Technische Universiteit Delft,
op gezag van de Rector Magnificus prof. dr. ir. T.H.J.J. van der Hagen,
voorzitter van het College voor Promoties,
in het openbaar te verdedigen op
dinsdag 4 Februari 2025 om 10.00 uur

door

Bowen LI

Master of Engineering in Hydraulic Engineering,
Tsinghua University, China,
geboren te Liaoning, China.

Dit proefschrift is goedgekeurd door de promotoren

Prof. dr. Sukanta Basu
Prof. dr. S.J. Watson
Prof. dr. H.W.J. Russchenberg

Samenstelling promotiecommissie:

Rector Magnificus,	voorzitter
Prof. dr. Sukanta Basu,	University at Albany, USA
Prof. dr. S.J. Watson,	Technische Universiteit Delft
Prof. dr. H.W.J. Russchenberg,	Technische Universiteit Delft
Onafhankelijke leden:	
Prof. dr. D.A. von Terzi,	Technische Universiteit Delft
Prof. dr. A. Estanqueiro,	Renewable Energy and Energy Systems Integration Unit of LNEG, Portugal
Prof. dr. G. Harrison,	University of Edinburgh, UK
Prof. dr. J. Reuder,	University of Bergen, Norway

Keywords: Dunkelflaute, wind energy, solar energy, machine learning

Printed by:

Cover:

ISBN 979-8-89686-668-8

An electronic version of this dissertation is available at
`http://repository.tudelft.nl/`.

To my families.

Bowen Li

Contents

Summary

Dunkelflaute, meaning "dark doldrums" in German, denotes prolonged periods characterized by low wind and solar energy production, attributed to overcast skies and calm weather conditions. With wind and solar power assuming increasingly crucial roles within the European energy landscape, these extreme weather conditions (Dunkelflaute events) pose a significant challenge to grid stability. Addressing this challenge in power production, the objective of this dissertation is to comprehensively analyze Dunkelflaute events and devise both physical and machine learning-based methodologies for their prediction. The research goal is approached through three key aspects: 1) conducting a statistical analysis of the frequency, duration, seasonal variations, and associated weather patterns of Dunkelflaute events to gain insights into their impact and underlying characteristics; 2) developing diverse strategies for the identification and prediction of these events from both a modelling and data availability standpoint to enhance predictability; and 3) projecting future weather patterns under climate change scenarios and investigate the impact of climate changes on this extreme weather.

The first aspect of the study delves into the statistical analysis and internal features of Dunkelflaute events within a region encompassing eleven Northern European countries. Utilizing power production data from Renewables.ninja, as well as actual data from TSOs, key characteristics such as frequency, duration, and seasonal effects of Dunkelflaute were identified. Dunkelflaute events were classified based on specific criteria (both wind and solar capacity factors below 0.2 and duration longer than 1h), leading to the discovery of 5-10 prolonged events lasting more than 1 day in Germany, Norway, and the UK, with some events enduring up to 5 days. The winter season was found to host the highest frequency of Dunkelflaute events, with durations ranging from 50 to 100 hours per month. Using the ERA5 reanalysis dataset, meteorological drivers behind Dunkelflaute events such as large stationary high-pressure systems and extensive low cloud coverage were identified. These blocked regimes originating from the extensive high-pressure systems can disrupt airflow, particularly affecting wind power production in Northern European countries. Additionally, a simulated grid connection highlighted the importance of system stability during Dunkelflaute events, emphasizing the potential benefits of interconnecting European grid systems to mitigate such occurrences.

The second aspect of the study focuses on the identification and prediction of Dunkelflaute events. The introduction of the WISRnet deep learning framework incorporated a CNN-AE model for weather pattern downscaling and a region-based k-means model for automating Dunkelflaute related pattern clustering. Validated with aggregated wind and solar power production data from Belgium, this strategy showcased promising results. Furthermore, the application of the WRF model in simulating atmospheric conditions during Dunkelflaute events demonstrated its effectiveness in predicting wind power production and insolation changes. Lastly, a LightGBM-based approach was proposed for estimating wind and solar power production during Dunkelflaute events. With a comprehensive range of input vari-

ables considered (such as wind speed, insolation, boundary layer height and sensible heat flux), the LightGBM model surpassed other machine learning models including RF and XGBoost and physical models like WRF, providing accurate and reliable power production estimations during Dunkelflaute events.

The third aspect of the study explores the influence of climate change on Dunkelflaute events. By projecting future weather patterns and simulating various emission scenarios, enhancements were made to the WISRnet model. This refined model now effectively clusters projected wind speed and insolation patterns to identify Dunkelflaute events. It was observed that the frequency of future Dunkelflaute events is greatly influenced by the different emission scenarios. Specifically, under the negative emission scenario RCP2.6, Dunkelflaute frequency exhibits a negative trend, while both weak and strong emission scenarios show positive trends. These results underscore the noticeable impact of climate change on the occurrence of Dunkelflaute events, highlighting the importance of integrating climate considerations into future grid planning.

In summary, this dissertation makes a major contribution by enhancing comprehension of Dunkelflaute events and proposing three distinct identification and prediction methodologies: Firstly, the introduction of an unsupervised deep learning framework, WISRnet, enables effective clustering of Dunkelflaute related patterns and event identification. Secondly, a WRF model-based approach is employed to emulate atmospheric conditions and predict Dunkelflaute events. Lastly, a LightGBM-based approach is utilized to estimate wind and solar power production during Dunkelflaute events, offering accurate and reliable insights into power generation dynamics during such occurrences.

Samenvatting

Dunkelflaute, wat "donkere windstiltes"betekent in het Duits, duidt op langdurige periodes gekenmerkt door lage wind- en zonne-energieproductie, toegeschreven aan bewolkte luchten en rustig weer. Met wind- en zonne-energie die steeds crucialere rollen aannemen binnen het Europese energielandschap, vormen deze extreme weersomstandigheden (Dunkelflaute gebeurtenissen) een aanzienlijke uitdaging voor de stabiliteit van het elektriciteitsnet. Om deze uitdaging in de stroomproductie aan te pakken, is het doel van deze dissertatie om Dunkelflaute gebeurtenissen uitgebreid te analyseren en zowel fysieke als op machine learning gebaseerde methodologieën te bedenken voor hun voorspelling. Het onderzoeksdoel wordt benaderd via drie belangrijke aspecten: 1) het uitvoeren van een statistische analyse van de frequentie, duur, seizoensvariaties en bijbehorende weerspatronen van Dunkelflaute gebeurtenissen om inzicht te krijgen in hun impact en onderliggende kenmerken; 2) het ontwikkelen van diverse strategieën voor de identificatie en voorspelling van deze gebeurtenissen vanuit zowel een modellerings- als gegevensbeschikbaarheidsoogpunt om voorspelbaarheid te verbeteren; en 3) het projecteren van toekomstige weerspatronen onder klimaatveranderingsscenario's en onderzoeken van de impact van klimaatverandering op dit extreme weer.

Het eerste aspect van de studie duikt in de statistische analyse en interne kenmerken van Dunkelflaute gebeurtenissen binnen een regio die elf Noord-Europese landen omvat. Door gebruik te maken van de energieproductiegegevens van Renewables.ninja, evenals werkelijke gegevens van TSO's, werden belangrijke kenmerken zoals frequentie, duur en seizoenseffecten van Dunkelflaute geïdentificeerd. Dunkelflaute gebeurtenissen werden geclassificeerd op basis van specifieke criteria (zowel wind- als zonnecapaciteitsfactoren onder 0,2 en een duur langer dan 1 uur), wat leidde tot de ontdekking van 5-10 langdurige gebeurtenissen die langer dan 1 dag aanhielden in Duitsland, Noorwegen en het Verenigd Koninkrijk, waarbij sommige gebeurtenissen tot 5 dagen duurden. Het winterseizoen bleek de hoogste frequentie van Dunkelflaute gebeurtenissen te hebben, met duur variërend van 50 tot 100 uur per maand. Met behulp van de ERA5-heranalyse dataset werden meteorologische factoren achter Dunkelflaute gebeurtenissen zoals grote stationaire hogedrukgebieden en uitgebreide bewolkte luchten geïdentificeerd. Deze geblokkeerde regimes afkomstig van uitgebreide hogedrukgebieden kunnen de luchtstroom verstoren en met name de windenergieproductie in Noord-Europese landen beïnvloeden. Daarnaast benadrukte een gesimuleerde netwerkaansluiting het belang van systeemstabiliteit tijdens Dunkelflaute gebeurtenissen, waarbij de potentiële voordelen van het koppelen van Europese netwerksystemen benadrukt werden om dergelijke gebeurtenissen te verzachten.

Het tweede aspect van de studie richt zich op de identificatie en voorspelling van Dunkelflaute gebeurtenissen. De introductie van het WISRnet diep leernetwerkincorporeerde een CNN-AE model voor het verkleinen van weerspatronen en een op regio gebaseerd k-means model voor het automatiseren van het clusteren van Dunkelflaute gerelateerde patronen. Gevalideerd met geaggregeerde wind- en zonne-energieproductiegegevens uit

België, toonde deze strategie veelbelovende resultaten. Verder toonde de toepassing van het WRF-model bij het simuleren van atmosferische omstandigheden tijdens Dunkelflaute gebeurtenissen de effectiviteit ervan aan in het voorspellen van windenergieproductie en veranderingen in zonnestraling. Ten slotte werd een op LightGBM gebaseerde aanpak voorgesteld voor het schatten van wind- en zonne-energieproductie tijdens Dunkelflaute gebeurtenissen. Met een uitgebreid scala aan overwogen invoervariabelen (zoals windsnelheid, zonnestraling, grenslaaghoogte en sensibele warmtestroom) overtrof het LightGBM-model andere machine learning modellen, waaronder RF en XGBoost, en fysische modellen zoals WRF, met nauwkeurige en betrouwbare schattingen van de energieproductie tijdens Dunkelflaute gebeurtenissen.

Het derde aspect van de studie onderzoekt de invloed van klimaatverandering op Dunkelflaute gebeurtenissen. Door toekomstige weerspatronen te projecteren en verschillende emissiescenario's te simuleren, zijn verbeteringen aangebracht in het WISRnet-model. Dit verfijnde model cluster nu effectief geprojecteerde windsnelheid- en instralingspatronen om Dunkelflaute gebeurtenissen te identificeren. Er werd opgemerkt dat de frequentie van toekomstige Dunkelflaute gebeurtenissen sterk beïnvloed wordt door de verschillende emissiescenario's. Specifiek vertoont de Dunkelflaute frequentie onder het negatieve emissiescenario RCP2.6 een negatieve trend, terwijl zowel zwakke als sterke emissiescenario's positieve trends tonen. Deze resultaten benadrukken de merkbare impact van klimaatverandering op het voorkomen van Dunkelflaute gebeurtenissen en onderstrepen het belang van het integreren van klimaatoverwegingen in toekomstige netplanning.

Samenvattend draagt deze dissertatie aanzienlijk bij aan het begrip van Dunkelflaute gebeurtenissen en stelt drie verschillende methodologieën voor identificatie en voorspelling voor: Ten eerste maakt de introductie van een ongesuperviseerd diep-leer-raamwerk, WISRnet, effectieve clustering van Dunkelflaute gerelateerde patronen en gebeurtenisherkenning mogelijk. Ten tweede wordt een aanpak gebaseerd op het WRF-model gebruikt om atmosferische omstandigheden na te bootsen en Dunkelflaute gebeurtenissen te voorspellen. Ten slotte wordt een aanpak gebaseerd op LightGBM gebruikt om de productie van wind- en zonne-energie tijdens Dunkelflaute gebeurtenissen te schatten, waardoor nauwkeurige en betrouwbare inzichten worden geboden in de dynamiek van energieopwekking tijdens dergelijke gebeurtenissen.

Acknowledgments

As I approach the completion of my PhD journey, I reflect on the extensive learning and growth I have experienced throughout these years. I am deeply grateful to all those who have supported and guided me along the way. Their encouragement, assistance, and insights have been invaluable in helping me navigate the challenges of my research and academic endeavors.

First and foremost, I want to express my heartfelt gratitude to Professor Sukanta Basu, my esteemed promoter and supervisor, for his unwavering support and guidance throughout my PhD journey. His exceptional expertise and insightful feedback have been instrumental in shaping my research and enhancing my academic development. I am deeply thankful for the countless hours he devoted to mentoring me, always encouraging me to think critically and creatively. Our engaging discussions often sparked new ideas and directions for my work, pushing me to expand my horizons. Professor Basu's passion for research and dedication to his students have been a true source of inspiration, motivating me to strive for excellence in my endeavors. During challenging times, his patience and understanding were a comforting presence that kept me focused. I am profoundly grateful for his belief in my potential and his steadfast commitment to my success. This journey would not have been possible without his guidance, and I consider it a privilege to have worked under his supervision. I look forward to carrying the knowledge and skills I have gained into my future career, always inspired by his exceptional mentorship.

My special thanks to my promoter, Professor Simon J. Watson for his invaluable support and guidance throughout my PhD journey. His expertise and insightful feedback have been essential in shaping my research and fostering my academic growth. I greatly appreciate the very detailed comments and feedback he provided for my work, which has made a lasting impact on my academic career.

I like to express my heartfelt gratitude to my promoter, Professor Herman W.J. Russchenberg, for his unwavering support throughout my academic journey. During the challenging times of the COVID-19 pandemic, his caring nature inspired me and helped me persevere. I greatly appreciate the time and attention he invested in guiding me and my peers through these unprecedented times.

I like to take a moment to express my deep gratitude to my fellow graduate students: Bedassa, Weiran Li, Hongyang Ma, Han Dun, Hao Zhang, Antoon, Adriaan, Pouriya, Max, Harish, Serken, Yi Dai, Yan Yuan, Yuqing Wang, Weilun Qin, and Chengyu Yin. Each of you has played an invaluable role in making this journey memorable and enriching. Our shared experiences have fostered a sense of camaraderie that I cherish deeply. Your kindness and support during tough times, especially during the uncertainties brought by the pandemic, have meant a lot to me. Together, we have celebrated milestones and navigated challenges, forging bonds that I hope will last well beyond our academic pursuits. I appreciate all the laughter, encouragement, and shared knowledge along the way. It has been a privilege to work alongside each of you, and I look forward to seeing all the amazing things you will

achieve in the future. Thank you for making this journey not just a learning experience, but a truly enjoyable one.

I to extend my gratitude to my friends during my PhD journey in the Netherlands: Aihui Fu, Yuexiang Chen, Qing Yong, Erqian Tang, Xuan Chen, Zhengwei Wu, Yun Wan, Jin Chang, Lu Cheng, Ze Chang, Li Wang, Ying Wu, Zhang Pan, Chunyan He, and Peiyan Liu. You have been an incredible source of support and encouragement throughout this rigorous yet rewarding experience. Our shared laughter and moments of joy have made the challenges of PhD life much more bearable. I have learned so much from each of you, both academically and personally, enriching my experience in ways I never imagined. I truly appreciate the kindness and understanding you've shown during tough times, especially when balancing the demands of research and life. As we all move forward in our careers, I will cherish the memories we've created together. Thank you for being such wonderful friends and for making my PhD journey an unforgettable adventure. I look forward to seeing where our paths will take us next and celebrating our future successes together!

Most importantly, I would like to express my gratitude to my family for their unwavering support and encouragement. Their belief in my abilities helped me stay motivated during the challenging times. Their sacrifices and understanding during my times of stress have not gone unnoticed, and I am truly grateful for their love. I am incredibly fortunate to have such a supportive family who believed in me every step of the way.

I would like to take this opportunity to express my deepest love and gratitude to my husband, Yang Jin, with whom I have shared seven wonderful years of love and companionship. We first met as master's students, embarking on this journey together to the Netherlands, where we discovered our shared goals. Over these years, we have studied, worked, traveled, and enjoyed countless moments together. We've built a life filled with joy and adventure as we embraced the journey of marriage and shared experiences. His unwavering support has been my anchor throughout this challenging journey. No matter how disheartened I felt by challenging scientific results or emotional ups and downs, Yang has always been my source of strength, offering unwavering understanding, patience, and support. The warmth of his love has provided me with the comfort and motivation to keep pushing forward. Together, we have navigated the highs and lows of this journey, and his presence has made all the difference. I am incredibly appreciative of his presence in my life. I will cherish our bond for all the years to come, and I look forward to a future filled with love and success. Thank you for being my partner, my confidant, and my greatest supporter.

The arrival of our son will be an incredibly exciting milestone for Yang and me, as we eagerly await his arrival next April. We look forward to welcoming him into our lives and nurturing him to be a healthy, happy and responsible man in the future. This new chapter brings us immense joy and anticipation, and we are ready to embrace the adventures of parenthood together. Our hearts are filled with gratitude for this precious gift, and we can't wait to share our lives with him.

In conclusion, I am profoundly grateful for the support and encouragement I have received from everyone who has been part of my PhD journey. As I move forward, I carry with me the cherished memories made along the way.

Bowen
Delft, December 2024

1

Introduction

1

1.1 Background & Context

Transitioning to renewable energy sources is a crucial aspect of global efforts to promote energy sustainability. The Paris Agreement, which was signed in the course of the 21st Conference of the Parties (COP21) in 2015, marks a significant milestone toward a more sustainable energy future. The agreement aims to control the increase in global temperature to 1.5-2°C up above pre-industrial scales and encourage the adoption of renewable and sustainable economic practices [1, 2]. To support these endeavors, the European Commission has established the 2030 Framework for Climate and Energy [3] and the European Green Deal (EGD) [4] (as shown in Fig. 1.1), which seek to reduce greenhouse gas (GHG) emissions by at least 40% by 2030 and ultimately achieve a net-zero GHG emission economy by 2050. This transition to renewable sources is a significant step, with the objective of Europe attaining worldwide leadership in renewable energies [5], with at least 32% renewable source share of the whole energy consumption by 2030. This involves significant investment in wind and solar power parks, with the expectation that they will contribute at least 80% of electricity production by 2050 [6].

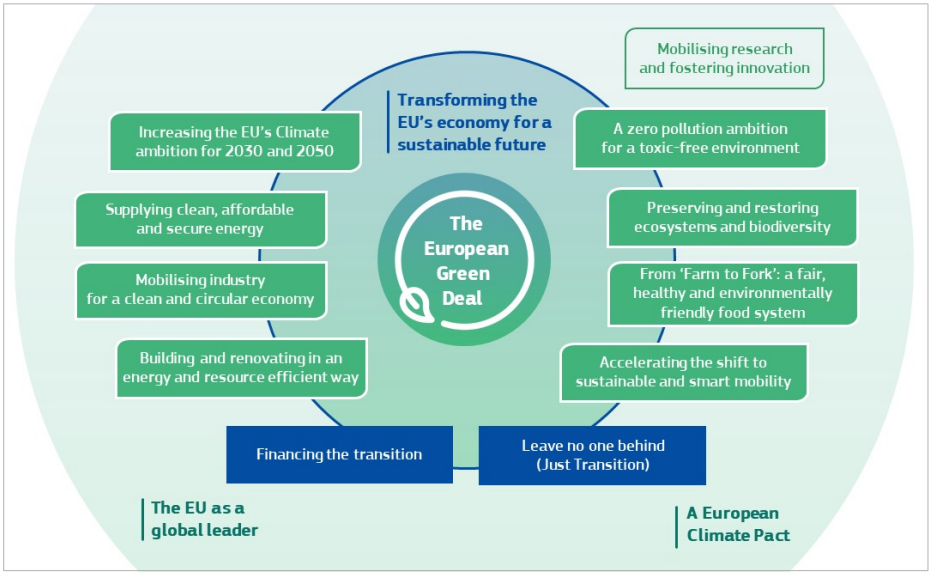

Figure 1.1: European green deal. [4]

In Europe, the use of renewable energy sources has been steadily increasing, with renewable energy contributing an increasing proportion of the region's energy consumption. From 2004 to 2018, the share of renewable sources as a fraction of the whole energy consumption in Europe rose from 9.6% to 18.9% [7]. In 2019, renewable energy accounted for approximately 20% of energy consumption [8]. This trend continued in 2020, with

renewable energy sources, particularly wind and solar, generating more electricity (40%) than fossil fuels (34%) [9, 10]. During this time, the European Union has achieved the second largest installed capacity (511.6 GW) of renewable energy globally [11]. A significant portion of this capacity is derived from wind and solar power, with installed solar power growing from 71.5 GW in 2012 to 160.4 GW and wind power growing from 97.2 GW to 187.5 GW over the same period. These trends highlight the impressive growth of renewable energy sources in Europe, particularly wind and solar energy. Offshore wind power, in particular, has recorded significant growth. Figure 1.2 shows the trends in offshore wind power growth in Europe for the period 2010–2020.

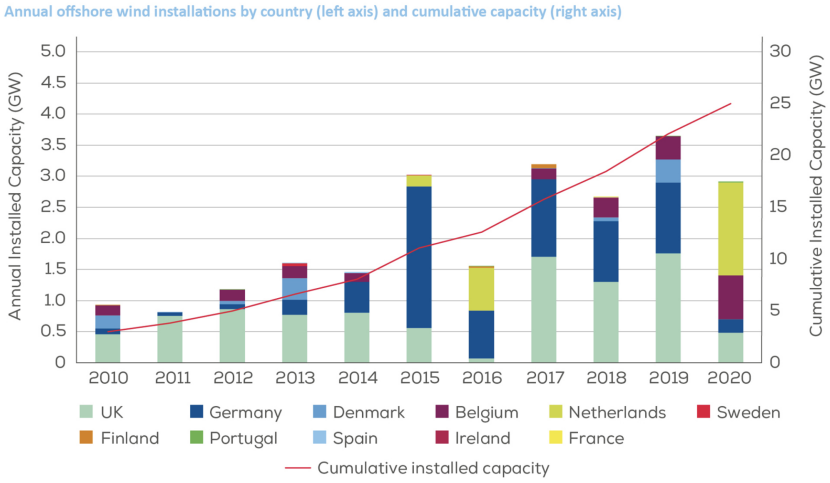

Figure 1.2: Offshore wind power installed capacity trend during the period 2010–2020. [12]

The North Sea Region (NSR), i.e. the North Sea and that part of north-western Europe bordering the North Sea, will play a crucial role in the energy transition. The NSR is energy-intensive due to its relatively dense population and the fact that it accounts for approximately 60% of the EU's GDP. Following its previous reliance on the oil and gas industry [13, 14], the NSR now plans to exploit the considerable potential for various renewable energy sources to decarbonize the region [15]. For instance, it is expected that at least 180GW of offshore wind parks will be installed in the NSR to meet the EU's targets [16]. This development has also led to several major transmission grid projects, such as the North Seas Countries' Offshore Grid Initiative (NSCOGI) in 2010 [17] and the North Seas Energy Cooperation (NSEC) in 2016 [18], to support the decarbonization plan.

The energy transition in the NSR has already led to a decrease of approximately 10% in greenhouse gas (GHG) emissions per decade from 1990 to the present. The NSR countries are committed to advancing this pace even further. They propose even more ambitious goals than the 40% reduction in GHG emissions (except 35% from Belgium) from 1990 levels advised by the EU. For example, the goals range from 49% for the Netherlands, 55% for Germany, 68% for the UK, and 70% for Denmark. By 2050, Belgium, the Netherlands, and Norway have ambitious plans to achieve 95% reductions in emissions, while Denmark,

1

Germany, Sweden, and the UK expect net-zero emissions [19]. To achieve the goals, Fig. 1.3 shows the energy mix for different scenarios in 2050.

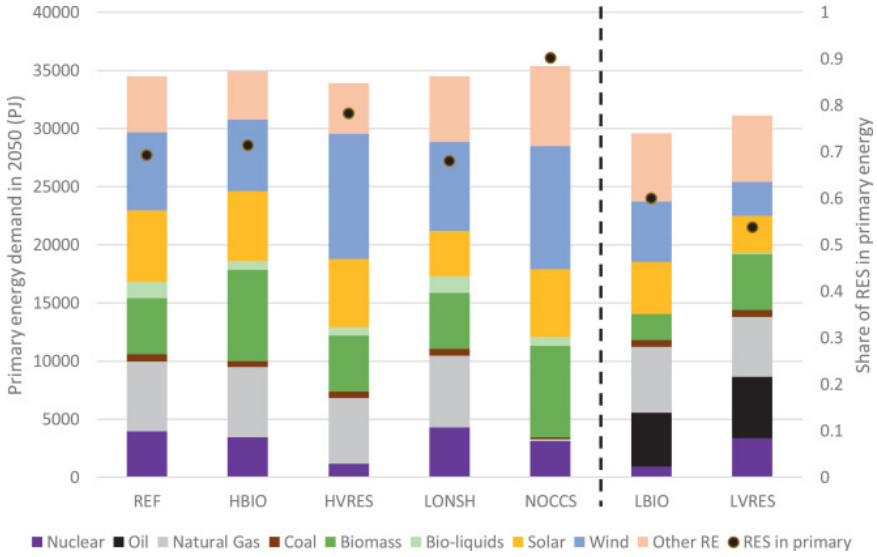

Figure 1.3: Primary energy mix in the NSR for selected scenarios in 2050. [19]

1.2 Dunkelflaute

Deploying wind and solar power plants is crucial for the energy transition. Despite the numerous benefits of these renewable sources, their power production is highly variable and not fully predictable, which can lead to significant challenges for grid operators. Due to the increasing penetration of these renewable sources and the decreasing presence of conventional generators, the electricity grid relies more on the weather and climate conditions [20, 21, 22, 23]. This intermittency, variability, and limited predictability, can cause challenges for load balancing and increase the risk of blackouts at the grid scale, increasing the burden on the grid operator.

The term 'Dunkelflaute' refers to long periods when both wind and solar energy production are significantly low due to cloudy and calm weather conditions [24, 25]. It is derived from the two German terms 'Dunkelheit' and 'Windflaute', meaning darkness and little wind, respectively. It is also known as 'dark doldrums' and 'wind and solar drought' in other literature [24, 26, 27]. Dunkelflaute periods of simultaneous low power generation from wind and solar sources have been reported in many regions, including Europe [28, 29], Japan [26] and Australia [30]. For example, according to reference [31], there was a Dunkelflaute event between December 12 and 24, 2007, during which renewable generation was only about one-third of the average. In [32], the climatology of Dunkelflaute events in Germany between 1979 and 2018 was investigated under the assumption of a 100% renewable energy scenario. The study found an average of four Dunkelflaute events per year with a duration of up to nine days. A study from TU Dresden reported that in 2017, a

Dunkelflaute event persisted for 10 days between January 16 and 27, combined with high demand [33].

The consequences of Dunkelflaute events can be significant. They have the potential to cause energy deficits, leading to higher electricity prices and power outages, depending on the magnitude and conditions of the power system. When Dunkelflaute occurs during cold weather [29, 34], it can pose a significant threat to the power grid's security and balance, potentially causing energy supply breakdowns [35, 36] exacerbating the challenges associated with higher demand. Consequently, it is necessary to cover the load gap with flexible generation or imported electricity, which can significantly increase costs. Along with short-term sudden changes due to ramp events (a sharp change in power within a short time) [37, 38], Dunkelflaute events can lead to adverse economic effects. For example, in 2021, Northern Europe countries (including Denmark, Ireland, and the UK) experienced a significant decrease in wind energy production due to a wind drought. As a result, there was a sudden increase in demand for electricity generated from natural gas, which led to higher electricity prices. On March 22nd of 2022, Tokyo was exposed to the threat of a blackout because of a rise in power demand resulting from snowfall and lower temperatures. The supply deficiency from solar and the shutdown of a thermal power station further exacerbated the situation [39].

1.3 Climate Change

The urgency of mitigating climate change has led to ambitious plans to promote the use of renewable energy sources. However, this shift towards renewables could make the energy system more sensitive to climate variability. While renewable energies are essential for mitigating climate change, their dependency on weather and climate makes them vulnerable to changes in these factors [40]. Climate change can affect both long-term averages and short-term extremes of wind and solar weather conditions, which can directly affect the related renewable production [41, 42, 43, 44]. This vulnerability could affect not only the mean production of renewable energy but also its temporal stability. Previous research, which used climate projection methods, has predicted that 10%–20% power in Europe will change with the climate in the 21st century [45, 46, 43]. Therefore, it is crucial to address the challenges posed by climate change to renewable energy production in order to ensure a sustainable and reliable energy future.

Several studies have analyzed the effect of climate change on wind and solar power production in Europe. According to past research, the impact of climate change on the mean production of wind and solar power is negative but limited, and the reductions are projected to be between 0-10% in different scenarios [40, 43, 44, 47]. A declining trend in near-surface wind speeds and wind power generation is indicated in large regions throughout Europe (with the exception of the region close to the Black Sea) [48]. Offshore wind energy production is projected to slightly decrease in most regions in Northern Europe and significantly decrease in the Mediterranean (except for the sea areas close to the southwest Iberian Peninsula) [49]. According to the medium greenhouse gas emission scenario in [50], surface solar radiation in Europe is projected to increase in central and southern Europe but decrease in northern and eastern areas. It was observed that the most significant reductions in solar PV supply would be experienced in Northern European countries. However, the overall average change in PV production in Europe is expected to

be small, albeit that significant changes could occur at the country level.

The frequency of Dunkelflaute events is also likely to vary with climate change as research has indicated that related weather variables like precipitation and typhoon intensity will be affected [26]. A Dunkelflaute event which occurred in 2012 was used to simulate the 2030 future scenario, which found that the requirement for backup energy will increase by 71% [34]. Research to investigate the impact of climate changes on Dunkelflaute events is still limited, while assessing this effect is important for maintaining the supply-demand balance of grid systems. As renewable energy sources continue to play a crucial role in the transition to a low-carbon economy, ensuring the resilience of the power system to climate change-related challenges like Dunkelflaute events is a pressing research priority.

1.4 Research Questions

To handle the risks from Dunkelflaute events, we propose to **gain further scientific insights into historic and future Dunkelflaute events and explore reliable prediction approaches for these events**. A set of research sub-questions are studied:

Q1. What is the frequency, duration, driver, and spatial coherence of Dunkelflaute in Northern Europe?

Q2. Can we automatically identify Dunkelflaute events using publicly available meteorological data instead of limited power data?

Q3. Can we reliably model and predict Dunkeflaute events using a contemporary mesoscale model?

Q4. Can we reliably estimate Dunkeflaute events using contemporary machine-learning methods? How is their performance compared with mesoscale models?

Q5. What will Dunkelflaute be like in the future in the context of climate change?

1.5 Dissertation Outline

This dissertation addresses the proposed research questions and outlines various approaches to investigate the phenomenon of Dunkelflaute, including climatological analysis, physical modeling, and machine learning. The following chapters address the corresponding research sub-questions step by step.

In Chapter 3, a climatological study provides initial statistical insight into Dunkelflaute events in eleven countries surrounding the North and Baltic Sea regions. Meteorological and power production datasets for multiple years were utilized to quantify various statistics related to Dunkelflaute events and identified their underlying meteorological drivers. In addition, the weather patterns associated with these events, based on surface pressure and cloud cover, were also analyzed. By assuming an interconnected EU-11 power system, the effect of aggregating production over a wide area was also investigated.

In Chapter 4, an unsupervised deep learning framework named WISRnet was proposed to identify Dunkelflaute events through meteorological datasets. A CNN-based autoencoder was used to downscale the wind speed and insolation patterns, which are further fed to a k-means clustering model. This research successfully linked Dunkelflaute events with WISRnet-derived clusters and realized their identification without any power data.

In Chapter 5, a simulation of a Dunkelflaute event off the coast of Belgium was conducted using a mesoscale model, namely the Weather Research and Forecasting (WRF) model. To validate the accuracy of the model, a wide range of meteorological data sets (from such as floating lidars, radiosondes, and weather stations) and measured power production data were used. This research also provided additional insights regarding the WRF model's reliability in capturing Dunkelflaute events.

In Chapter 6, the capability of a machine learning model, LightGBM, was first demonstrated for estimating wind and solar power production during Dunkelflaute periods. Through multi-location and multi-variable modeling, this research provided not only precise estimation but also quantified the importance of various meteorological features in the prediction.

In Chapter 7, Dunkelflaute events were investigated through three future scenarios with different emission levels using the unsupervised deep learning framework, WISRnet, to cluster the events. Important insights into the relationship between Dunkelflaute and climate change were gained.

In Chapter 8, findings and suggestions for future research are summarised and discussed.

References

[1] United Nations. *Adoption of the Paris agreement, United Nations Framework Convention on Climate Change (UNFCCC)*. 2015.

[2] United Nations Framework Convention on Climate Change (UNFCCC). *Paris Agreement—Status of Ratification*. 2019.

[3] European Commission. *Communication from the Commission to the European Parliament, the Council, the European Economic and Social Committee and the Committee of the Regions-A policy framework for climate and energy in the period from 2020 to 2030*. 2014.

[4] European Commission. *The European green deal- Communication from the commission to the European parliament, the European Council, the Council, the European economic and social committee and the committee of the regions*. 2019.

[5] European Parliament et al. "Directive (EU) 2018/2001 of the European Parliament and of the Council of 11 December 2018 on the promotion of the use of energy from renewable sources". In: *Off. J. Eur Union Belgium* 20 (2018), p. 2.

[6] IRENA. "Renewable capacity statistics 2022". In: *International renewable energy agency* (2022).

[7] *Renewable Energy Statistics—Statistics Explained, Available online:* `https://ec.europa.eu/eurostat/statistics-explained/index.php/Renewable_energy_statistics#Share_of_renewable_energy_almost_doubled_between_2004_and_2018`.

[8] Idiano D'adamo. "Assessing environmental and energetic indexes in 27 European countries". In: *International Journal of Energy Economics and Policy* (2021).

[9] Svetlana Proskurina et al. "Five years left–How are the EU member states contributing to the 20% target for EU's renewable energy consumption; the role of woody biomass". In: *Biomass and bioenergy* 95 (2016), pp. 64–77.

[10] Dave Jones and Charles Moore. *Renewables Beat Fossil Fuels-a Half-Yearly Analysis of Europe's Electricity Transition. 2020.* 2020.

[11] IRENA. "Renewable capacity statistics 2020". In: *International renewable energy agency* (2020).

[12] Lizer Ramirez, Daniel Fraile, and G Brindley. "Offshorewind in Europe: Key trends and statistics 2020". In: (2021).

[13] R Martınez-Gordón et al. "A review of the role of spatial resolution in energy systems modelling: Lessons learned and applicability to the North Sea region". In: *Renewable and Sustainable Energy Reviews* 141 (2021), p. 110857.

[14] OSPAR Commission et al. *The quality status report 2010.* 2010.

[15] Laura Florentina Gusatu et al. "A spatial analysis of the potentials for offshore wind farm locations in the North Sea region: Challenges and opportunities". In: *ISPRS International Journal of Geo-Information* 9.2 (2020), p. 96.

[16] ENTSO-E. *Vision on Market Design and System Operation towards 2030.* 2020.

[17] Jan De Decker et al. "Offshore electricity grid infrastructure in Europe". In: *Offshore-Grid Final Report* (2011).

[18] North Seas Countries and the European Commission. "Political Declaration on energy Cooperation between the North Seas Countries". In: (2016).

[19] Rafael Martınez-Gordón et al. "Modelling a highly decarbonised North Sea energy system in 2050: A multinational approach". In: *Advances in Applied Energy* 5 (2022), p. 100080.

[20] Edward Baleke Ssekulima et al. "Wind speed and solar irradiance forecasting techniques for enhanced renewable energy integration with the grid: a review". In: *IET Renewable Power Generation* 10.7 (2016), pp. 885–989.

[21] Mukund K Deshmukh and Sandip S Deshmukh. "Modeling of hybrid renewable energy systems". In: *Renewable and sustainable energy reviews* 12.1 (2008), pp. 235–249.

[22] Matthias Huber, Desislava Dimkova, and Thomas Hamacher. "Integration of wind and solar power in Europe: Assessment of flexibility requirements". In: *Energy* 69 (2014), pp. 236–246.

[23] FJ Santos-Alamillos et al. "Combining wind farms with concentrating solar plants to provide stable renewable power". In: *Renewable Energy* 76 (2015), pp. 539–550.

[24] Yuhji Matsuo et al. "Investigating the economics of the power sector under high penetration of variable renewable energies". In: *Applied Energy* 267 (2020), p. 113956.

[25] Chris Gilbert. *It's dark, it's still – it's dunkelflaute, Available online:* `https://www.energynetworks.com.au/news/energy-insider/2021-energy-insider/its-dark-its-still-its-dunkelflaute/`. 2021.

[26] Masamichi Ohba, Yuki Kanno, and Daisuke Nohara. "Climatology of dark doldrums in Japan". In: *Renewable and Sustainable Energy Reviews* 155 (2022), p. 111927.

[27] GL Doorman and Laurens De Vries. "Electricity market design based on consumer demand for capacity". In: *Joint EURELECTRIC-Florence School of Regulation* (2017).

[28] Damien Raynaud et al. "Energy droughts from variable renewable energy sources in European climates". In: *Renewable Energy* 125 (2018), pp. 578–589.

[29] Fabian Mockert et al. "Meteorological conditions during Dunkelflauten in Germany: Characteristics, the role of weather regimes and impacts on demand". In: *arXiv preprint arXiv:2212.04870* (2022).

[30] Andy Boston, Geoffrey D Bongers, and Nathan Bongers. "Characterisation and mitigation of renewable droughts in the Australian National Electricity Market". In: *Environmental Research Communications* 4.3 (2022), p. 031001.

[31] Przemyslaw Komarnicki, Michael Kranhold, and Zbigniew A Styczynski. "Introduction: Climate Policy Goals of Sustainable Energy Supply". In: *Sector Coupling-Energy-Sustainable Economy of the Future: Fundamentals, Model and Planning Example of a General Energy System (GES)*. Springer, 2022, pp. 1–44.

[32] Fabian Mockert et al. *Dunkelflauten in Germany: Climatology and Relation to Weather Regimes*. Tech. rep. Copernicus Meetings, 2022.

[33] P Jessen-Thiesen et al. "Dauer und Häufigkeit von Dunkelflauten in Deutschland". In: *Energiewirtschaftliche Tagesfragen* 69.1/2 (2019), pp. 62–65.

[34] Philipp Hauser et al. "Does increasing natural gas demand in the power sector pose a threat of congestion to the German gas grid? A model-coupling approach". In: *Energies* 12.11 (2019), p. 2159.

[35] Karin van der Wiel et al. "Meteorological conditions leading to extreme low variable renewable energy production and extreme high energy shortfall". In: *Renewable and Sustainable Energy Reviews* 111 (2019), pp. 261–275.

[36] Hannah C Bloomfield, David J Brayshaw, and Andrew J Charlton-Perez. "Characterizing the winter meteorological drivers of the European electricity system using targeted circulation types". In: *Meteorological Applications* 27.1 (2020), e1858.

[37] Masamichi Ohba, Shinji Kadokura, and Daisuke Nohara. "Impacts of synoptic circulation patterns on wind power ramp events in East Japan". In: *Renewable Energy* 96 (2016), pp. 591–602.

[38] Tinghui Ouyang et al. "Prediction of wind power ramp events based on residual correction". In: *Renewable energy* 136 (2019), pp. 781–792.

[39] Masamichi Ohba, Yuki Kanno, and Shigeru Bando. "Effects of meteorological and climatological factors on extremely high residual load and possible future changes". In: *Renewable and Sustainable Energy Reviews* 175 (2023), p. 113188.

[40] Sonia Jerez et al. "The impact of climate change on photovoltaic power generation in Europe". In: *Nature communications* 6.1 (2015), p. 10014.

[41] Sara C Pryor and RJ Barthelmie. "Climate change impacts on wind energy: A review". In: *Renewable and sustainable energy reviews* 14.1 (2010), pp. 430–437.

[42] Julia A Crook et al. “Climate change impacts on future photovoltaic and concentrated solar power energy output”. In: *Energy & Environmental Science* 4.9 (2011), pp. 3101–3109.

[43] Isabelle Tobin et al. “Assessing climate change impacts on European wind energy from ENSEMBLES high-resolution climate projections”. In: *Climatic Change* 128 (2015), pp. 99–112.

[44] Isabelle Tobin et al. “Climate change impacts on the power generation potential of a European mid-century wind farms scenario”. In: *Environmental Research Letters* 11.3 (2016), p. 034013.

[45] Hanna Hueging et al. “Regional changes in wind energy potential over Europe using regional climate model ensemble projections”. In: *Journal of Applied Meteorology and Climatology* 52.4 (2013), pp. 903–917.

[46] Mark Reyers, Joaquim G Pinto, and Julia Moemken. “Statistical–dynamical downscaling for wind energy potentials: evaluation and applications to decadal hindcasts and climate change projections”. In: *International Journal of Climatology* 35.2 (2015), pp. 229–244.

[47] J Scott Hosking et al. “Changes in European wind energy generation potential within a 1.5 C warmer world”. In: *Environmental Research Letters* 13.5 (2018), p. 054032.

[48] Richard Davy et al. “Climate change impacts on wind energy potential in the European domain with a focus on the Black Sea”. In: *Renewable and sustainable energy reviews* 81 (2018), pp. 1652–1659.

[49] Idar Barstad, Asgeir Sorteberg, and Michel dos-Santos Mesquita. “Present and future offshore wind power potential in northern Europe based on downscaled global climate runs with adjusted SST and sea ice cover”. In: *Renewable Energy* 44 (2012), pp. 398–405.

[50] Kimmo Ruosteenoja and Petri Räisänen. “Seasonal changes in solar radiation and relative humidity in Europe in response to global warming”. In: *Journal of Climate* 26.8 (2013), pp. 2467–2481.

2

Background

2.1 Meteorological Studies

2

2.1.1 Meteorological characteristics of Dunkelflaute

The scientific field of energy meteorology has expanded rapidly in response to the knowledge required concerning the relationship between climate and energy production-demand balance. Experts have played a vital role in this interdisciplinary field by investigating the impact of meteorological variability on energy generation and consumption, examining the potential effects of future climate change, and studying the seasonal predictability of energy-associated features. To better understand the variability of renewable energy generation and its drivers, it is essential to examine broad-scale synoptic weather patterns (WPs) that influence the evolution of local factors. Previous research has suggested that fluctuations in renewable energy are influenced by weather variability at different spatial and temporal scales, which involves the development of large-scale WPs [1, 2, 3].

Many researchers have investigated weather patterns related to low renewable power production. According to studies such as [4] for Germany and [5] for Europe, low renewable production events may be attributed to the presence of high-pressure systems (as shown in Fig. 2.1). These systems, which are referred to as blocking conditions, are characterized by high surface pressure, reduced winds, and cold and foggy weather during winter. These cloudy conditions are different from the usual blue sky accompanied by high surface pressure. In this condition, wind and solar power generation in Central Europe may experience subpar output, as highlighted in [2, 3]. For the four-weather regime classification developed in [6, 7, 8], the negative phase of the North Atlantic Oscillation (NAO), strongly associates with the Greenland Blocking weather regime, is correlated with cold and weak wind conditions [9, 2, 10]. This regime is linked to a reduction in energy production and an increase in energy demand across Europe. In a study focused on winter days, [3] investigated low wind energy output in Europe and discovered that the lowest wind power capacity factor (CF) for Germany occurred along with the European blocking weather regime, with a negative wind speed anomaly contributing to this effect. [11] reported a connection between energy compound events (ECEs) and weather regimes in Germany, with a higher frequency of occurrences during the European and Greenland Blocking weather regimes. These blocked regimes pose a high risk to adjacent countries located near the North and Baltic Seas, as they could face up to 50% underproduction. Furthermore, the study found that the odds of ECEs increase under the presence of blocked regimes, leading to widespread impacts across multiple European countries.

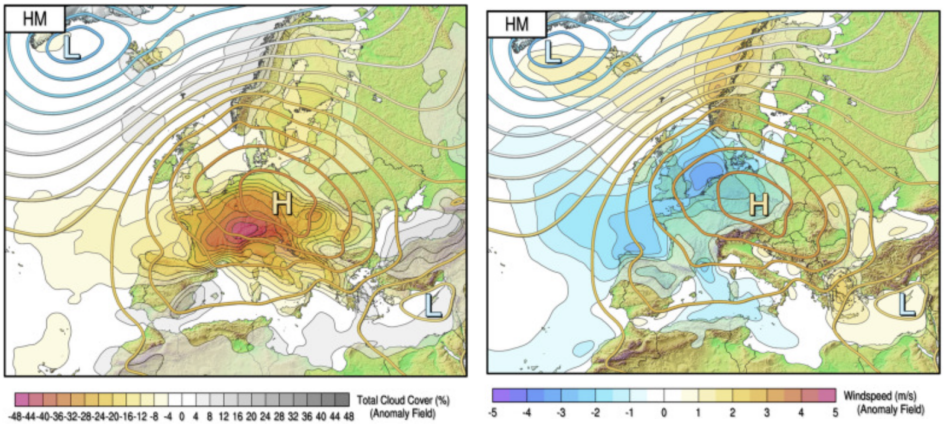

Figure 2.1: Cloud cover and wind speed anomalies associated with a high-pressure system during a period of low renewable energy production. [4]

Research focusing on Dunkelflaute events shows similar findings. According to [12, 4], Dunkelflaute can be classified by Grosswetterlagen, which is a system that categorizes circulation patterns in Europe using 29 different weather types that focus on regional conditions. It has been found that the most frequent pattern for Dunkelflaute in Germany is "Grosswetterlage GWL9," which is represented by a high-pressure system over Central Europe and has similar characteristics to the European Blocking weather regime. The wind speed and cloud cover anomaly composite plots in Fig. 2.1 can explain this weather pattern well. In [13] three blocking weather regimes were identified that were most frequently associated with Dunkelflaute, namely European Blocking (22%), Scandinavian Blocking (15%), and Greenland Blocking (14%). The most frequent pattern for Dunkelflaute was also found to be a high-pressure system over Germany and Central Europe, associated with the European Blocking weather regime. Dunkelflaute periods caused by Greenland Blocking are considered cold Dunkelflaute, with temperatures up to 4 °C colder than the 30-day running climatology, which leads to an increase in electricity demand for electrical heating. Such increased demand during periods of lower-than-normal power output by renewable energy sources puts a strain on the energy system. Additionally, it was found that Dunkelflaute can occur not only when high pressure prevails but also in conditions where Germany is situated between pronounced weather systems elsewhere. Notably, the most critical cold Dunkelflaute periods occur predominantly during the Greenland Blocking weather regime. In [14], research was carried out on the link between meteorological drivers and extreme residual load (RL) events in Japan. They used self-organizing maps (SOM) to classify WPs and found that these extreme RL events leading to energy shortage were strongly influenced by certain WPs. In particular, high RL mostly resulted from WPs with a strong pressure gradient, which causes cold air to come from the north. However, the increase in variable renewable energy resulted from cloudy and windless WPs are usually caused by southern coastal extratropical cyclones. [15] also explored the synoptic WPs correlated with "dark doldrums" in Japan, using SOM to classify WPs. They found that the frequent occurrence of dark doldrums was connected with four specific WPs, which

were produced by the interchange of rain fronts and cold air intrusion. These WPs have expanded cloud cover and calm wind.

In addition to WPs, other meteorological characteristics of Dunkelflaute have also been investigated, such as the seasonal dependency and the Dunkelflaute duration. [13] reported that Dunkelflaute occurs mainly in autumn and winter in Germany. During these seasons, there is low mean solar capacity factor due to low solar radiation, and thus Dunkelflaute events are mainly the result of periods of low-wind duration. These findings were consistent with the studies of [12, 4]. [4] further observed that all shortfall events happened in these seasons regardless of the event duration, with most of the events occurring in January (7 to 8 events out of 20 occur in this month), as shown in Fig. 2.2. According to [13], the duration of Dunkelflaute events associated with weather regimes is quite long, particularly for Greenland Blocking weather regimes, with an average of 19 days. [12] also studied Dunkelflaute in Germany from 1995 to 2015 and identified 23 wind events lasting at least 48 hours. The identification was based on capacity factors below certain threshold values. Longer events were less frequent, with around 6 events lasting more than 96 hours.

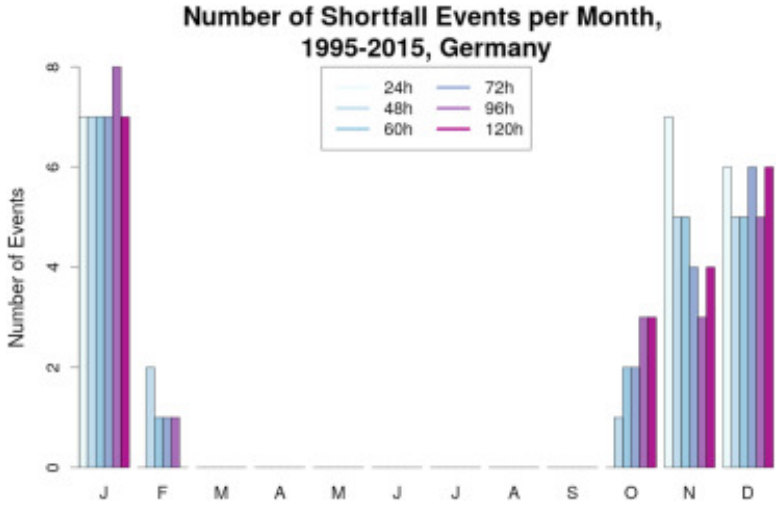

Figure 2.2: Number of shortfall events per month from 1995 to 2015 in Germany. [4]

2.1.2 Forecasting Dunkelflaute

Since Dunkelflaute events have a close relationship with weather regimes, it is possible to use weather regimes as a predictor, which can identify both the probability and duration of a potential Dunkelflaute event. Various methods have been suggested to forecast Dunkelflaute events, as well as energy supply and demand, including grid-point-based and pattern-based methods [16, 17]. The former utilizes grid-point surface meteorological forecasts to predict relevant power quantities, while the latter assigns the large-scale atmospheric flow to a pre-identified circulation pattern, and estimates surface impact in two steps. [17] have shown that grid-point forecasts have higher accuracy for short lead times

(days 0-10), while pattern-based methods show greater accuracy for extended lead times (day 12+).

With the results of [13], combined with those of [18] indicating that surface weather is influenced by weather regimes, and the promising skill of using weather regimes in sub-seasonal to seasonal forecasting, weather regime forecasts are essential for energy system operators to prepare for multi-day supply shortages. However, according to [19, 20], the blocking-type weather regimes have lower intrinsic predictability, particularly over Europe, which can result in lower forecast skill. The limitations might also arise from the difficulties that models face in accurately capturing the underlying physical processes, which vary with different spatial scales, such as latent heat release in meso–scale and synoptic-scale systems [21, 22]. These errors affect the prediction of transition into blocking-type regimes, which further contribute to lower forecast skill [23, 24]. To enhance the sub-seasonal predictability of blocking, it is necessary to investigate the blocking dynamics on sub-seasonal temporal scales in the future, as suggested by [18].

2.2 Power forecasting: from physical models to big data

Accurate power forecasting is a critical task in the renewable energy sector, especially for sources like solar and wind that are subject to variability due to weather patterns. To address this challenge, a variety of approaches have been developed, which have been broadly categorized into four branches: physical approaches, statistical approaches, artificial intelligence strategies, and hybrid approaches [25, 26, 27].

Numerical weather prediction (NWP) models are widely used in power forecasting, particularly for wind power. These models use physical and mathematical equations to simulate the atmosphere's behavior and predict meteorological variables, such as wind speed, temperature, and air pressure [28]. While NWP models are primarily proposed to predict weather conditions over extensive regions, their results can be aggregated to derive predictions of wind and solar power. Many researchers have reviewed the use of global and regional NWP models, as well as the commercial and operational systems for predicting wind power production [29, 30], and more effective hybrid models have been proposed [31]. While NWP models can provide accurate predictions, several issues have become troublesome for the applications. Firstly, the computational burden dramatically increases due to the high physical complexities [32]. Physical models usually require a large quantity of weather variables that must be available during calculation, which is unrealistic for many scenarios. Secondly, the prediction error accumulates with time since achieving an absolutely accurate solution to the partial differential equations in NWP models is impossible [33, 34]. Due to these drawbacks, it is necessary to develop new approaches with low cost and general availability.

Statistical models for power prediction are mathematical approaches based on regression assumptions and parameter optimization using big data. In wind power forecasting, statistical models are commonly used to forecast wind speed based on time-series data [30]. Various statistical methods such as an autoregressive model [35], exponential smoothing [36], and autoregressive integrated moving average [37, 38] have been developed to optimize the model parameters and enhance forecasting stability. However, these models

rely on assumptions regarding the data distributions and are not suitable for nonlinear time series forecasting [25]. To improve prediction accuracy, non-linear statistical models have been developed, including non-linear autoregression with exogenous input [39], multiple-kernel relevance vector regression [40], and Bayesian-based adaptive robust multi-kernel regression [41]. Although plenty of approaches have been proposed, the accuracy of traditional statistical models has been limited by their ability in extracting data features.

2.3 Machine Learning (ML)

2.3.1 ML in earth and atmospheric science

Machine learning (ML) has become a popular approach to identify extreme weather events. It refers to a branch of artificial intelligence that utilizes large datasets to identify intricate patterns and generate tailored predictions or decisions [42, 43]. Over the past decade, machine learning has seen unprecedented growth in many scientific domains, including the Earth system sciences. Due to the Earth system's nonlinear and chaotic behavior, learning complex nonlinear dynamics from data is a promising approach for accurate modeling. The European Centre for Medium-Range Weather Forecasts (ECMWF), for example, has accumulated hundreds of petabytes of Earth-system-related data in its archive [44]. Geosciences have undergone a major transformation with the advent of big data and numerous geoscience data banks have been produced, providing potential for geoscientists to apply machine learning for accurate modeling of the state and evolution of the Earth system [45]. Additionally, recent activities have resulted in newly-generated data resources with consistently high quality and high spatio-temporal resolutions, e.g., few-kilometer and hourly resolution (or better) for Europe [12].

These advancements have made long-term, gridded meteorological data readily available in the public domain, which has allowed for the application of many machine-learning methods that are a natural fit for the problems encountered in geoscience applications. There has been a wide range of machine learning applications across all components of Earth system models, as well as across the entire workflow of weather and climate prediction models [44]. The specific applications encompass the atmosphere and atmospheric chemistry [46, 47], ocean [48], land surface, sea ice, land ice [49], severe weather [50] and for all the processes of weather and climate prediction models [51, 52, 53].

One specific application of ML in geosciences is classification and pattern recognition. For instance, [54] employed a deep convolutional neural network (CNN) to classify tropical cyclones, atmospheric rivers, and weather fronts to detect these extreme events. Assisted by a Bayesian approach, the ML system achieved high classification accuracy, ranging from 89% to 99%. In regions lacking labeled data, a 3D convolutional auto-encoder was applied by [55] to enhance the identification of extreme climate events. [56] proposed a deep learning strategy using generative adversarial networks and convolutional neural networks, which presents high efficiency in weather pattern classification for PV power forecasting.

Time-series analysis is another typical application, which is used to analyze the internal relationships between geoscience variables and future weather conditions. By analyzing historical data on temperature, precipitation, and other meteorological variables, researchers can use time-series models to predict future trends and patterns. For example, [57] proposed

a temporal convolutional neural (TCN) network-based approach, which forecasts weather variables (including pressure, temperature, and humidity) using time-series data with low prediction errors. In addition, by analyzing the contribution of variables to the prediction, researchers can further obtain the relationship between input and prediction variables [58].

Machine learning algorithms have also been proven useful in addressing specific challenges within the geoscience domain. An example of this is the reconstruction of missing values in climate datasets, which is a task that can be accomplished using Convolutional Neural Network (CNN)-based algorithms. A study by [59] demonstrated the effectiveness of this approach in reconstructing missing values in global climate datasets like HadCRUT4. Another example is learning from unlabeled data which is inconvenient to handle by researchers. ML approaches like semi-supervised and unsupervised learning can help alleviate the dependence on labels. For instance, [60] investigated the application of semi-supervised learning with a self-training-based label propagation method, which demonstrated superior performance to supervised learning approaches.

2.3.2 ML in power forecasting

Machine learning (ML) has gained widespread popularity as a promising technique for power forecasting [61]. The primary advantage of ML over traditional statistical methods is its capability to process massive amounts of data, extract useful features, and generate accurate predictions. Power forecasting, which involves predicting energy demand and production, relies heavily on historical data of weather conditions and energy usage. ML models can be trained using these data to capture the complex relationships between energy production, weather patterns, and other relevant factors. Many review papers have conducted comprehensive comparisons and summaries of the ML methods for wind and solar forecasting [62, 63, 64, 65, 66, 67, 68].

Deep learning is a branch of ML, which has been adopted as a favored methodology in power forecasting, given its capacity to capture intricate patterns in data and deliver precise predictions. Deep neural networks, in particular, are based on mirroring the hierarchical configuration of the human brain. In comparison with traditional machine learning methods, deep learning obviates the requirement for complicated feature engineering, empowering the model to learn directly from unprocessed data. In power forecasting, existing NN-based approaches have demonstrated superiority. For example, [69] employed artificial neural networks (ANNs) to predict the wake effects on a wind farm, which yielded highly encouraging results. In addition, ANNs are one of the most accurate machine-learning algorithms for forecasting photovoltaic (PV) solar power output. Both single-algorithm and multiple-algorithm studies have shown that ANNs consistently produce high-accuracy forecasts for PV solar power output and are more effective than other tested ML algorithms [70, 71, 72]. Fig. 2.3 shows an example architecture of an ANN.

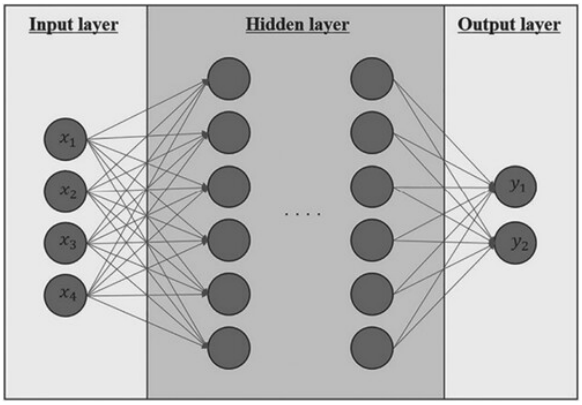

Figure 2.3: Structure of an ANN for solar power prediction. [70]

A Convolutional Neural Network (CNN) is a powerful deep learning approach that has been used in power forecasting. It can extract spatial and temporal features from input data, which can then be used to make predictions about future energy production or consumption. One approach utilizing CNNs is demonstrated by [73] (architecture shown in Fig. 2.4), decomposing input data into multiple frequencies with a wavelet transform and then predicting each frequency with a deep CNN. Another approach is to incorporate weather images as inputs, thereby capturing useful weather information and enhancing power forecasting [74]. CNNs have also evolved to improve power forecasting performance. For instance, an efficient deep CNN has been developed in [75] with an enhanced regression output layer. An improved residual-based deep CNN was proposed in [76], which outperformed multiple previous deep learning networks for power forecasting.

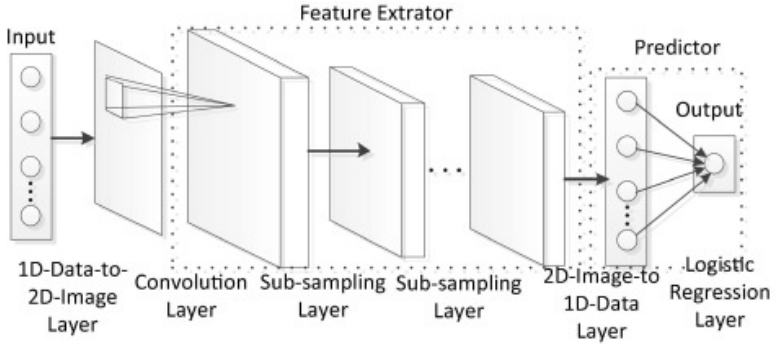

Figure 2.4: Structure of a CNN for wind power prediction. [73]

Long Short-Term Memory (LSTM) is another important deep learning algorithm used in power forecasting due to its ability to model long-term dependencies. The LSTM cells can transmit and preserve information through the temporal dimension, and are therefore useful in time-series forecasting. However, training an LSTM can be time-consuming and may result in low prediction accuracy. To improve the performance of LSTMs, researchers

have proposed various modifications. For instance, additional CNNs were utilized by [77] to extract variable features and the LSTM is applied for wind power forecasting. [78] introduced a new LSTM-based model, which improves the forget gate function and activation function. Additionally, a shared weight LSTM model was proposed to handle the time-consuming issue and reduce the tuning parameters [79].

In addition to deep learning approaches, various decision tree (DT)-based models have evolved to enhance the predictability of wind power production. These models, such as random forest (RF), extra trees, extreme gradient boosting (XGB), and gradient boosted regression trees (GBRTs), are based on ensemble learning and multivariate regression techniques. Among these models, GBRTs have received increased attention due to their promising forecasting ability, stability, and ease of implementation [80]. Recent studies have demonstrated the effectiveness of tree-based ensemble methods in predicting renewable energy [81, 82, 83]. For example, for PV solar power output, the DT algorithm outperforms other machine learning techniques like an ANN and a RF [84, 85]. Furthermore, [86] has shown better solar power forecasting performance using the XGB algorithm than other ML techniques including the RF algorithm. These studies suggest that decision-tree-based models have a promising future in renewable energy forecasting.

References

[1] Laura Zubiate et al. “Spatial variability in winter NAO–wind speed relationships in western Europe linked to concomitant states of the East Atlantic and Scandinavian patterns”. In: *Quarterly Journal of the Royal Meteorological Society* 143.702 (2017), pp. 552–562.

[2] Karin van der Wiel et al. “The influence of weather regimes on European renewable energy production and demand”. In: *Environmental Research Letters* 14.9 (2019), p. 094010.

[3] Christian M Grams et al. “Balancing Europe’s wind-power output through spatial deployment informed by weather regimes”. In: *Nature climate change* 7.8 (2017), pp. 557–562.

[4] Jaqueline Drücke et al. “Climatological analysis of solar and wind energy in Germany using the Grosswetterlagen classification”. In: *Renewable Energy* 164 (2021), pp. 1254–1266.

[5] Karin van der Wiel et al. “Meteorological conditions leading to extreme low variable renewable energy production and extreme high energy shortfall”. In: *Renewable and Sustainable Energy Reviews* 111 (2019), pp. 261–275.

[6] Robert Vautard. “Multiple weather regimes over the North Atlantic: Analysis of precursors and successors”. In: *Monthly weather review* 118.10 (1990), pp. 2056–2081.

[7] Paul-Antoine Michelangeli, Robert Vautard, and Bernard Legras. “Weather regimes: Recurrence and quasi stationarity”. In: *Journal of the atmospheric sciences* 52.8 (1995), pp. 1237–1256.

[8] Christophe Cassou. “Intraseasonal interaction between the Madden–Julian oscillation and the North Atlantic Oscillation”. In: *Nature* 455.7212 (2008), pp. 523–527.

[9] HC Bloomfield, CC Suitters, and DR Drew. "Meteorological drivers of European power system stress". In: *Journal of Renewable Energy* 2020 (2020), pp. 1–12.

[10] Paulina Tedesco et al. "Gaussian copula modeling of extreme cold and weak-wind events over Europe conditioned on winter weather regimes". In: *arXiv preprint arXiv:2209.12556* (2022).

[11] Noelia Otero et al. "Characterizing renewable energy compound events across Europe using a logistic regression-based approach". In: *Meteorological applications* 29.5 (2022), e2089.

[12] Frank Kaspar et al. "A climatological assessment of balancing effects and shortfall risks of photovoltaics and wind energy in Germany and Europe". In: *Advances in Science and Research* 16 (2019), pp. 119–128.

[13] Fabian Mockert et al. "Meteorological conditions during Dunkelflauten in Germany: Characteristics, the role of weather regimes and impacts on demand". In: *arXiv preprint arXiv:2212.04870* (2022).

[14] Masamichi Ohba, Yuki Kanno, and Shigeru Bando. "Effects of meteorological and climatological factors on extremely high residual load and possible future changes". In: *Renewable and Sustainable Energy Reviews* 175 (2023), p. 113188.

[15] Masamichi Ohba, Yuki Kanno, and Daisuke Nohara. "Climatology of dark doldrums in Japan". In: *Renewable and Sustainable Energy Reviews* 155 (2022), p. 111927.

[16] Albert Soret et al. "Sub-seasonal to seasonal climate predictions for wind energy forecasting". In: *Journal of Physics: Conference Series*. Vol. 1222. 1. IOP Publishing. 2019, p. 012009.

[17] Hannah C Bloomfield et al. "Pattern-based conditioning enhances sub-seasonal prediction skill of European national energy variables". In: *Meteorological Applications* 28.4 (2021), e2018.

[18] Dominik Büeler et al. "Year-round sub-seasonal forecast skill for Atlantic–European weather regimes". In: *Quarterly Journal of the Royal Meteorological Society* 147.741 (2021), pp. 4283–4309.

[19] Davide Faranda et al. "The switching between zonal and blocked mid-latitude atmospheric circulation: a dynamical system perspective". In: *Climate Dynamics* 47 (2016), pp. 1587–1599.

[20] Assaf Hochman et al. "Do Atlantic-European weather regimes physically exist?" In: *Geophysical Research Letters* 48.20 (2021), e2021GL095574.

[21] Mark J Rodwell et al. "Flow-dependent reliability: A path to more skillful ensemble forecasts". In: *Bulletin of the American Meteorological Society* 99.5 (2018), pp. 1015–1026.

[22] Christian M Grams and Heather M Archambault. "The key role of diabatic outflow in amplifying the midlatitude flow: A representative case study of weather systems surrounding western North Pacific extratropical transition". In: *Monthly Weather Review* 144.10 (2016), pp. 3847–3869.

[23] Laura Ferranti et al. “How far in advance can we predict changes in large-scale flow leading to severe cold conditions over Europe?” In: *Quarterly Journal of the Royal Meteorological Society* 144.715 (2018), pp. 1788–1802.

[24] Mio Matsueda and TN Palmer. “Estimates of flow-dependent predictability of wintertime Euro-Atlantic weather regimes in medium-range forecasts”. In: *Quarterly Journal of the Royal Meteorological Society* 144.713 (2018), pp. 1012–1027.

[25] Huaizhi Wang et al. “A review of deep learning for renewable energy forecasting”. In: *Energy Conversion and Management* 198 (2019), p. 111799.

[26] Amir Mosavi et al. “State of the art of machine learning models in energy systems, a systematic review”. In: *Energies* 12.7 (2019), p. 1301.

[27] Hui Liu, Xiwei Mi, and Yanfei Li. “Smart deep learning based wind speed prediction model using wavelet packet decomposition, convolutional neural network and convolutional long short term memory network”. In: *Energy Conversion and Management* 166 (2018), pp. 120–131.

[28] Hui Liu, Hong-qi Tian, and Yan-fei Li. “Comparison of two new ARIMA-ANN and ARIMA-Kalman hybrid methods for wind speed prediction”. In: *Applied Energy* 98 (2012), pp. 415–424.

[29] Claudio Monteiro et al. *Wind power forecasting: State-of-the-art 2009.* Tech. rep. Argonne National Lab.(ANL), Argonne, IL (United States), 2009.

[30] Ren Cai et al. “Wind speed forecasting based on extreme gradient boosting”. In: *IEEE Access* 8 (2020), pp. 175063–175069.

[31] Ashraf Ul Haque, M Hashem Nehrir, and Paras Mandal. “A hybrid intelligent model for deterministic and quantile regression approach for probabilistic wind power forecasting”. In: *IEEE Transactions on power systems* 29.4 (2014), pp. 1663–1672.

[32] M Lydia et al. “Linear and non-linear autoregressive models for short-term wind speed forecasting”. In: *Energy conversion and management* 112 (2016), pp. 115–124.

[33] Akın Tascikaraoglu and Mehmet Uzunoglu. “A review of combined approaches for prediction of short-term wind speed and power”. In: *Renewable and Sustainable Energy Reviews* 34 (2014), pp. 243–254.

[34] Saurabh S Soman et al. “A review of wind power and wind speed forecasting methods with different time horizons”. In: *North American power symposium 2010.* IEEE. 2010, pp. 1–8.

[35] Philippe Poggi et al. “Forecasting and simulating wind speed in Corsica by using an autoregressive model”. In: *Energy conversion and management* 44.20 (2003), pp. 3177–3196.

[36] Muhammad Uzair Yousuf, Ibrahim Al-Bahadly, and Ebubekir Avci. “Current perspective on the accuracy of deterministic wind speed and power forecasting”. In: *IEEE Access* 7 (2019), pp. 159547–159564.

[37] SN Singh, Abheejeet Mohapatra, et al. “Repeated wavelet transform based ARIMA model for very short-term wind speed forecasting”. In: *Renewable energy* 136 (2019), pp. 758–768.

[38] Kalid Yunus, Torbjörn Thiringer, and Peiyuan Chen. "ARIMA-based frequency-decomposed modeling of wind speed time series". In: *IEEE Transactions on Power Systems* 31.4 (2015), pp. 2546–2556.

[39] Erasmo Cadenas et al. "Wind speed prediction using a univariate ARIMA model and a multivariate NARX model". In: *Energies* 9.2 (2016), p. 109.

[40] Sheng-wei Fei. "A hybrid model of EMD and multiple-kernel RVR algorithm for wind speed prediction". In: *International Journal of Electrical Power & Energy Systems* 78 (2016), pp. 910–915.

[41] Yun Wang et al. "Deterministic and probabilistic wind power forecasting using a variational Bayesian-based adaptive robust multi-kernel regression model". In: *Applied Energy* 208 (2017), pp. 1097–1112.

[42] Yann LeCun, Yoshua Bengio, and Geoffrey Hinton. "Deep learning". In: *nature* 521.7553 (2015), pp. 436–444.

[43] Ian Goodfellow et al. *Deep learning*. Vol. 1. 2. MIT press Cambridge, 2016.

[44] Peter D Dueben et al. "Challenges and benchmark datasets for machine learning in the atmospheric sciences: Definition, status, and outlook". In: *Artificial Intelligence for the Earth Systems* 1.3 (2022), e210002.

[45] Pejman Tahmasebi et al. "Machine learning in geo-and environmental sciences: From small to large scale". In: *Advances in Water Resources* 142 (2020), p. 103619.

[46] Noah D Brenowitz and Christopher S Bretherton. "Prognostic validation of a neural network unified physics parameterization". In: *Geophysical Research Letters* 45.12 (2018), pp. 6289–6298.

[47] Peer Nowack et al. "Using machine learning to build temperature-based ozone parameterizations for climate sensitivity simulations". In: *Environmental Research Letters* 13.10 (2018), p. 104016.

[48] Maike Sonnewald et al. "Bridging observations, theory and numerical simulation of the ocean using machine learning". In: *Environmental Research Letters* 16.7 (2021), p. 073008.

[49] Tom R Andersson et al. "Seasonal Arctic sea ice forecasting with probabilistic deep learning". In: *Nature communications* 12.1 (2021), p. 5124.

[50] Amy McGovern et al. "Making the black box more transparent: Understanding the physical implications of machine learning". In: *Bulletin of the American Meteorological Society* 100.11 (2019), pp. 2175–2199.

[51] Filipe Aires et al. "Statistical approaches to assimilate ASCAT soil moisture information—I. Methodologies and first assessment". In: *Quarterly Journal of the Royal Meteorological Society* 147.736 (2021), pp. 1823–1852.

[52] Julien Brajard et al. "Combining data assimilation and machine learning to emulate a dynamical model from sparse and noisy observations: A case study with the Lorenz 96 model". In: *Journal of computational science* 44 (2020), p. 101171.

[53] Peter Grönquist et al. "Deep learning for post-processing ensemble weather forecasts". In: *Philosophical Transactions of the Royal Society A* 379.2194 (2021), p. 20200092.

[54] Yunjie Liu et al. "Application of deep convolutional neural networks for detecting extreme weather in climate datasets". In: *arXiv preprint arXiv:1605.01156* (2016).

[55] Evan Racah et al. "Extremeweather: A large-scale climate dataset for semi-supervised detection, localization, and understanding of extreme weather events". In: *Advances in neural information processing systems* 30 (2017).

[56] Fei Wang et al. "Generative adversarial networks and convolutional neural networks based weather classification model for day ahead short-term photovoltaic power forecasting". In: *Energy conversion and management* 181 (2019), pp. 443–462.

[57] Pradeep Hewage et al. "Temporal convolutional neural (TCN) network for an effective weather forecasting using time-series data from the local weather station". In: *Soft Computing* 24 (2020), pp. 16453–16482.

[58] Andreas S Weigend. *Time series prediction: forecasting the future and understanding the past*. Routledge, 2018.

[59] Christopher Kadow, David Matthew Hall, and Uwe Ulbrich. "Artificial intelligence reconstructs missing climate information". In: *Nature Geoscience* 13.6 (2020), pp. 408–413.

[60] Michael W Dunham, Alison Malcolm, and J Kim Welford. "Improved well-log classification using semisupervised label propagation and self-training, with comparisons to popular supervised algorithms". In: *Geophysics* 85.1 (2020), O1–O15.

[61] Fouzi Harrou and Ying Sun. *Advanced statistical modeling, forecasting, and fault detection in renewable energy systems*. IntechOpen, 2020.

[62] Cyril Voyant et al. "Machine learning methods for solar radiation forecasting: A review". In: *Renewable energy* 105 (2017), pp. 569–582.

[63] Muhammad Naveed Akhter et al. "Review on forecasting of photovoltaic power generation based on machine learning and metaheuristic techniques". In: *IET Renewable Power Generation* 13.7 (2019), pp. 1009–1023.

[64] Huaizhi Wang et al. "Taxonomy research of artificial intelligence for deterministic solar power forecasting". In: *Energy Conversion and Management* 214 (2020), p. 112909.

[65] Adel Mellit et al. "Advanced methods for photovoltaic output power forecasting: A review". In: *Applied Sciences* 10.2 (2020), p. 487.

[66] Hui Liu et al. "Deterministic wind energy forecasting: A review of intelligent predictors and auxiliary methods". In: *Energy Conversion and Management* 195 (2019), pp. 328–345.

[67] Alberto Pliego Marugán et al. "A survey of artificial neural network in wind energy systems". In: *Applied energy* 228 (2018), pp. 1822–1836.

[68] Bo Yang et al. "State-of-the-art one-stop handbook on wind forecasting technologies: An overview of classifications, methodologies, and analysis". In: *Journal of Cleaner Production* 283 (2021), p. 124628.

[69] Michael F Howland and John O Dabiri. "Wind farm modeling with interpretable physics-informed machine learning". In: *Energies* 12.14 (2019), p. 2716.

[70] Yusuf Essam et al. “Investigating photovoltaic solar power output forecasting using machine learning algorithms”. In: *Engineering Applications of Computational Fluid Mechanics* 16.1 (2022), pp. 2002–2034.

[71] Mohammad H Alomari, Jehad Adeeb, and Ola Younis. “Solar photovoltaic power forecasting in jordan using artificial neural networks”. In: *International Journal of Electrical and Computer Engineering (IJECE)* 8.1 (2018), pp. 497–497.

[72] Ali Erduman. “A smart short-term solar power output prediction by artificial neural network”. In: *Electrical Engineering* 102.3 (2020), pp. 1441–1449.

[73] Huai-zhi Wang et al. “Deep learning based ensemble approach for probabilistic wind power forecasting”. In: *Applied energy* 188 (2017), pp. 56–70.

[74] Yuchi Sun, Gergely Szűcs, and Adam R Brandt. “Solar PV output prediction from video streams using convolutional neural networks”. In: *Energy & Environmental Science* 11.7 (2018), pp. 1811–1818.

[75] Sana Mujeeb et al. “Wind power forecasting based on efficient deep convolution neural networks”. In: *Advances on P2P, Parallel, Grid, Cloud and Internet Computing: Proceedings of the 14th International Conference on P2P, Parallel, Grid, Cloud and Internet Computing (3PGCIC-2019) 14*. Springer. 2020, pp. 47–56.

[76] Ceyhun Yildiz et al. “An improved residual-based convolutional neural network for very short-term wind power forecasting”. In: *Energy Conversion and Management* 228 (2021), p. 113731.

[77] Wenzu Wu et al. “Probabilistic short-term wind power forecasting based on deep neural networks”. In: *2016 international conference on probabilistic methods applied to power systems (PMAPS)*. IEEE. 2016, pp. 1–8.

[78] Ruiguo Yu et al. “LSTM-EFG for wind power forecasting based on sequential correlation features”. In: *Future Generation Computer Systems* 93 (2019), pp. 33–42.

[79] Zhendong Zhang et al. “Wind speed prediction method using shared weight long short-term memory network and Gaussian process regression”. In: *Applied energy* 247 (2019), pp. 270–284.

[80] Paulino J Garcıa Nieto et al. “Pressure drop modelling in sand filters in micro-irrigation using gradient boosted regression trees”. In: *Biosystems engineering* 171 (2018), pp. 41–51.

[81] Mark Landry et al. “Probabilistic gradient boosting machines for GEFCom2014 wind forecasting”. In: *International Journal of Forecasting* 32.3 (2016), pp. 1061–1066.

[82] Caroline Persson et al. “Multi-site solar power forecasting using gradient boosted regression trees”. In: *Solar Energy* 150 (2017), pp. 423–436.

[83] Alberto Torres-Barrán, Álvaro Alonso, and José R Dorronsoro. “Regression tree ensembles for wind energy and solar radiation prediction”. In: *Neurocomputing* 326 (2019), pp. 151–160.

[84] Aakash Gupta, Ankur Bansal, Kshitij Roy, et al. “Solar energy prediction using decision tree regressor”. In: *2021 5th International Conference on Intelligent Computing and Control Systems (ICICCS)*. IEEE. 2021, pp. 489–495.

[85] Dhriti G Shetty et al. “Prediction of solar energy using ML”. In: *International Journal of Scientific Research & Engineering Trends* 7.3 (2021), pp. 2069–2074.

[86] Berny Carrera and Kwanho Kim. “Comparison analysis of machine learning techniques for photovoltaic prediction using weather sensor data”. In: *Sensors* 20.11 (2020), p. 3129.

3

A Brief Climatology of Dunkelflaute Events Surrounding the North and Baltic Sea Areas

In the coming decades, the European energy system is expected to become increasingly reliant on non-dispatchable generation such as wind and solar power. Under such a renewable energy scenario, a better characterization of the extreme weather condition 'Dunkelflaute', which can lead to a sustained reduction of wind and solar power, is important. In this paper, we report findings from the very first climatological study of Dunkelflaute events occurring in eleven countries surrounding the North and Baltic Sea areas. By utilizing multi-year meteorological and power production datasets, we have quantified various statistics pertaining to these events and also identified their underlying meteorological drivers. It was found that almost all periods tagged as Dunkelflaute events (with a length of more than 24 h) are in November, December, and January for these countries. On average, there are 50–100 h of such events happening in each of these three months per year. The limited wind and solar power production during Dunkelflaute events is shown to be mainly driven by large-scale high-pressure systems and extensive low-cloud coverage. Even though the possibility of simultaneous Dunkelflaute events in neighboring countries can be as high as 30–40%, such events hardly occur simultaneously in all the eleven countries. Through an interconnected EU-11 power system, the mean frequency of Dunkelflaute drops from 3–9% for the individual countries to approximately 3.5% for the combined region, highlighting the importance of aggregating production over a wide area to better manage the integration of renewable energy generation.

This chapter is partly based on *Li, B., Basu, S., Watson, S. J., and Russchenberg, H. W. (2021). A brief climatology of dunkelflaute events over and surrounding the North and Baltic Sea areas. Energies, 14(20), 6508.* [1].

3.1 Introduction

In the near future, wind and solar power production are projected to contribute an increasingly higher proportion to Europe's energy mix. By 2030, renewable energy is expected to contribute up to one-third of the European total energy demand [2, 3], and this fraction will double by 2050 [4]. The North and Baltic Sea areas and bordering countries will account for a considerable share of this renewable generation capacity [5, 6, 7]. For an energy system that will become increasingly reliant on highly variable generation dominated by wind and solar sources, power production will become increasingly dependent on meteorological variability [8, 9, 10, 11]. Certain weather patterns can lead to adverse power production, e.g., a sustained period (multi-day) of extremely low power production [12, 9, 13], particularly during high demand periods [14, 15, 16]. It is important to characterize as well as to quantify the predictability of weather patterns leading to such extreme deficits for power grids to effectively balance supply and demand.

In this paper, we discuss one such unfavorable weather phenomenon which can lead to low levels of wind and solar power production, dubbed 'Dunkelflaute' [17, 18], primarily characterized by calm winds and overcast conditions. Over the past few years, several Dunkelflaute events have been reported in the Netherlands [19, 20], Belgium [21, 22], and Germany [23, 24], which required major intervention from the system operators, including demand-side management, reserve power deployment, and electricity imports from other countries to prevent power shortages. Previous studies of Belgian and Dutch Dunkelflaute events were documented in [17, 18], which was the first time the capabilities of mesoscale modeling were evaluated to simulate and forecast Dunkelflaute events.

With an increasing share of renewable generation in power systems, there is a pressing need for a detailed characterization of Dunkelflaute events across a wider range of countries. Unfortunately, the handful of case studies discussed in the previous papers do not provide any climatological information on this phenomenon. To fill this void, in this study, we consider eleven countries surrounding the North and Baltic Sea areas. We analyze thirty-two years of power production and meteorological data to quantify various basic statistics (e.g., frequency distributions) related to the Dunkelflaute events which have durations longer than one day. We believe that these statistics might be of use in the design of next-generation power grid systems, and in turn, reduce the adverse impacts of future Dunkelflaute events on electricity generation and transmission.

Recently, research has been carried out on the deployment of wind and solar energy in the power grid in terms of temporal variability [25, 26] and the correlation between output [27] and flexibility requirements [28, 29] for several countries. Widén [27] found a negative correlation between wind and solar power generation, which suggested that the combined deployment of wind and solar energy in the power system can help to balance temporal variability [10, 30, 31]. However, the mix fails to tackle extreme variations lasting for several days or even longer and calls for additional flexible resources [12, 32, 33]. To study persistent low renewable power production and high shortfall scenarios, van der Wiel et al. [13] focused on the 1-in-10-year extreme production events and emphasized their importance in future system design. However, to the best of our knowledge, none of these studies focused on the detailed characterization of Dunkelflaute periods, which is the sole purpose of the present study. Here, we quantify the temporal persistence of the Dunkelflaute events, and also document their seasonal variations and other traits. With

the increasing shares of variable renewable energy generation, such statistical information is critically important for flexibility in power systems.

Previous research has shown that meteorological conditions and their variability have a strong impact on energy-related parameters and thus influence wind and solar power supply [10, 11, 9, 8]. Large-scale weather patterns have a significant impact on surface conditions [34, 35, 36], e.g., blocked regimes and related high-pressure systems are known to be associated with low wind power production [13, 37, 38, 39, 40]. Aside from their impact on wind speed, synoptic-scale circulations can also significantly affect cloud cover and hence surface solar radiation [41, 42, 43, 44, 45] and solar power production [46, 13].

Li et al. [17] mentioned that in the meteorology literature, Dunkelflaute is typically known as anticyclonic gloom [47, 48]. It is associated with extremely weak wind, persistent high-pressure systems, and overcast conditions with stratus or stratocumulus clouds. In the present study, we further advance our understanding of Dunkelflaute events by creating climatological (anomaly) maps of several meteorological variables (e.g., cloud base height). From these maps, it also becomes evident that the Dunkelflaute events do not occur at the same time in all the countries surrounding the North and Baltic Sea areas. Results from spatial correlation analysis further lend support to this fact. Given these findings, we surmise that it may be possible to significantly reduce the adverse effects of Dunkelflaute via grid interconnection between all these countries. In this context, we provide rudimentary results, as in-depth analysis on grid interconnection is beyond the scope of the present study.

This chapter is organized as follows. In Section 3.2, we describe the power production and meteorological data utilized. We then quantify basic statistics and identify meteorological drivers of Dunkelflaute events in Sections 3.3 and 3.4, respectively. In Section 3.5, an assessment is made of the benefit of an interconnected grid, by simulating the interconnection of smaller regions into a larger power system. Finally, conclusions and prospective future work are discussed in Section 3.6.

3.2 Data and Methods

3.2.1 Simulated Power Production Data

Staffell and Pfenninger developed an open-source tool, called Renewables.ninja [49, 50], to investigate the electricity supply in Britain [26]. In this research, we utilize this model to explore Dunkelflaute characteristics for eleven countries bordering the North and Baltic Sea areas (see Figure 4.8), since these offshore areas and bordering countries account for a very considerable share of current and future European renewable generation capacity [39]. Besides, certain multi-national power grid schemes have been proposed for this region [6, 51], which are relevant for our analysis of interconnection effects (discussed later). Please note that we have excluded Latvia and Estonia from our analysis because they have very limited renewable energy capacity. To be specific, in 2016, Latvia and Estonia had installed solar energy generation capacities of 0.69 and 11.04 MW, respectively [52]. Hence, the eleven countries studied here are Belgium (BE), Germany (DE), Denmark (DK), Finland (FI), France (FR), Ireland (IE), Lithuania (LT), The Netherlands (NL), Norway (NO), Poland (PL), Sweden (SE), and the United Kingdom (UK).

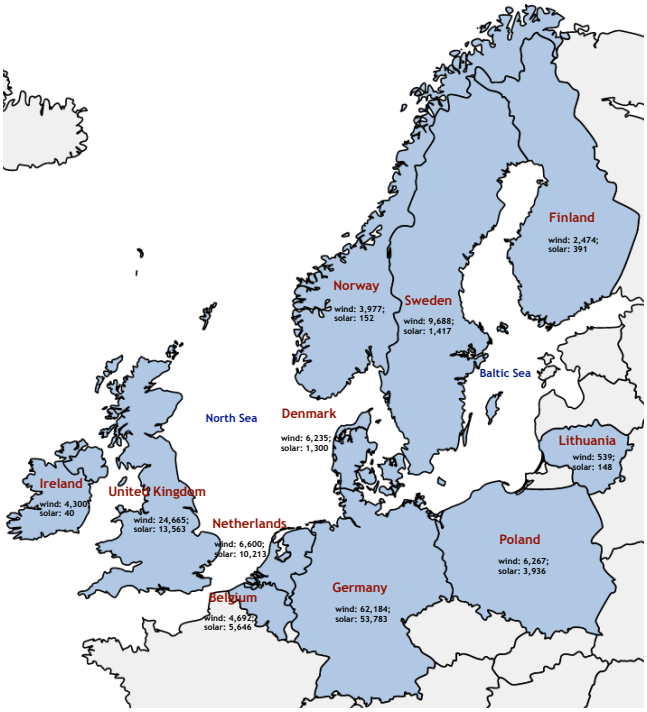

Figure 3.1: The eleven countries studied in the research bordering the North and Baltic Sea areas. For each country, the wind and solar capacities (MW) for the year of 2020 are listed, respectively [53].

The Renewables.ninja tool [50, 49] is used to provide hourly wind and solar capacity factors (CF) aggregated nationally for 32 years (1985–2016). The hourly wind and solar capacity factors are based on the meteorological data from the MERRA-2 reanalysis dataset. Reanalysis data have been widely used to simulate wind and solar power production because of their extensive coverage and availability. The Renewables.ninja tool uses the Virtual Wind Farm model to convert wind speed data at different heights to wind power output [49], while irradiance and temperature data are used to model solar power production utilizing the Global Solar Energy Estimator model, as illustrated in [50]. Compared with other models covering multiple countries [12, 54, 55], the Renewables.ninja tool has been calibrated using actual power production data, and has been proven to be quite accurate for Europe [26, 39].

The Renewables.ninja tool provides wind and solar capacity factors using weather data for the period 1985–2016 by simulating all operating wind and solar farms in 'current' locations as of 2016. The installed capacity of wind farms for 2016 for the eleven countries used in this study can be obtained from the Renewables.ninja dataset. The installed solar capacity for each country was obtained from IRENA statistics [52]. Capacity factors were converted to national generation potential by making use of the respective installed capacities in each country.

3.2.2 Validation of Simulated Power Production Data

In this section, we use measured power production data from the transmission system operators (TSOs) [56] to validate the capacity factors generated from the Renewables.ninja tool. Since the installed capacities used by the Renewables.ninja tool are constant based on the values as of December 2016, we used Belgian measured power production and installed capacity data for 2016 to validate the modeled data. It should be noted that the installed capacities of wind and solar power in Belgium were unchanged during 2016. Aggregated historical power production and installed capacity data are provided by the various TSOs (e.g., Elia for Belgium, TenneT, 50 Hertz, Amprion, and TransnetBW for Germany, and Energinet for Denmark). The Belgian power data have a sampling rate of 15 min, but we aggregated these to an hourly level to be consistent with the modeled capacity factor data. The wind and solar power production values have been normalized to their respective nominal capacities to obtain capacity factors. Scatter plots are shown in Figure 3.2 to compare the modeled wind and solar capacity factors with measured data from the TSO. Overall, the modeled capacities were reproduced quite well with Renewables.ninja data, though there was a small deviation at the higher end of the wind power capacity factor plot. Nonetheless, most of the values show a good correlation.

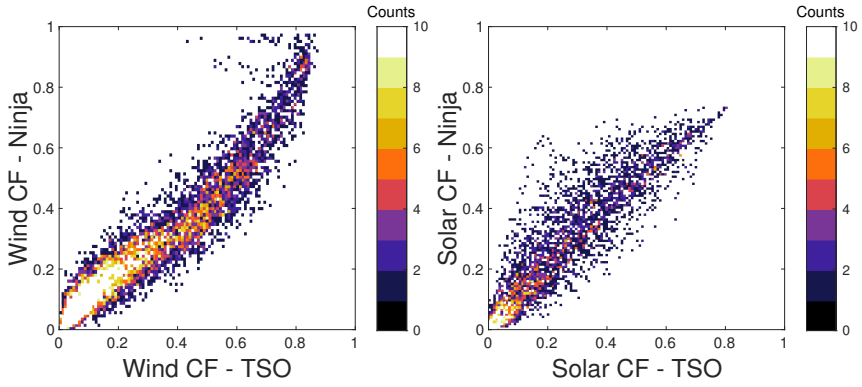

Figure 3.2: Bi-variate histograms of modeled and actual wind (**left** panel) and solar (**right** panel) power capacity factors (CF) for 2016 in Belgium.

3.2.3 Reanalysis Data

To analyze the variability of meteorological conditions during Dunkelflaute events, the popular ERA5 reanalysis dataset was used (from ECMWF, the European Centre for Medium-Range Weather Forecasts [57]). ERA5 employs a horizontal grid size of 31 km and consists of hourly data. For this work, the same temporal coverage as provided by the Renewables.ninja tool (32 years, 1985–2016) was used. In our previous work, the ERA5 dataset has been shown to rather accurately characterize Dunkelflaute events [17], including reproducing vertical profiles and time series of various meteorological variables. In the present study, we utilized air pressure at mean sea level, cloud base height, and low cloud cover from the ERA5 dataset.

3.3 Characteristics of Wind and Solar Power Generation during Dunkelflaute

Taking Germany, Norway, and the UK as examples, Figure 3.3 shows the annual frequency of Dunkelflaute events defined using percentage capacity factor and time duration thresholds. In this figure, the capacity factor (CF) is defined as the fraction of wind and solar photovoltaic (PV) power production normalized by the respective installed capacity of wind and PV generation, where the fractions are the same for each. For example, a CF threshold value of 10% implies a capacity factor threshold of 10% for wind and 10% for PV. The number of Dunkelflaute events per year is noticeably decreased by reducing the capacity factor threshold or increasing the length of duration, since both conditions provide a more rigorous test for what constitutes a Dunkelflaute event.

For example, there are approximately 5–10 cases that are longer than one day each year in Germany for a threshold of 20% of capacity, with the most persistent events lasting for 4–5 days. These types of long-lasting Dunkelflaute events can challenge the grid operator when balancing supply and demand and may require the procurement of power from neighboring countries at a relatively high market price. In contrast, for a capacity threshold of 10%, there are hardly any cases lasting longer than two days, since one long-lasting event can be split into several shorter cases once there are a few samples having capacity factors larger than 10%.

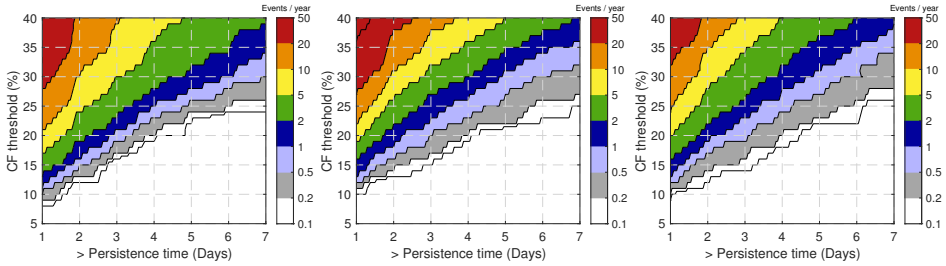

Figure 3.3: The frequency of Dunkelflaute events for Germany (**left** panel), Norway (**middle** panel), and the UK (**right** panel) respectively, using different thresholds for capacity factor and time duration. The underlying data, spanning the years of 1985 to 2016, were generated by the Renewables.ninja tool.

When only considering prolonged periods of low wind power generation in Great Britain [9] (i.e., not accounting for PV generation), there are about 5–6 low wind production cases annually using a 5% CF threshold and persistence of longer than one day. Since the definition of a Dunkelflaute event includes both low wind and solar power production, the results in Figure 3.3 show a lower frequency of occurrence than that seen in [9]. It can also be seen that the number of events tagged as Dunkelflaute events does not vary much for the three different countries.

For the remainder of this paper, we have chosen to classify an event as a Dunkelflaute event if wind and solar CFs both fall below a specific threshold of 20% during a particular 60 min period, which means both wind and PV power production being lower than 20% of their respective capacities. It should be noted that although it can be expected that there is no or little solar power production after sunset and before sunrise, calm nighttime

conditions are of significance from the point of view of system balancing, and therefore are included in this climatological analysis.

Figure 3.4 shows the frequency distribution of the length of events classified as Dunkelflaute for Belgium, Germany, and Denmark comparing modeled data from Renewables.ninja and the actual power production data from the TSOs. The frequency peaks at a duration between 12 and 24 h with a similar distribution for the three countries. There is good agreement between the two data sources, although there is an overestimation of the peak frequency for Germany using the Renewables.ninja data.

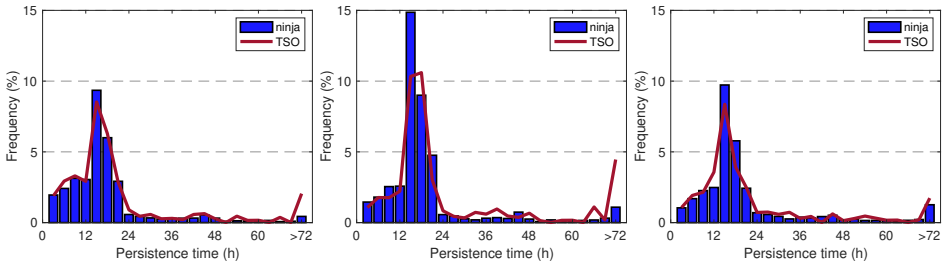

Figure 3.4: Frequency distribution of modeled (ninja) and actual (TSO) Dunkelflaute durations for Belgium (**left** panel), Germany (**middle** panel), and Denmark (**right** panel). The modeled data, spanning the years of 1985 to 2016, were generated by the Renewables.ninja tool. Actual power production data from the TSOs are for the years 2015-18.

Figure 3.5 shows the average monthly hours of Dunkelflaute events for the eleven countries based on the Renewables.ninja data. We included only those events lasting for more than one day and plotted the total number of hours per month. As seen in the left panel of Figure 3.5, there is clearly a common distribution of the annual cycle of Dunkelflaute events for the different countries. Notably, almost all of the Dunkelflaute events lasting more than one day are predominantly present during the extended winter period (October–February). In fact, the occurrence of Dunkelflaute events mainly peaks in November, December, and January, during each of which there are 50–100 h of such events per year. One exception is in Sweden, with a larger magnitude of more than 150 h for the three months. The overall distribution is similar when using the measured (TSO) data in Belgium, Germany, and Denmark for 2015–2018 (refer to the right panel of Figure 3.5), though we can see a relatively larger magnitude of Dunkelflaute hours in January for the 4-year actual production data.

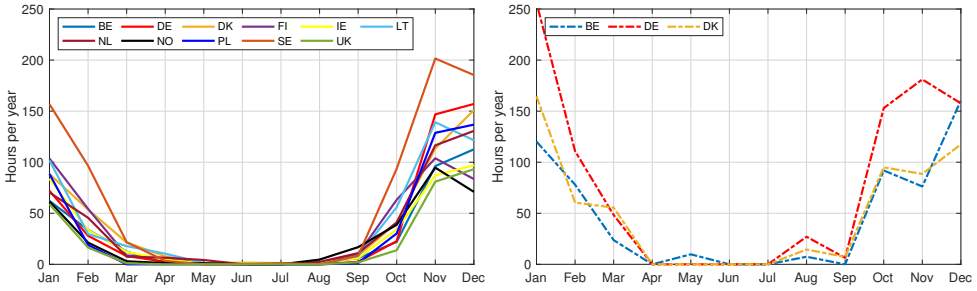

Figure 3.5: The **left** panel shows the monthly variation of Dunkelflaute hours per year for eleven countries over the North Sea and Baltic Sea based on the Renewable.ninja data. The **right** panel is similar but using actual production data from the TSOs to identify Dunkelflaute in Belgium (BE), Germany (DE), and Denmark (DK) for 2015–2018. We only account for the Dunkelflaute events longer than one day.

3.4 Meteorological Drivers

Dunkelflaute is shown to be associated with near-calm and stratus and/or stratocumulus-covered conditions driven by a high-pressure system [17]. We used hourly values of mean sea level pressure and cloud cover data from ERA5 for the Dunkelflaute periods during 1985–2016 to investigate how periods of Dunkelflaute are correlated with these variables. Spatial anomaly maps were created and averaged for those periods when Dunkelflaute events were prevalent. These Dunkelflaute periods were identified using the Renewable.ninja tool, as described before. Taking four representative countries of Denmark, Poland, Sweden, and the UK as examples, we analyzed the pressure and cloud cover maps to determine the weather factors giving rise to Dunkelflaute events for these countries.

3.4.1 Pressure

During Dunkelflaute periods (see top row of Figure 3.6), an extensive high-pressure system is clearly prevalent. The specific location, size, and magnitude of the system vary for individual events and countries. For example, during periods of Dunkelflaute in Denmark (top row, first column), Poland, and Sweden (top row, second and third columns, respectively), pressure in the Scandinavian area and Central Europe is higher than in the surrounding areas respectively, while for the UK (top row, fourth column), a high-pressure center is located over most of the North Sea area. Overall, the extended high surface pressure area developed over the four countries shows a slack pressure gradient, leading to a much lower surface wind speed in the individual countries. This is likely to lead to much lower levels of wind power production over an extended area.

These results are in agreement with previous studies, that show that large-scale high-pressure systems influence local weather and can further negatively affect both available wind and solar power generation [46, 40, 13]. These studies showed that such high-pressure systems are not associated with clear skies, but instead thick and extensive cloud cover, which are very characteristic of Dunkelflaute events (i.e., anticyclonic gloom weather [58, 59]). This will be discussed further in the next section. Amongst the various synoptic-scale weather phenomena which have been shown to strongly affect wind power generation in western Europe [60, 61, 62, 37], blocking of high-pressure systems (and the absence of

westerly airflow into Europe) can result in extended periods of low production and periods of Dunkelflaute [40, 37, 38, 39].

3.4.2 Cloud

Overcast sky with extensive low cloud cover is very characteristic of anticyclonic gloom weather. As seen in the maps of the mean cloud base height (CBH), when a Dunkelflaute event occurs, the height drops below 600 or even 400 m in the North and Baltic Sea areas and adjacent countries (second row of Figure 3.6). The third row of Figure 3.6 shows maps of the CBH anomaly calculated by subtracting the overall monthly mean CBH values from the mean values observed during periods of Dunkelflaute. Extensive areas of negative CBH anomaly (i.e., reduced CBH) are clearly seen over the four countries during periods of Dunkelflaute, with values of between approximately −500 and −100 m (third row of Figure 3.6).

Low-level cloud is an important element that strongly influences radiative features and local weather [63, 64, 65]. Over the North Sea, the low-level cloud is predominantly comprised of stratus, stratocumulus, and fog [66], consistent with the cloud cover types observed during anticyclonic gloom [17]. Several studies [67, 68, 69, 70] have shown that synoptic conditions in the North Sea area frequently give rise to extensive stratocumulus clouds. For example, stratocumulus over the North Sea with a cloud top at 800 m and base at 400 m was observed by Nicholls [69], driven by a near stationary anticyclone located west of Ireland. Moderate winds with little shear were observed, which is also the case for nocturnal stratocumulus over the UK [67, 68, 70]. CBH for another five cases observed in the stratocumulus-topped boundary layer in the North Sea by Nicholls and Leighton [70] were all lower than or almost equal to 1000 m.

The high albedo of these low stratocumulus clouds can considerably reduce the incoming radiative flux at the surface. As described in [71, 64, 72, 73], there is approximately a 40–50% reduction of surface solar radiation during the presence of stratus or stratocumulus clouds in comparison with cloud-free regions. The combination of lower than normal solar radiation over the regions of interest and shorter day lengths in winter (during which most Dunkelflaute events occur) indicates that total daily energy production from solar farms will be limited during periods of extensive stratocumulus. Furthermore, it should be noted that the occurrence of stratocumulus clouds mentioned above is associated with high-pressure systems, especially over the sea [71, 64, 70]. This is consistent with the observations in the previous section based on the top row of Figure 3.6.

Extensive coverage of low clouds (lower than approximately 2 km) also plays an important role in surface weather on the synoptic scale. The fourth row of Figure 3.6 suggests that low cloud cover (LCC) averaged for Dunkelflaute periods is around 0.7–0.9, which is significantly higher than the monthly mean LCC. This can be seen in the anomaly maps in the fifth row of Figure 3.6, where the mean overall LCC is subtracted from the mean LCC during Dunkelflaute events. Warren et al. [66] also found that LCC is about 0.7 when stratocumulus clouds occur over the North Sea. Positive anomaly values of LCC of around 0.1 to 0.3 are clear in the bottom row of Figure 3.6 for Dunkelflaute events occurring in Denmark, Poland, Sweden, and the UK.

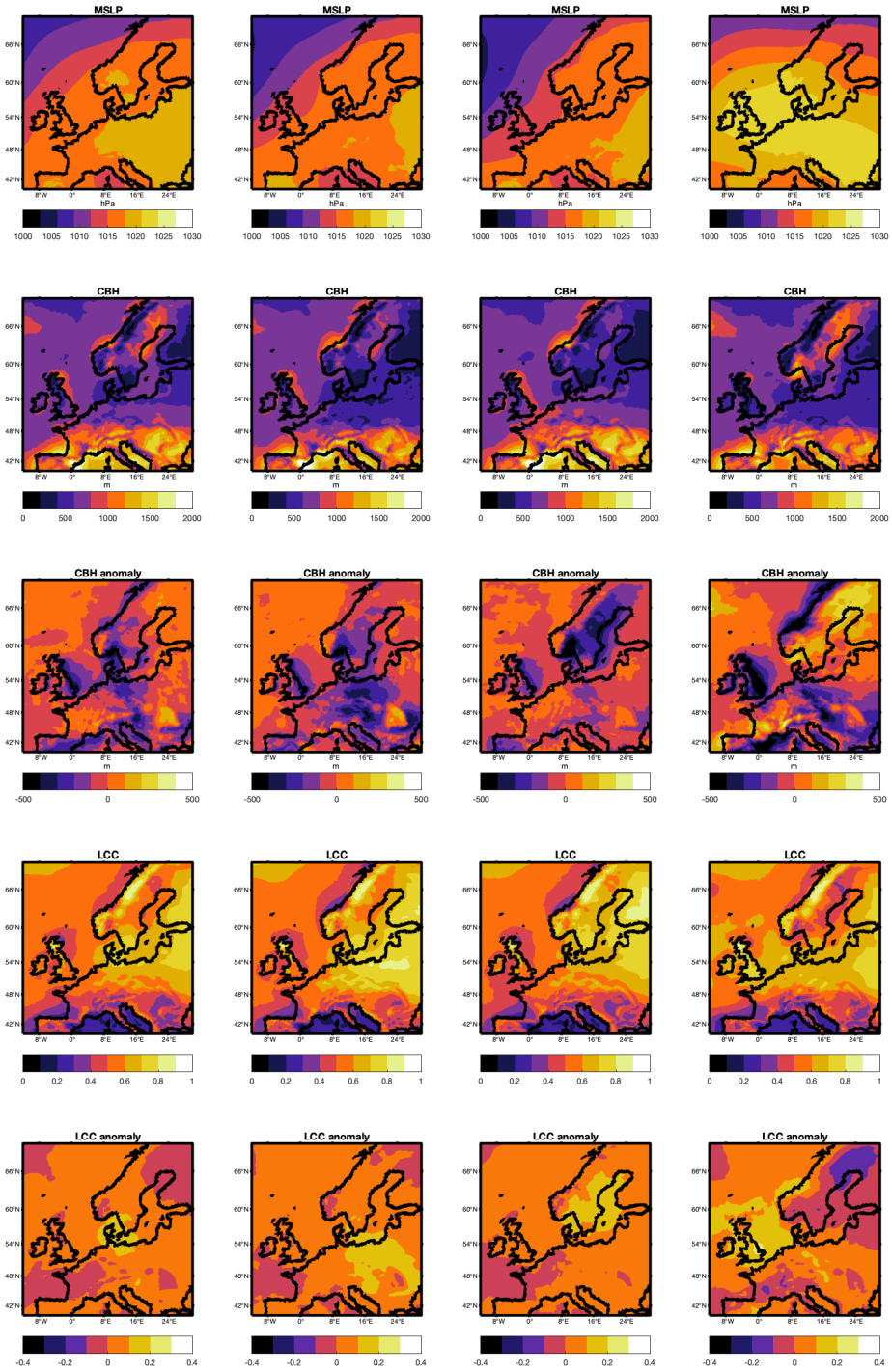

Figure 3.6: Map of mean sea level pressure (MSLP, top row), cloud base height (CBH, second row), CBH anomaly (third row), low cloud cover (LCC, fourth row), and LCC anomaly (bottom row) during Dunkelflaute periods in Denmark (**left** column), Poland (**middle-left** column), Sweden (**middle-right** column), and the UK (**right** column), respectively. Anomaly maps were created by subtracting the monthly mean values from mean values when Dunkelflaute occurs.

3.5 Spatial Correlation and Grid Connection

In this section, we quantify the spatial correlation of Dunkelflaute occurrences in eleven different European countries bordering the North and Baltic Sea areas. We used a binary flag (0 or 1) to represent non-Dunkelflaute and Dunkelflaute events (lasting more than one day) respectively, in individual countries, and calculated the Pearson correlation coefficient between each pair of the eleven countries. Although this metric is normally used for real numbers, it is also suitable for binary variables [74].

As shown in Figure 6.1, the correlation coefficients for Dunkelflaute events occurring in neighboring countries are about 0.3–0.4, with a peak magnitude of 0.5–0.6 for the Netherlands and Belgium, and Denmark and Sweden. This suggests that Dunkelflaute events can happen simultaneously over a relatively large area covering several countries. On the other hand, it is clear that Dunkelflaute periods are less correlated for those countries relatively far away from each other. Taking the UK as an example, when Dunkelflaute occurs there, there is a considerably lower probability of simultaneous Dunkelflaute occurrence in the Northern and central parts of Europe, such as in Finland and Poland.

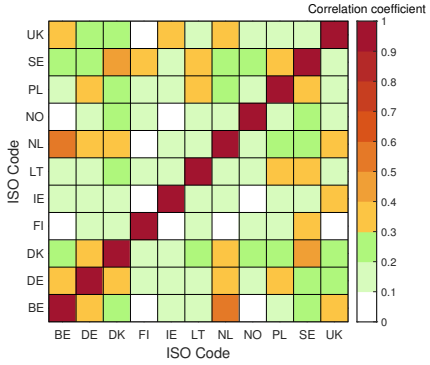

Figure 3.7: Correlation coefficients of Dunkelflaute occurrences between eleven European countries.

From Figure 6.1, we can conclude that Dunkelflaute events rarely occur simultaneously in all eleven countries considered. Several multi-national power grid schemes have been proposed in Europe to benefit from integrated systems, such as the North Sea Offshore Grid project, which is expected to connect offshore renewable energy resources around the North Sea area [6], and the Baltic Energy Market Interconnection Plan, linking nine countries surrounding the Baltic Sea [51]. Therefore, it is interesting to consider what benefit can be gained from an interconnected European system of the eleven countries of interest studied here regarding the occurrence of Dunkelflaute events.

Figure 3.8 shows the reduction in the frequency of Dunkelflaute events (duration of longer than one day) for the eleven individual countries compared to an interconnected system where the wind and PV generation are pooled. The mean frequency of Dunkelflaute (marked as a black horizontal line) is decreased from 3–9% for the individual countries to approximately 3.5% when interconnected. Furthermore, the maximum frequency (marked as a blue '+' symbol) is about 6.5% if power systems are interconnected, whereas individual countries can have frequency extremes of 6–14% of Dunkelflaute events. Pooling wind

and PV generation through interconnection would seem to benefit most of the countries studied, especially Sweden and the Netherlands. The exceptions are Norway and the UK, where there seems to be only marginal or no benefit for these countries.

The right panel of Figure 3.8 provides further evidence for the benefits of interconnecting countries into a large power system. Taking four countries: Germany, Norway, Sweden, and the UK, as an example, we can see a reduction in the frequency of Dunkelflaute events for the larger interconnected power system, especially for those events that last for several consecutive days.

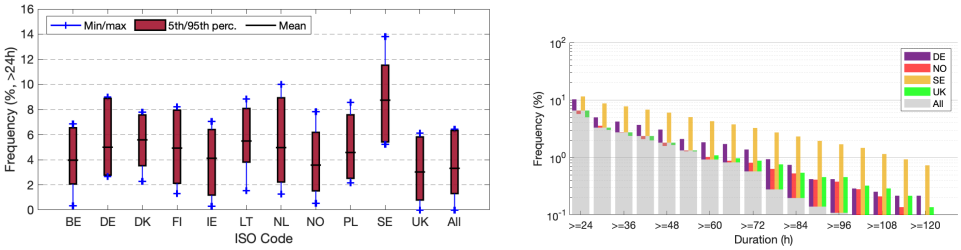

Figure 3.8: **Left** panel: frequency boxplot of Dunkelflaute events (longer than a day) for individual countries and where wind and PV generation are pooled in an interconnected system of eleven countries (labeled as 'All'). **Right** panel: frequency distribution of Dunkelflaute events for four representative countries (Germany (DE), Norway (NO), Sweden (SE), and the UK) and an interconnected system (labeled as 'All'). The frequency for the interconnected system is given by gray bars, while the frequency for the four individual countries is shown in color as a deviation from the magnitude of the interconnected system.

As illustrative examples, we used two Dunkelflaute events to quantify the benefits that can be gained through the interconnection into a larger power system of eleven countries (see Figure 3.9). The Dunkelflaute periods are marked as shaded gray regions under the curves. The first event occurred almost simultaneously in Ireland and the UK during late November of 2007, as shown in the left panels of Figure 3.9. The underproduction of wind and solar power lasted for about three days, and the positive effects of an interconnected system are clearly shown by leveling the capacity factor for the entire system, especially the wind CF, and alleviating the impacts of the Dunkelflaute events in the two countries. The second Dunkelflaute event is depicted in the right panel of Figure 3.9. During the early part of November 2013, Denmark and Sweden experienced Dunkelflaute episodes. If operational, the interconnected system (labelled as 'All') would have been able to increase the capacity factors of both wind and solar and circumvent the Dunkelflaute events. In the literature, other benefits of interconnected systems have been demonstrated, including a relative reduction in wind power variability [75, 76, 77] and a reduction in flexibility requirements [12, 78].

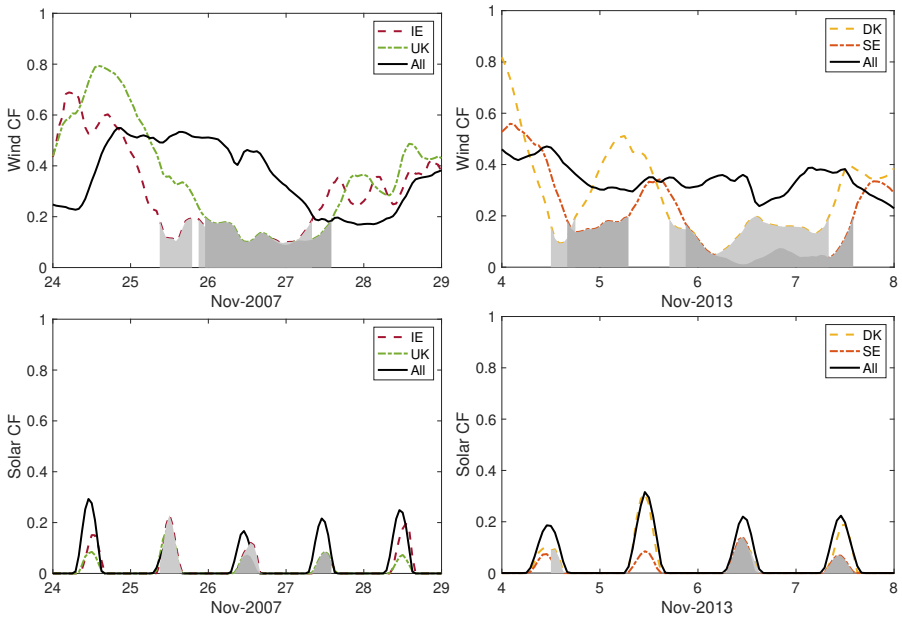

Figure 3.9: Time series of wind capacity factor (**top** panel) and solar capacity (**bottom** panel) during two cases of Dunkelflaute, which occurred in Ireland (IE), the UK (**left** panel), Denmark (DK), and Sweden (SE, **right** panel), respectively. The wind and solar CF are shown for the individual countries and an interconnected system of eleven countries (labeled as 'All'). The Dunkelflaute periods are demarcated by shaded gray regions. Different shades correspond to different countries.

3.6 Concluding Remarks

A climatological analysis of Dunkelflaute events was carried out for eleven countries bordering the North and Baltic Sea areas. Utilizing a wind and PV capacity factor threshold of 20%, we can conclude that substantial periods of Dunkelflaute lasting for at least a day occur each year. For example, there were approximately 2–10 events (duration of longer than one day) each year in three of the exampled countries, Germany, Norway, and the UK, and similar frequencies were also found in the other eight countries. Notably, there were a few cases lasting three or even five days. The largest frequency of Dunkelflaute events was seen in November, December, and January.

These events were shown to be typically characterized by near stationary large-scale high-pressure systems and extensive low cloud coverage, with a lower than average cloud base height. This confirms the association of the Dunkelflaute events and blocked regimes arising from the extensive high pressure, which can obstruct the westerly airflow into Europe and further result in the underproduction of wind energy in the neighboring countries. Furthermore, the occurrence of expansive low-level clouds was shown to be another characteristic of Dunkelflaute events, which further corroborates the previous finding that the high-pressure ridges between frontal systems are associated with the occurrence of stratocumulus clouds in mid-latitudes [71, 64]. Due to the relatively low solar radiation and shorter day lengths in winter (during which most Dunkelflaute events

occur), the limited solar energy production during the events can thus be well-explained.

Lastly, it was found that the correlation coefficients of Dunkelflaute events for neighboring countries were moderate (approximately 0.3–0.4). Simple analysis revealed that an interconnected power system where wind and PV generation are pooled can decrease the occurrence of Dunkelflaute events considerably. Our findings, albeit preliminary, can be of importance for reducing the risk of black-outs or the necessity for backup energy demands and costs to maintain system stability, especially for high renewable penetration in the near future.

References

[1] Bowen Li et al. "A brief climatology of dunkelflaute events over and surrounding the North and Baltic Sea areas". In: *Energies* 14.20 (2021), p. 6508.

[2] B. Matthias, G. Andreas, and G Patrick. "European Energy Transition 2030: The Big Picture. Ten Priorities for the next European Commission to meet the EU's 2030 targets and accelerate towards 2050". In: *URL: https://www. agoraenergiewende. de/en/publications/european-energytransition-2030-the-big-picture/* (2019), pp. 1–103.

[3] European Commission. "Report from the Commission to the European Parliament, the Council, the European Economic and Social Committee and the Committee of the Regions on the Implementation of EU Macro-Regional Strategies". In: (2019), pp. 1–12.

[4] European Commission. "Energy Roadmap 2050". In: (2012), pp. 1–20.

[5] M Müller et al. "Translate COP21-2045 outlook and implications for offshore wind in the North Seas". In: *ESMNL17412* (2017), pp. 1–21.

[6] European Commission. "Political Declaration on Energy Cooperation between the North Seas Countries". In: (2016), pp. 1–7.

[7] M Cecchinato. "Boosting offshore wind energy in the Baltic Sea". In: *Puneda, I. and Fraile, D., WindEurope Taskforce Baltic, available at: https://windeurope. org/wp-content/uploads/files/about-wind/reports/WindEurope-Boosting-offshore-wind. pdf (last access: 20 December 2021)* (2019).

[8] Hannah C Bloomfield et al. "Quantifying the increasing sensitivity of power systems to climate variability". In: *Environmental Research Letters* 11.12 (2016), p. 124025.

[9] Dirk J Cannon et al. "Using reanalysis data to quantify extreme wind power generation statistics: A 33 year case study in Great Britain". In: *Renewable Energy* 75 (2015), pp. 767–778.

[10] FJ Santos-Alamillos et al. "Analysis of spatiotemporal balancing between wind and solar energy resources in the southern Iberian Peninsula". In: *Journal of applied meteorology and climatology* 51.11 (2012), pp. 2005–2024.

[11] Philip E Bett, Hazel E Thornton, and Robin T Clark. "European wind variability over 140 yr". In: *Advances in Science and Research* 10.1 (2013), pp. 51–58.

[12] Matthias Huber, Desislava Dimkova, and Thomas Hamacher. "Integration of wind and solar power in Europe: Assessment of flexibility requirements". In: *Energy* 69 (2014), pp. 236–246.

[13] Karin van der Wiel et al. “Meteorological conditions leading to extreme low variable renewable energy production and extreme high energy shortfall”. In: *Renewable and Sustainable Energy Reviews* 111 (2019), pp. 261–275.

[14] James Oswald, Mike Raine, and Hezlin Ashraf-Ball. “Will British weather provide reliable electricity?” In: *Energy Policy* 36.8 (2008), pp. 3212–3225.

[15] S Zachary and CJ Dent. “Probability theory of capacity value of additional generation”. In: *Proceedings of the Institution of Mechanical Engineers, part O: Journal of risk and reliability* 226.1 (2012), pp. 33–43.

[16] Gareth P Harrison et al. “Capacity value of offshore wind in Great Britain”. In: *Proceedings of the Institution of Mechanical Engineers, Part O: Journal of Risk and Reliability* 229.5 (2015), pp. 360–372.

[17] Bowen Li et al. “Mesoscale modeling of a “Dunkelflaute” event”. In: *Wind Energy* 24.1 (2021), pp. 5–23.

[18] Bowen Li et al. “Quantifying the predictability of a ‘Dunkelflaute’event by utilizing a mesoscale model”. In: *Journal of Physics: Conference Series*. Vol. 1618. 6. IOP Publishing. 2020, p. 062042.

[19] NOS. *Netbeheerder moest groot inkopen om stroomtekort op te vangen*. https://nos.nl/artikel/2229787-netbeheerder-moest-groot-inkopen-om-stroomtekort-op-te-vangen.html. accessed on 4 November 2020. 2018.

[20] NRC. *Netbeheerder Tennet wendt landelijk stroomtekort af*. https://www.nrc.nl/nieuws/2018/04/30/landelijk-stroomtekort-afgewend-door-netbeheerder-tennet-a1601355. accessed on 4 November 2020. 2018.

[21] Frank Meinke-Hubeny et al. “Energy transition in Belgium–Choices and costs”. In: *EnergyVille in Opdracht van Febeliec: Genk, Belgium* (2017).

[22] Elia. *Electricity Scenarios for Belgium towards 2050, Elia’s Quantified Study on the Energy Transition in 2030 and 2040*. Tech. rep. Technical Report. Elia. Brussels, 2017.

[23] D Wetzel. *Die Dunkelflaute bringt Deutschlands Stromversorgung ans Limit*. https://www.welt.de/wirtschaft/article161831272/Die-Dunkelflaute-bringt-Deutschlands-Stromversorgung-ans-Limit.html. accessed on 4 November 2020. 2017.

[24] S Schultz. *Ist der Winter wirklich zu düster für den Ökostrom?* https://www.spiegel.de/wirtschaft/soziales/oekostrom-knapp-panikmache-mit-der-dunkelflaute-a-1133450.html. accessed on 4 November 2020. 2017.

[25] Stefan Pfenninger. “Dealing with multiple decades of hourly wind and PV time series in energy models: A comparison of methods to reduce time resolution and the planning implications of inter-annual variability”. In: *Applied energy* 197 (2017), pp. 1–13.

[26] Iain Staffell and Stefan Pfenninger. “The increasing impact of weather on electricity supply and demand”. In: *Energy* 145 (2018), pp. 65–78.

[27] Joakim Widén. "Correlations between large-scale solar and wind power in a future scenario for Sweden". In: *IEEE transactions on sustainable energy* 2.2 (2011), pp. 177–184.

[28] Philipp Grünewald et al. "The role of large scale storage in a GB low carbon energy future: Issues and policy challenges". In: *Energy Policy* 39.9 (2011), pp. 4807–4815.

[29] Andreas Schröder et al. "The integration of renewable energies into the German transmission grid—A scenario comparison". In: *Energy Policy* 61 (2013), pp. 140–150.

[30] Dominik Heide et al. "Seasonal optimal mix of wind and solar power in a future, highly renewable Europe". In: *Renewable Energy* 35.11 (2010), pp. 2483–2489.

[31] FJ Santos-Alamillos et al. "Combining wind farms with concentrating solar plants to provide stable renewable power". In: *Renewable Energy* 76 (2015), pp. 539–550.

[32] Stefan Pfenninger and James Keirstead. "Renewables, nuclear, or fossil fuels? Scenarios for Great Britain's power system considering costs, emissions and energy security". In: *Applied Energy* 152 (2015), pp. 83–93.

[33] Alexander Buttler et al. "Variability of wind and solar power–An assessment of the current situation in the European Union based on the year 2014". In: *Energy* 106 (2016), pp. 147–161.

[34] Guy Plaut and Eric Simonnet. "Large-scale circulation classification, weather regimes, and local climate over France, the Alps and Western Europe". In: *Climate Research* 17.3 (2001), pp. 303–324.

[35] P Yiou and M Nogaj. "Extreme climatic events and weather regimes over the North Atlantic: when and where?" In: *Geophysical Research Letters* 31.7 (2004).

[36] Markus G Donat et al. "Examination of wind storms over Central Europe with respect to circulation weather types and NAO phases". In: *International Journal of Climatology* 30.9 (2010), pp. 1289–1300.

[37] Laura Zubiate et al. "Spatial variability in winter NAO–wind speed relationships in western Europe linked to concomitant states of the East Atlantic and Scandinavian patterns". In: *Quarterly Journal of the Royal Meteorological Society* 143.702 (2017), pp. 552–562.

[38] Hazel E Thornton et al. "The relationship between wind power, electricity demand and winter weather patterns in Great Britain". In: *Environmental Research Letters* 12.6 (2017), p. 064017.

[39] Christian M Grams et al. "Balancing Europe's wind-power output through spatial deployment informed by weather regimes". In: *Nature climate change* 7.8 (2017), pp. 557–562.

[40] HC Bloomfield et al. "The changing sensitivity of power systems to meteorological drivers: a case study of Great Britain". In: *Environmental Research Letters* 13.5 (2018), p. 054028.

[41] D Pozo-Vázquez et al. "NAO and solar radiation variability in the European North Atlantic region". In: *Geophysical Research Letters* 31.5 (2004).

[42] Ellsworth G Dutton et al. "Long-term variations in the occurrence and effective solar transmission of clouds as determined from surface-based total irradiance observations". In: *Journal of Geophysical Research: Atmospheres* 109.D3 (2004).

[43] Ellsworth G Dutton et al. "Decadal variations in surface solar irradiance as observed in a globally remote network". In: *Journal of Geophysical Research: Atmospheres* 111.D19 (2006).

[44] Arturo Sanchez-Lorenzo, Josep Calbó, and Javier Martin-Vide. "Spatial and temporal trends in sunshine duration over Western Europe (1938–2004)". In: *Journal of Climate* 21.22 (2008), pp. 6089–6098.

[45] Marc Chiacchio and Martin Wild. "Influence of NAO and clouds on long-term seasonal variations of surface solar radiation in Europe". In: *Journal of Geophysical Research: Atmospheres* 115.D10 (2010).

[46] Karin van der Wiel et al. "The influence of weather regimes on European renewable energy production and demand". In: *Environmental Research Letters* 14.9 (2019), p. 094010.

[47] A Watts. *Weather Wise: Reading Weather Signs*. Adlard Coles. London, 2013.

[48] CKM Douglas. "Clouds as seen from an aeroplane". In: *Q J Roy Meteor Soc* 46.195 (1920), pp. 233–242.

[49] Iain Staffell and Stefan Pfenninger. "Using bias-corrected reanalysis to simulate current and future wind power output". In: *Energy* 114 (2016), pp. 1224–1239.

[50] Stefan Pfenninger and Iain Staffell. "Long-term patterns of European PV output using 30 years of validated hourly reanalysis and satellite data". In: *Energy* 114 (2016), pp. 1251–1265.

[51] Energy and Climate Change Committee. "A European Supergrid". In: (2011).

[52] IRENA. "Renewable Energy Capacity Statistics 2015". In: *IRENA Renewable Energy Capacity Statistics* (2015), pp. 1–44.

[53] IRENA. "Renewable Capacity Statistics 2021". In: *IRENA Renewable Energy Capacity Statistics* (2021).

[54] Xi Lu and Michael B McElroy. "Global potential for wind-generated electricity". In: *Wind Energy Engineering*. Elsevier, 2017, pp. 51–73.

[55] RSHPO V. McKenna et al. "Cost-potentials for large onshore wind turbines in Europe". In: *Energy* 83 (2015), pp. 217–229.

[56] ENTSOE. *ENTSOE*. `https://www.entsoe.eu/data/`. accessed on 8 October 2021. 2021.

[57] Hans Hersbach et al. "The ERA5 global reanalysis". In: *Quarterly Journal of the Royal Meteorological Society* 146.730 (2020), pp. 1999–2049.

[58] Michael Allaby. *Encyclopedia of weather and climate*. Facts on File, 2007.

[59] J Weller and JE Thornes. "An investigation of winter nocturnal air and road surface temperature variation in the West Midlands, UK under different synoptic conditions". In: *Meteorological Applications* 8.4 (2001), pp. 461–474.

[60] David James Brayshaw et al. "The impact of large scale atmospheric circulation patterns on wind power generation and its potential predictability: A case study over the UK". In: *Renewable Energy* 36.8 (2011), pp. 2087–2096.

[61] Caroline R Ely et al. "Implications of the North Atlantic Oscillation for a UK–Norway renewable power system". In: *Energy Policy* 62 (2013), pp. 1420–1427.

[62] Helene Burningham and Jon French. "Is the NAO winter index a reliable proxy for wind climate and storminess in northwest Europe?" In: *International Journal of Climatology* 33.8 (2013), pp. 2036–2049.

[63] A Slingo and JM Slingo. "The response of a general circulation model to cloud longwave radiative forcing. I: Introduction and initial experiments". In: *Quarterly Journal of the Royal Meteorological Society* 114.482 (1988), pp. 1027–1062.

[64] AGM Driedonks and PG Duynkerke. "Current problems in the stratocumulus-topped atmospheric boundary layer". In: *Boundary-Layer Meteorology* 46.3 (1989), pp. 275–303.

[65] Antoni Viúdez-Mora et al. "Modeling atmospheric longwave radiation at the surface during overcast skies: The role of cloud base height". In: *Journal of Geophysical Research: Atmospheres* 120.1 (2015), pp. 199–214.

[66] Stephen G Warren et al. *Global distribution of total cloud cover and cloud type amounts over land.* Tech. rep. Washington Univ., Seattle (USA). Dept. of Atmospheric Sciences; Colorado …, 1986.

[67] SJ Caughey, BA Crease, and WT Roach. "A field study of nocturnal stratocumulus II Turbulence structure and entrainment". In: *Quarterly Journal of the Royal Meteorological Society* 108.455 (1982), pp. 125–144.

[68] A Slingo, R Brown, and CL Wrench. "A field study of nocturnal stratocumulus; III. High resolution radiative and microphysical observations". In: *Quarterly Journal of the Royal Meteorological Society* 108.455 (1982), pp. 145–165.

[69] SQJR Nicholls. "The dynamics of stratocumulus: Aircraft observations and comparisons with a mixed layer model". In: *Quarterly Journal of the Royal Meteorological Society* 110.466 (1984), pp. 783–820.

[70] S Nicholls and J Leighton. "An observational study of the structure of stratiform cloud sheets: Part I. Structure". In: *Quarterly Journal of the Royal Meteorological Society* 112.472 (1986), pp. 431–460.

[71] PG Duynkerke and AGM Driedonks. "A model for the turbulent structure of the stratocumulus–topped atmospheric boundary layer". In: *Journal of Atmospheric Sciences* 44.1 (1987), pp. 43–64.

[72] Dennis L Hartmann, Maureen E Ockert-Bell, and Marc L Michelsen. "The effect of cloud type on Earth's energy balance: Global analysis". In: *Journal of Climate* 5.11 (1992), pp. 1281–1304.

[73] Robert Wood. "Stratocumulus clouds". In: *Monthly Weather Review* 140.8 (2012), pp. 2373–2423.

[74] Bin Zhang and Sargur N Srihari. "Properties of binary vector dissimilarity measures". In: *Proc. JCIS Int'l Conf. Computer Vision, Pattern Recognition, and Image Processing*. Vol. 1. 2003.

[75] Willett Kempton et al. "Electric power from offshore wind via synoptic-scale interconnection". In: *Proceedings of the National Academy of Sciences* 107.16 (2010), pp. 7240–7245.

[76] Mark Z Jacobson and Mark A Delucchi. "Providing all global energy with wind, water, and solar power, Part I: Technologies, energy resources, quantities and areas of infrastructure, and materials". In: *Energy policy* 39.3 (2011), pp. 1154–1169.

[77] Hannele Holttinen et al. "Wind and load variability in the Nordic countries". In: *VTT Technology* 96 (2013).

[78] Sarah Becker et al. "Transmission grid extensions during the build-up of a fully renewable pan-European electricity supply". In: *Energy* 64 (2014), pp. 1404–1418.

4

Automated Identification of 'Dunkelflaute' Events

As wind and solar power play increasingly important roles in the European energy system, unfavourable weather conditions, such as 'Dunkelflaute' (extended calm and cloudy periods), will pose ever greater challenges to transmission system operators. Thus, accurate identification and characterization of such events from open data streams (e.g., reanalysis, numerical weather prediction, and climate projection) are going to be crucial.

In this study, we propose a two-step, unsupervised deep learning framework (named WISRnet) to automatically encode spatial patterns of wind speed and insolation, and subsequently, identify Dunkelflaute periods from the encoded patterns. Specifically, a deep convolutional neural network (CNN)-based autoencoder (AE) is first employed for feature extraction from the spatial patterns. These two-dimensional CNN-AE patterns encapsulate both amplitude and spatial information in a parsimonious way. In the second step of the WISRnet framework, a variant of the well-known k-means algorithm is used to divide the CNN-AE patterns in region-dependent meteorological clusters.

For the validation of the WISRnet framework, aggregated wind and solar power production data from Belgium are used. Using a simple criterion from published literature, all the Dunkelflaute periods are directly identified from this six year-long dataset. Next, each of these periods is associated with a WISRnet-derived cluster. Interestingly, we find that the majority of these Dunkelflaute periods are part of only five clusters (out of twenty five). We show that in lieu of proprietary power production data, the WISRnet framework can identify Dunkelflaute periods from public-domain meteorological data. To further demonstrate the prowess of this framework, it is deployed to identify and characterize Dunkelflaute events in Denmark, Sweden, and the UK.

This chapter is partly based on *Li, B., Basu, S., and Watson, S. J. (2022). Automated Identification of "Dunkelflaute" Events: A Convolutional Neural Network–Based Autoencoder Approach. Artificial Intelligence for the Earth Systems, 1(4), e220015.* [1].

4.1 Introduction

With wind and solar power becoming major contributors to the European energy system, it is crucial to identify and characterize extreme weather events, which may significantly affect power production. Simultaneous low levels of wind and solar power production during Dunkelflaute events are causing increasing concern [2, 3, 4, 5, 6]. These events occur several times each year, predominately during winter months, in northern European countries and sometimes last for several days [5]. They can challenge transmission system operators in terms of balancing supply and demand of electricity. Therefore, a reliable way to identify, characterize, and eventually forecast Dunkelflaute events becomes a necessity.

One of the first peer-reviewed studies on Dunkelflaute was conducted by [6]. They investigated the capability of contemporary mesoscale models to simulate Dunkelflaute events. In a follow-up study [5], they documented a brief climatology of Dunkelflaute events for countries surrounding the North and Baltic seas. They utilized aggregated power production data for the identification of Dunkelflaute cases. Owing to their proprietary nature, renewable power production data are often not easily accessible for research. Furthermore, due to the young age of the renewable energy industry, only a limited amount of historical power production data are available from most countries. In contrast, long-term (ranging from mid-1800 to 2100), gridded meteorological data (e.g., reanalysis, numerical weather forecast, and climate projection) are readily available in the public domain. In the present study, we develop a machine learning (ML)-based approach which can ingest these types of open data streams, and in turn, can automatically identify Dunkelflaute events.

In recent years, ML algorithms have been widely used in many fields for learning intricate structures from large datasets [7, 8]. For example, in the field of earth science, ML has been proven useful in numerous applications, such as cloud image classification [9, 10], land surface classification [11], ozone profile shape estimation [12], weather prediction [13, 14, 15, 16], *etc.* Moreover, ML techniques have shown their potential for identifying certain types of prominent weather patterns like tropical cyclones, fronts, and atmospheric rivers in large climate datasets [17, 18]. To the best of our knowledge, the present study is the first ML-based study of the Dunkelflaute phenomenon.

The rest of the paper is organized as follows. In Section 2, we discuss a few ML algorithms which are relevant for the proposed WISRnet framework. The datasets used in the numerical experiments are described in Section 3. In Section 4, we delve into the WISRnet framework. Clustering and validation results are documented in Section 5 followed by a summarized discussion in Section 6. In-depth technical details and various sensitivity studies are reported in five appendices.

4.2 Overview of Relevant Machine Learning Algorithms

Machine learning refers to the automatic extraction of useful information or the learning of a specific task from given input data [19]. It has two basic forms: supervised and unsupervised learning. Supervised learning utilizes known inputs and corresponding labeled ground truth data [20]. In contrast, unsupervised learning discovers groups of items in the data using unlabelled instances [21]. In this research, given the unavailability of labeled data, we use an unsupervised method for the purpose of Dunkelflaute identification.

In the atmospheric science literature, several unsupervised clustering methods, including k-means, hierarchical clustering, and self-organizing maps, have been used for classification of synoptic weather patterns [22, 23, 24, 25, 26]. In addition, they have been found useful in explaining trends in extreme temperatures [27] and facilitating weather forecasts [28, 29, 30]. They are also popular for identifying extreme weather patterns [31, 32, 33], wind power prediction [34, 35], and other meteorological applications [36, 37, 38].

In parallel to classical unsupervised ML approaches, in recent years, supervised convolutional neural networks (CNNs) have demonstrated their strengths in pattern classification. They have achieved excellent results in object detection and pattern recognition [39, 7]. CNNs can automatically learn and extract representative features from multi-dimensional datasets, such as images and videos. They achieve high accuracy in classifying complex geophysical patterns, like clouds [10], ice crystal [40], land surface type [11], and volcano deformation [41]. These examples show the benefits of supervised CNN. However, labeled datasets are often not available for various applications [41, 33]. Thus, it is necessary to investigate the capability of CNNs implemented in an unsupervised manner. Recently, unsupervised CNNs have been used for classifying cloud organizations [42]. In another application [43], it has been utilized for creating flood inundation maps from synthetic aperture radar images.

Instead of unsupervised learning, a handful of recent studies exploited a new ML paradigm called self-supervised learning [44, 45]. In this approach, the labels are automatically generated either by a separate pre-trained model [46] , or via common image transformations [47].

Clustering large datasets with high-dimensional feature vectors is a challenging task. The feature vectors may be nonlinear and/or non-stationary; for geophysical problems, they often exhibit multiscale behaviors. Various types of noise are also omnipresent. In some cases, the smaller scales may not be very relevant for the global characterizations. Under these circumstances, brute-force learning and clustering of the high-dimensional feature vectors may lead to overfitting and reduced generalization. To circumvent this problem, a type of unsupervised neural network, known as an autoencoder [48, 49, 50], can be first employed. Autoencoders do not require any labels as their sole objective is to extract important features from high-dimensional inputs. They map the inputs to outputs via encoding with minimal loss of information. In atmospheric science literature, a few studies have clustered weather patterns and extremes using CNN-based AE algorithms [18, 33, 51] and produced promising results. In this study, we develop a new CNN–AE architecture to automatically compress spatial wind speed and insolation patterns into low-dimensional encoded patterns. More technical information on an AE is provided in Appendix A.

The encoded CNN-AE patterns are then clustered via the k-means algorithm. Since Dunkelflaute events are geographically localized phenomena, their clustering should account for spatial information. Thus, we make use of a geographically-dependent k-means algorithm. In principle, more advanced clustering techniques (e.g., self-organizing maps) can be utilized instead of k-means; however, we opted for this well-known approach for its simplicity. Advantages and disadvantages of various clustering algorithms can be found in [31].

4.3 Description of Datasets

The performance of deep learning models typically (with some exceptions) depend on the availability of high-quality training data. In-situ wind speed and insolation data are often collected at sparse locations; the data records are usually short in duration, and might suffer from temporal discontinuities. The measurements are also susceptible to terrain effects (e.g., shadowing) and measurement errors. In order to avoid these issues, in this proof-of-concept study, we use the ERA5 reanalysis dataset from the European Centre for Medium Range Weather Forecasts [52]. This global reanalysis has the highest temporal (hourly) and spatial resolution (~31 km) amongst its contemporaries. More importantly, in previous Dunkelflaute research [5, 6], this dataset was shown to be very reliable for capturing numerous traits of Dunkelflaute events.

In this study, we use hourly wind speed data from 100 m above ground level (AGL) and downward short-wave radiation flux (insolation) at the surface. The time-period of interest is from year 2009 to year 2018. For both the variables, the sample size is 86,904. We concentrate our analysis over the North Sea and neighbouring countries given the massive amount of ongoing and proposed wind farm installations in this region. Specifically, our domain of interest covers the region 46.75° to 62.5° north and -12° to 19.75° east (consisting of 64 × 128 latitude-longitude grid points). An illustrative example of a Dunkelflaute event is shown in Figure 5.4. This event occurred on January 16th, 2017 over Belgium and caused a significant drop in renewable power generation [53].

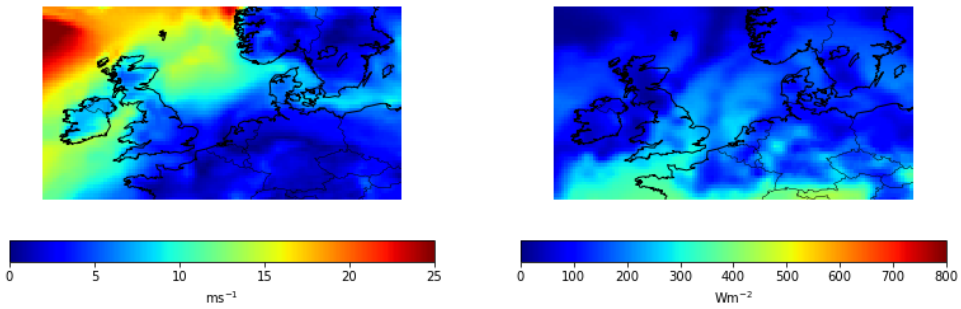

Figure 4.1: Spatial fields of 100-m wind speed (left panel) and downwelling shortwave radiation (insolation) at the surface (right panel) at 12 UTC on January 16th, 2017. On this day, a Dunkelflaute event occurred over Belgium causing a large shortfall in renewable power generation.

For the validation of our proposed clustering framework, we use aggregated wind and solar power production data from Belgium. These datasets along with information on installed capacity were provided by the Belgian system operator Elia (https://www.elia.be). The selected validation period is from 2013 to 2018 since the aggregated power production data is only available from 2013. We aggregate the measured power data from a sampling rate of 15 min to 60 min to be consistent with the hourly meteorological data from the ERA5 dataset. In [5], a particular sample is tagged as a Dunkelflaute event if both wind and solar power production fall below the threshold of 20% of their respective capacities during that 60 min period. They reported that Dunkelflaute events lasting more than one day

predominantly occur during the extended winter period (October-February). In the present work, for validation, we also use the same definition for labeling samples as Dunkelflaute or non-Dunkelflaute.

4.4 Methodology

4.4.1 Overview of the WISRnet framework

The deep learning (DL) architecture used to cluster weather patterns and identify Dunkelflaute events is shown in Figure 7.1. Henceforth, we refer to our framework as the WISRnet (WInd and SolaR network). For the training process, wind speed and insolation data are separately input into the CNN-AE model which 'learns' weather patterns. The encoder part of the CNN-AE consists of seven convolutional layers that encode the input characteristics. The last layer of the encoder (i.e., the encoded pattern) is sometimes called a bottleneck layer. Commonly, a 1-D fully connected (FC) layer is used as a bottleneck layer. However, 2-D encoded patterns can be easily projected to the underlying geographical map and then convolved with a spatially varying weight matrix (e.g., a 2-D Gaussian kernel). As a result, the 2-D patterns are well suited to identify features with spatial relationships. For this reason, in this study, we use a 2-D bottleneck layer.

In the literature, the decoder part of an AE is often just a mirror image of the encoder [54, 55]. However, there are exceptions. For example, [51] employed an asymmetric AE (named CapsNets) to predict the occurrence of cold and heat waves. Here, we use two FC layers and five convolutional layers in the decoder part to reconstruct input weather patterns. In contrast to the convolutional layers, the FC layers lose spatial information due to the flattening operation. However, their inclusion in the WISRnet architecture is justified as they clearly improve the overall quality of the reconstructed fields (more information is provided in Appendix B).

The accuracy of the CNN-AE model is assessed by comparing the input and the corresponding reconstructed patterns. Root-mean-squared error is used as a loss function.

The encoded patterns, resulting from respective wind speed and insolation inputs, are first normalized, and then, convolved with a 2-D Gaussian kernel. The center of the Gaussian kernel is prescribed based on the country of interest. For example, the geophysical center of Belgium (Latitude: 51.547°N and longitude: 4.610°E) is chosen as the kernel center, when we are identifying Dunkelflaute events in and around Belgium. Next, the convolved patterns are clustered using the k-means algorithm.

4.4.2 First Step of the WISRnet Framework: Spatial Pattern Extraction

Wind speed and insolation values are inputted to the CNN-AE model in the form of a 64×128 longitude-latitude grid (see Figure 5.4). Two CNN-AE models with different weights are trained for wind speed and insolation, respectively as depicted in Figure 7.1. There are seven convolutional layers in the encoding part with 4, 8, 16, 32, 256, 32, and 1 filter, respectively. Each convolution filter has a kernel size of 3×3 and zero padding is applied to keep the size constant in each layer. All layers are followed by a rectified linear unit (ReLU) activation function to introduce nonlinearity to the CNN-AE model [56]. For the first three convolutional layers, max-pooling (MP) with a kernel size of 2×2 and stride of 1

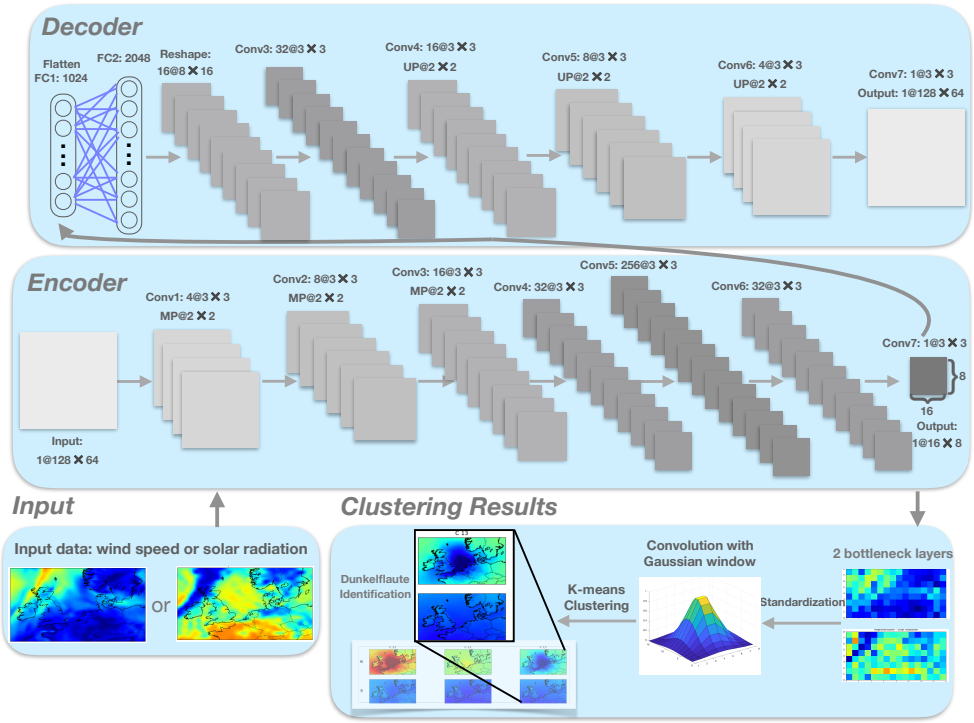

Figure 4.2: Schematic of the proposed WISRnet framework.

is used to effectively halve the dimensions of the data to enhance learning efficiency, while the last four layers are connected directly without pooling layers. The CNN-AE outputs a two-dimensional encoded pattern (aka the bottleneck layer) of dimensions 16×8 for both wind speed and insolation. Please refer to Appendix B regarding the accuracy of the CNN-AE model.

As mentioned earlier, we use an asymmetric CNN-AE framework. In the decoding part, there are two FC layers with 1024 and 2048 neurons followed by four convolutional layers. The number of filters used in the convolutional layers is 32, 16, 8, 4, 1, respectively; and there are three up-sampling layers between the layers to ultimately return to the input dimensions.

To evaluate the performance of the CNN-AE model, the ERA5 data are divided into three sets; where the first 80% of the samples are chosen for the training set, the following 10% of samples for the validation set, and the last 10% as the test set. The samples are contiguous in each set to avoid any information leakage across sets. The kernel filters are used for extracting characteristics, and they are updated using the back-propagation method. The adaptive moment estimation (Adam) is utilized as the optimizer [57]. The maximum number of epochs is set to 100 with a batch size of 128, and the validation loss is estimated after each epoch. The hyperparameters, including kernel size, number of filters, number of convolutional layers, and learning rate are optimised in terms of the lowest

validation loss and the highest accuracy in the reconstruction of the input fields. There is no visual evidence of overfitting in learning curves; furthermore, the application of dropout regularization did not improve the overall results. Please refer to Appendix B for further details.

4.4.3 Second Step of the WISRnet Framework: Weather Pattern Clustering

In [5], we reported that the correlation of Dunkelflaute occurrences in nearby areas decreases with increasing distance. Thus, we do not cluster the weather patterns for a specific country; rather, we use a spatially varying weight matrix for the entire domain of interest. First, the two encoded patterns (corresponding to wind speed and insolation fields) from the CNN-AE are standardized by subtracting the overall mean and normalized by overall standard deviations. Then, these normalized values are convolved with the following Gaussian kernel:

$$f(x,y) = \frac{1}{2\pi\sigma_x\sigma_y} e^{-\left[\frac{(x-\mu_x)^2}{2\sigma_x^2} + \frac{(y-\mu_y)^2}{2\sigma_y^2}\right]} \tag{4.1}$$

where μ_x and μ_y are the coordinates of the geographical center of interest. The variables σ_x and σ_y are related to region of influence in the x (longitudinal) and y (latitudinal) directions, respectively. Their prescribed values depend on the size of the country of interest. For an area the size of Belgium, a value of 1 was used for both σ_x and σ_y.

The k-means algorithm [58] is used to cluster the convolved CNN-AE patterns into 25 weather clusters. As discussed in Appendix C, we have found that 25 clusters are appropriate for the convergence of k-means clustering and identifying the most characteristic features of wind speed and insolation patterns.

Before discussing the results, we would like to emphasize that our region-dependent clustering technique is important for reducing the total number of clusters. Without this technique, the difference between Dunkelflaute in different countries will be difficult to distinguish with only twenty five clusters; please refer to Appendix D for more details.

In Appendix E, we use self-organizing map (SOM) as a baseline to cluster weather patterns and compare its results with the proposed WISRnet framework.

4.5 Results

4.5.1 Feature Extraction

Figure 4.3 shows an illustrative example from the validation set of an original (left), encoded (middle) and reconstructed (right) map of the wind speed and insolation fields. The encoded maps can be seen to capture the main features of wind speed and insolation maps, e.g., higher encoded values corresponding to higher wind speed or insolation. In addition, the CNN-AE patterns have similar spatial distributions as the original ones, which means that the location information is not lost. The reconstructed map is used to evaluate the performance of the CNN-AE. As seen in the illustrative example in Figure 4.3, the original wind speed and insolation field are reproduced well. For the entire validation set, the root mean squared errors between the original and the reconstructed values are 0.78 m s^{-1} and 24.62 W m^{-2} for the wind speed and insolation, respectively. Since the wind speed and solar radiation in the whole dataset can go up to about 44.57 m s^{-1} and 1010.85 W m^{-2}

with the average of 7.77 m s^{-1} and 123.46 W m^{-2}, respectively, the errors are moderately low.

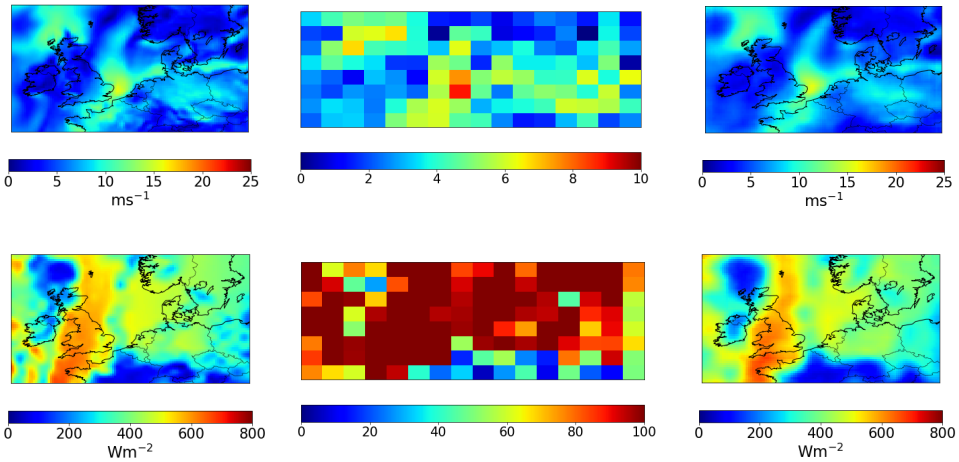

Figure 4.3: An illustrative example from the validation dataset of the original (left), encoded (middle) and reconstructed (right) maps of the wind speed (top panel) and insolation (bottom panel) fields from the CNN-AE. This is a randomly selected example (16 UTC on May 14th, 2018), and not a Dunkelflaute case.

4.5.2 Weather Pattern Clustering

In Figure 7.2, we show the clustering results of the CNN-AE patterns with the Gaussian weighting kernel centred on Belgium. For each of the 25 clusters, mean wind speed and insolation anomalies are calculated based on the 10-year mean values for all clusters. Different clusters exhibit different magnitudes and extent of wind speed and insolation with a clear focus over Belgium. From visual inspection, the clusters C2, C9, C12, C18, and C23 are most closely related to periods of simultaneous low wind speed and insolation over Belgium. These clusters (henceforth Top 5 clusters) seem to be the most suitable candidates for identifying cases of Dunkelflaute and will be analysed in the next section.

To illustrate how well the clusters capture the characteristics of individual events, in Figure 4.5, we show two randomly selected events for each of the Top 5 clusters associated with periods of Dunkelflaute. Actual values of wind speed and insolation are shown. For all ten events, low wind speeds and low levels of insolation are apparent over Belgium.

4.5.3 Identification and Verification

In Table 4.1, we examine how frequently Dunkelflaute events actually occur for each cluster and what fraction of events are Dunkelflaute events in each cluster based on actual Belgian wind and solar power generation data for the period 2013 to 2018. We classify a particular event as a Dunkelflaute event if both wind and solar power production fall below the

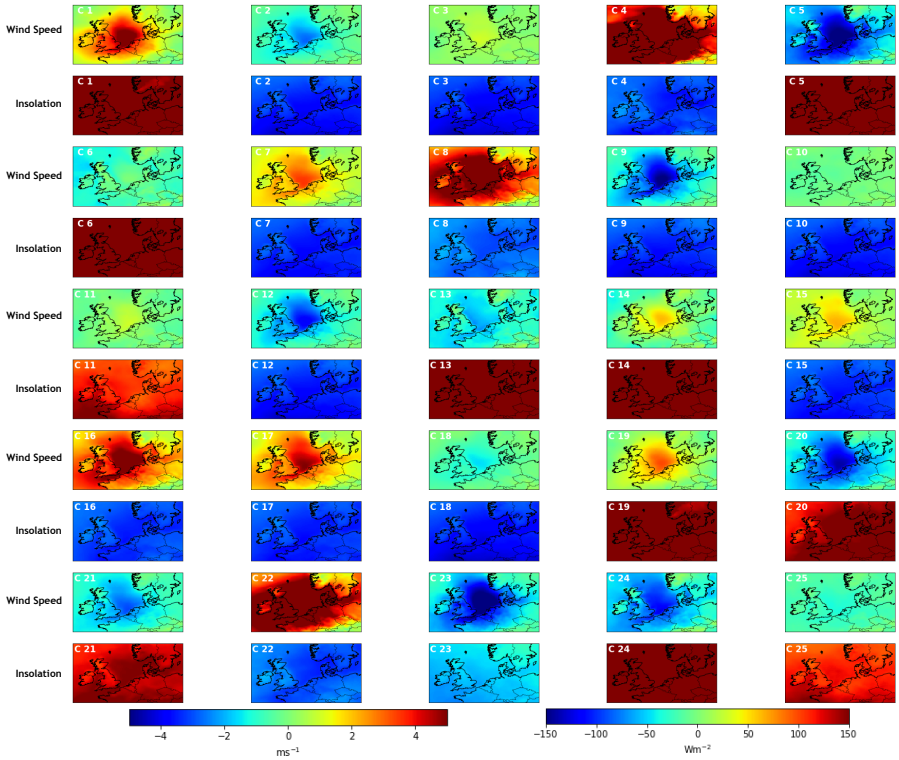

Figure 4.4: Anomalies of wind speed and insolation based on the 10-year mean for the 25 clusters (C1–C25) using the CNN-AE patterns. The Gaussian kernel is centred on Belgium.

threshold of 20% of their respective capacities [5]. Dunkelflaute periods are then matched to the appropriate cluster for that period. In the table, the DF time ratio is calculated as the ratio of Dunkelflaute events in each cluster to the total number of Dunkelflaute events. The events lasting longer than 12 hours or 24 hours are labeled as '> 12 h' and '> 24 h', respectively. The label 'All' is used in Table 4.1) to denote all events. The top five clusters in terms of DF time ratio are shown in bold. We would like to emphasize that these same five clusters were visually identified earlier as suitable candidates for identifying Dunkelflaute events. These five clusters account for 75% of all Dunkelflaute events greater than 12 hours, 69% of all such events greater than 24 hours, and 68% for all the events.

The mean wind and solar power capacity factors (CF) for each of the 25 clusters are also listed in Table 4.1. The capacity factor is defined as the fraction of wind and solar power production normalized by their respective installed capacities. For the C9, C12, and C23 clusters, the mean capacity factors are especially low, with values less than 10% for both wind and solar power. The mean solar power capacity factors for the C2 and C18 clusters are equally low, while wind power capacity factors for them are slightly higher.

To further illustrate the correlation of Dunkelflaute events to specific clusters, the fraction of Dunkelflaute events as a ratio of total events in each cluster, named Positive

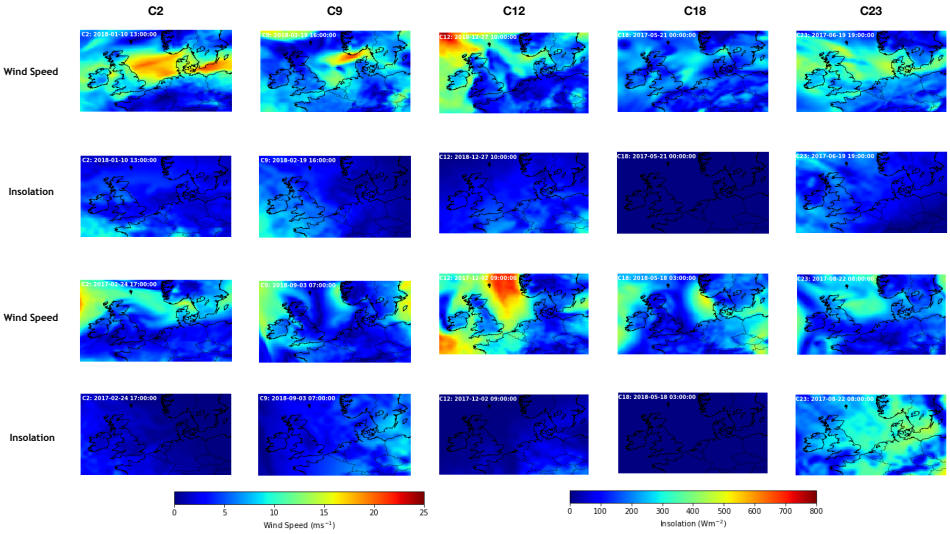

Figure 4.5: Two randomly selected events for each of the Top 5 clusters associated with periods of Dunkelflaute. Actual values (i.e., not anomalies) of wind speed and insolation are shown and the clusters are based on the CNN-AE patterns with the Gaussian kernel centred on Belgium.

Ratio, is shown in Table 4.1. This ratio is simply calculated by dividing the number of hourly Dunkelflaute samples by the total number of samples in a specific cluster. It can be seen that over 90% of the events in clusters C9, C12 and C23 are Dunkelflaute events. This would suggest that these clusters are a reliable indicator of whether an event is a Dunkelflaute event. Clusters C2 and C18 are a less reliable indicator but nonetheless indicate a high probability of an event being a Dunkelflaute event. Some level of incorrect clustering can be explained by overestimation of the magnitude of insolation in the ERA5 reanalysis [59, 60], especially for the cloudy days which are of interest for this work.

The Top 5 clusters all have mean capacity factors lower than 20%, which is exactly the threshold for defining Dunkelflaute. Thus, associating these clusters to Dunkelflaute events is rather straightforward. However, for three other clusters (C10, C20, and C21), such an inference cannot be drawn in a conclusive manner. These clusters have mean capacity factors marginally higher than the threshold of 20%. They also include a handful of Dunkelflaute events. Specifically, for Dunkelflaute events longer than 12 hours, the clusters C10, C20, and C21 have DF time ratio of 8%, 3%, and 3%, respectively. At the same time, they have positive ratio of only 25%, 32%, and 25%, respectively. Thus, if these clusters are identified as Dunkelflaute clusters, there will be a large number of false positive samples. In this study, we favored missing out on a few events instead of including too many non-Dunkelflaute events in our analysis.

Figure 4.6 shows the frequency of the capacity factors for the Top 5 Dunkelflaute clusters, as well as the plots for the 95^{th} percentile values for wind and solar power. It is clear that approximately 95% of the samples clustered in the C9, C12, and C23 clusters have capacity factors lower than 25%. While for the C2 and C18 clusters, most values lies within

Table 4.1: The correlation between periods of Dunkelflaute based on Belgian wind and solar power data and the clustered wind speed and insolation data between 2013 and 2018.

Cluster	DF Time Ratio			Mean Actual CF		Positive Ratio			Number of Samples
	>12 h	>24 h	All	Wind	Solar	>12 h	>24 h	All	
C1	0	0	0	0.6223	0.3070	0	0	0.0029	690
C2	**0.1701**	**0.1630**	**0.1654**	**0.1293**	**0.0138**	**0.5969**	**0.1715**	**0.8110**	**3773**
C3	0.0383	0.0517	0.0590	0.2929	0.0097	0.1405	0.0568	0.3026	3609
C4	0	0	0	0.7786	0.0344	0	0	0	237
C5	0.0030	0.0040	0.0025	0.0279	0.4732	0.0331	0.0132	0.0380	1209
C6	0.0016	0.0025	0.0018	0.2240	0.4413	0.0148	0.0070	0.0232	1420
C7	0.0047	0.0093	0.0081	0.4580	0.0177	0.0219	0.0128	0.0521	2880
C8	0	0	0	0.7245	0.0370	0	0	0	1526
C9	**0.1727**	**0.1600**	**0.1378**	**0.0595**	**0.0146**	**0.8822**	**0.2452**	**0.9846**	**2590**
C10	0.0751	0.0887	0.1017	0.2338	0.0126	0.2547	0.0903	0.4828	3898
C11	0.0100	0.0123	0.0152	0.2949	0.2068	0.0770	0.0286	0.1645	1714
C12	**0.1958**	**0.1539**	**0.1726**	**0.0986**	**0.0141**	**0.7397**	**0.1744**	**0.9118**	**3503**
C13	0.0026	0.0048	0.0028	0.1332	0.4684	0.0233	0.0127	0.0340	1499
C14	0.0003	0	0.0005	0.3510	0.4407	0.0046	0	0.0104	862
C15	0.0162	0.0245	0.0250	0.3741	0.0191	0.0645	0.0291	0.1393	3331
C16	0	0	0.0002	0.6418	0.0278	0	0	0.0020	2006
C17	0.0005	0.0017	0.0017	0.5503	0.0233	0.0026	0.0026	0.0115	2700
C18	**0.1259**	**0.1411**	**0.1379**	**0.1800**	**0.0106**	**0.4180**	**0.1405**	**0.6405**	**3986**
C19	0.0009	0.0012	0.0016	0.4637	0.2702	0.0102	0.0043	0.0247	1174
C20	0.0340	0.0322	0.0302	0.0592	0.2429	0.3189	0.0907	0.3955	1411
C21	0.0329	0.0315	0.0362	0.1053	0.2329	0.2469	0.0709	0.3808	1762
C22	0	0	0	0.7862	0.0316	0	0	0	987
C23	**0.0857**	**0.0761**	**0.0641**	**0.0362**	**0.0521**	**0.8873**	**0.2363**	**0.9280**	**1278**
C24	0.0022	0.0035	0.0020	0.0681	0.5155	0.0197	0.0095	0.0251	1472
C25	0.0275	0.0376	0.0335	0.1879	0.2108	0.1872	0.0768	0.3198	1939

about 40% capacities, confirming these clusters as less reliable indicators of Dunkelflaute events. Besides, as shown in Table 4.1, the mean wind power capacity factors for four out of these five Dunkelflaute clusters are larger than the mean solar power capacity factors, resulting in the relatively smaller values for the 95^{th} percentile for insolation.

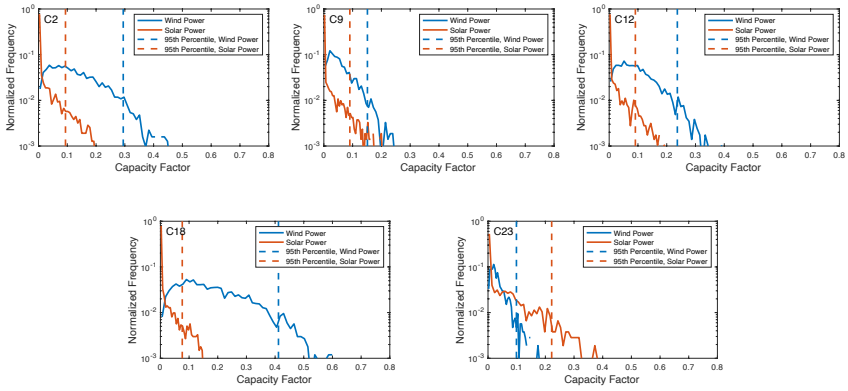

Figure 4.6: Normalized frequency of capacity factor for the Top 5 clusters associated with Dunkelflaute events. Aggregated power production data for the years 2013–2018 (data source: https://www.elia.be) are used for the analysis. From top left to bottom right the clusters are: C2, C9, C12, C18, and C23. Dashed lines represent the 95^{th} percentile values for wind and solar power.

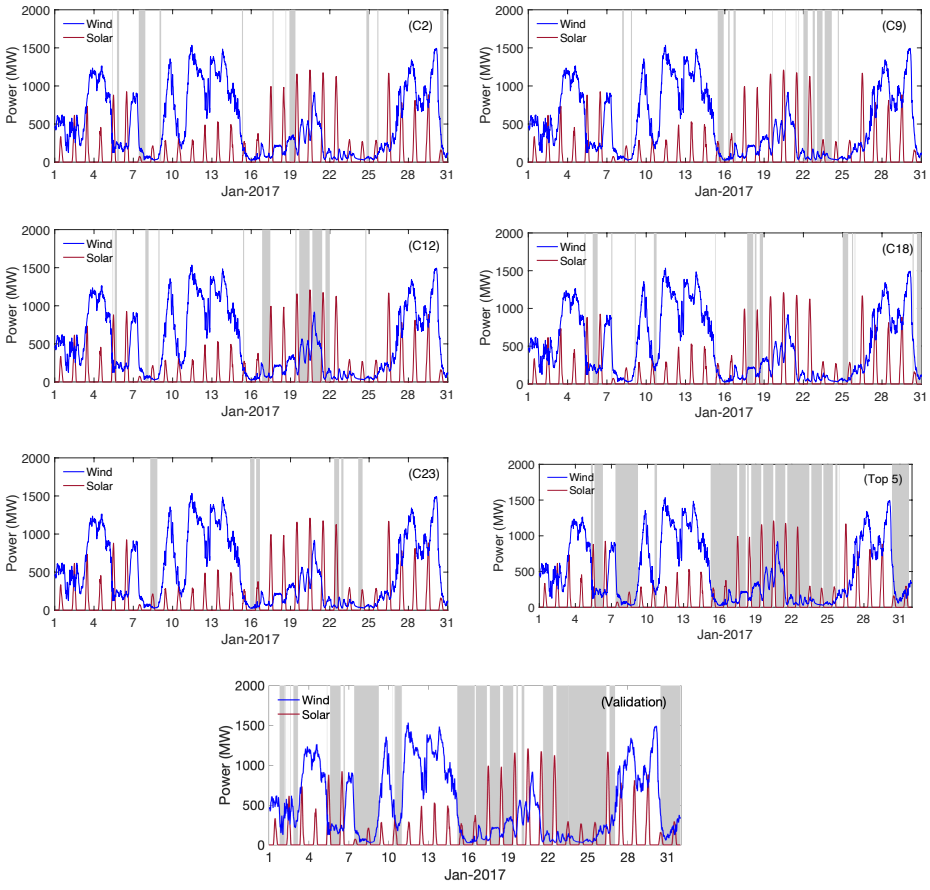

Figure 4.7: Time series of wind and solar energy production during January 2017 (data source: data source: https://www.elia.be). In the top six panels, the shaded gray regions represent the Dunkelflaute periods identified by the C2, C9, C12, C18, C23 clusters, respectively and all these periods combined (marked as 'Top 5'). In the bottom panel, the Dunkelflaute time is demarcated by a gray shade if both wind and solar power production fall below the threshold of 20% of their respective capacities using Elia data. This plot is used for validation.

Taking an actual Dunkelflaute case as an example, Figure 4.7 shows the aggregated wind and solar power production data for January 2017 [6]. Belgium experienced a total of nine days of Dunkelflaute in January 2017, during which flexibility options including more electricity generation from natural gas and additional power imports from neighboring countries were taken to circumvent the situation. The Dunkelflaute periods clustered in the individual five clusters identified previously (C2, C9, C12, C18, C23) and all these five clusters together (marked as 'Top 5') are marked as shaded gray regions in the top six panels of Figure 4.7. High correlation is seen between the Dunkelflaute periods based on actual power data (bottom panel of Figure 4.7) and the clustered wind speed and insolation data in Top 5 clusters. Each of the Top 5 clusters identified some segments of the Dunkelflaute event.

4.5.4 Identification of Dunkelflaute for Other European Countries

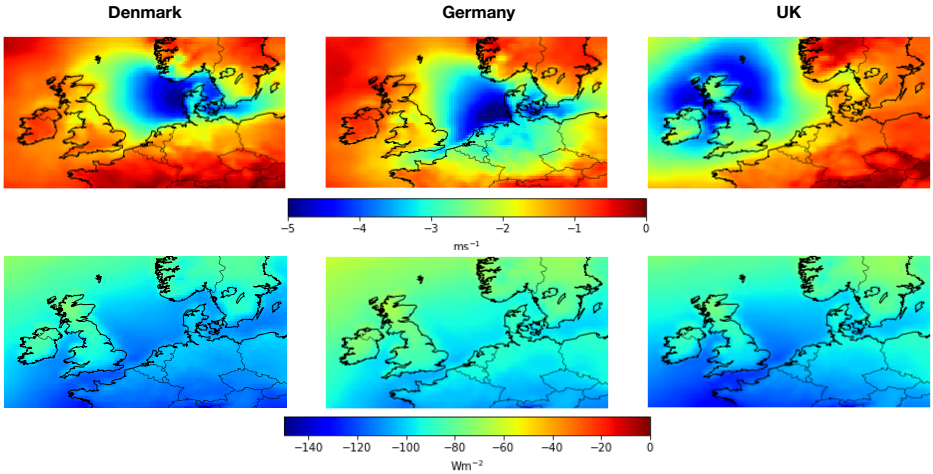

Figure 4.8: Anomalies of wind speed (top panel) and insolation (bottom panel) for weather patterns clustered as Dunkelflaute centered over Denmark (left panel), Germany Sweden (middle panel), and the UK (right panel).

The proposed WISRnet framework can also be applied to other countries to identify Dunkelflaute periods. Here, we utilize the framework for three additional countries: Denmark, Germany Sweden, and the UK. Anomalies of wind speed and insolation for the most representative clusters identified as Dunkelflaute are shown in Figure 4.8 for each of the three countries. Areas of anomalously low wind speed and insolation are clearly shown centred on the three countries of interest.

Taking Denmark as an example, the mean wind speed and insolation anomalies for 25 clusters are shown in Figure 4.9. The clustered patterns clearly focus on Denmark and several clusters are characteristic of Dunkelflaute periods, *i.e.*, C1, C21, and C24. For these three clusters, low wind speeds and insolation are present over Denmark and surrounding areas, covering a considerable part of the North Sea. It is also clear that negative anomalies

of insolation extend over almost the entire domain.

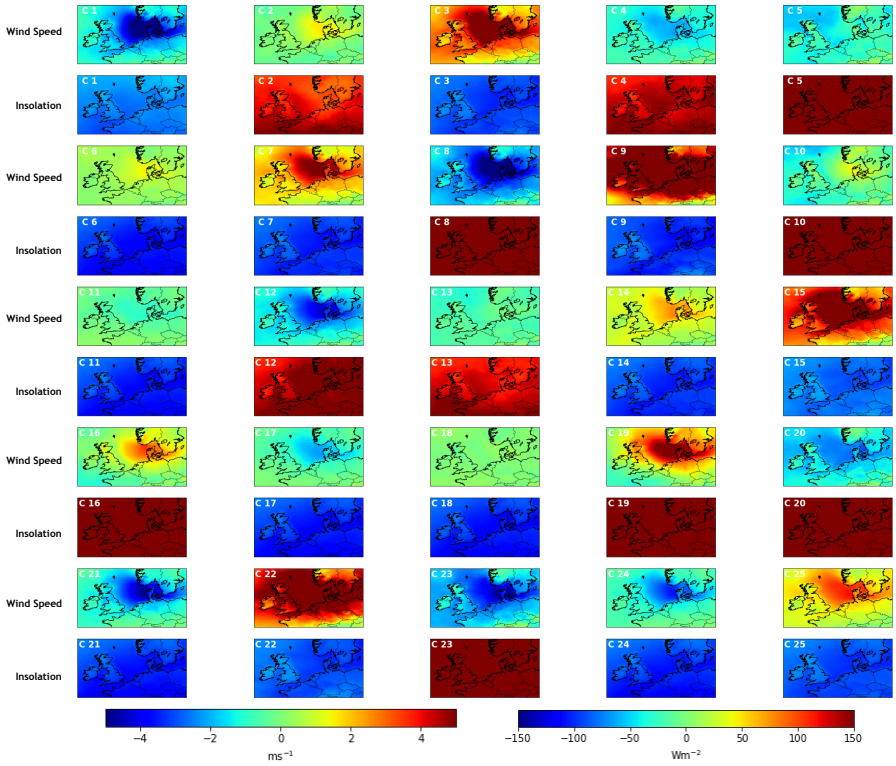

Figure 4.9: Similar to Fig. 7.2, except that the clustering algorithm is centered over Denmark.

4.6 Concluding Remarks

This paper is the first to demonstrate the capability of a machine learning-based framework (named WISRnet) for identifying Dunkelflaute events using public-domain wind speed and insolation data (e.g., reanalysis datasets). The crucial elements of the WISRnet are the CNN-AE architecture to extract the two-dimensional features from gridded weather data and the region-dependent k-means clustering. The combination of these elements enables the WISRnet to identify location-specific Dunkelflaute patterns. High accuracy is achieved when extracting encoded spatial patterns. Most importantly, excellent correspondence is seen between observed Dunkelflaute periods and those tagged as such using the WISRnet approach. Even though most of the present study has been focused on Belgium, the applicability of the WISRnet for other countries has also been briefly illustrated.

We believe that the clustering of Dunkelflaute events can be improved by including other types of meteorological data (e.g., satellite observations). In addition to wind speed and insolation, several other variables (e.g., mean sea level pressure, cloud base height, low cloud cover) are closely related to Dunkelflaute events [5]. The inclusion of some of

these variables might also enhance the overall performance of the WISRnet. Furthermore, other clustering methods (e.g., SOM) and other spatial weighting algorithms may be more effective than our current approach. We hope to experiment with some of these alternatives in our future work.

The WISRnet framework, with minor adjustments, can be used in conjunction with various climate projection datasets (e.g., CMIP5). By doing so, one will be able to quantify the impacts of climate change on the characteristics of the Dunkelflaute events. It is needless to say that any statistically significant trend in the Dunkelflaute events will be of critical importance for the designing and planning of next-generation power systems.

4.7 Appendix

4.7.1 Appendix A: Autoencoder

An autoencoder comprises of an encoder part and a decoder part. The encoding process transforms the input patterns to the bottleneck layer with compressed amplitude and spatial information. For a given input dataset $x \in \mathbf{R}^d$, a hidden layer in the encoder can be written as follows:

$$z = f(x) = \varphi(W_e x + b_1). \tag{4.2}$$

Here an encoder $f(\bullet)$ uses the activation function $\varphi(\bullet)$ to introduce the nonlinearity. When $z \in \mathbf{R}^s$, $W_e \in \mathbf{R}^{s \times d}$ and $b_1 \in \mathbf{R}^s$ are the weight matrix and bias value given to the input features, respectively. Here d and s refer to the size of inputted and encoded patterns, respectively.

Then the decoder recreates the input patterns by mapping the encoded patterns back to the input features as follows.

$$y = g(z) = \phi(W_d z + b_2), \tag{4.3}$$

where $g(z)$ indicates the mapping process between the hidden layer and the outputted features, and $\phi(\bullet)$ denotes the decoding activation function. $W_d \in \mathbf{R}^{d \times s}$ and $b_2 \in \mathbf{R}^d$ represents the weight matrix and bias term of the decoder. The reconstruction uses trainable parameters $\theta = \{W_e, W_d, b_1, b_2\}$. The goal of the autoencoder is to output the features y to be close to the input information a to the maximum extent. It can be achieved through training by minimizing a loss function:

$$J(\theta) = \sum_x L(x, y) = \sum_x L(x, g(f(x))), \tag{4.4}$$

where L represents the loss function which is used to measure the reconstruction error. A regularization term can also be added to avoid overfitting. The minimization of the error term is usually implemented by stochastic gradient descent.

4.7.2 Appendix B: Convolutional Neural Network (CNN)

The CNN used here is developed using the Tensorflow-Keras library [61, 62]. We have trained a number of CNNs including the symmetric architecture and asymmetric architecture of autoencoder, and several representatives are listed in the table 4.2. The best symmetric algorithms we trained, named CNN3-FC1, has three convolutional layers with 8, 16, and 32 filters, respectively. The final feature map is flattened first and then connected

to a dense layer that fully connected with 128 neurons. Regarding the asymmetric autoencoder algorithm, three representative structures, called Asym-CNN5, Asym-CNN7, and Asym-CNN10, use 5, 7, and 10 convolutional layers in the encoding part, respectively. The convolutional layers of Asym-CNN5 and Asym-CNN10 have 4, 8, 256, 32, 1 filters and 4, 8, 16, 32, 64, 128, 256, 256, 32, 1 filters, respectively. The Asym-CNN7 architecture is depicted in Figure 7.1. For these four CNNs, all the filters in the convolutional layers have a kernel size of 3×3 and the first three convolutional layers are all followed by a ReLU activation function and a max-pooling layer. The max-pooling layer uses a kernel size of 2×2 and a stride of 1. For the decoding part, CNN3-FC1 is the reverse structure of its encoder. The decoder structures for the other three have the same number of layers as their encoding counterpart, specifically, two fully-connected layers and 3, 5, and 8 convolutional layers, respectively.

Table 4.2: The RMSE between the input and the reconstructed patterns for nine different CNN-AE architectures.

	Learning Rate	Dropout	FC layer	Wind Speed (m/s)			Insolation (W/m^2)		
RMSE	-	-	1st layer	train	validation	test	train	validation	test
CNN3-FC1	0.001	-	1024	0.76	0.76	0.80	24.85	33.50	26.59
Asym-CNN5	0.001	-	1024	0.80	0.81	0.85	22.12	25.45	24.27
Asym-CNN7	0.0005	-	1024	0.78	0.78	0.82	21.09	24.88	23.40
Asym-CNN7	**0.001**	-	**1024**	**0.78**	**0.78**	**0.81**	**21.26**	**24.62**	**23.06**
Asym-CNN7	0.005	-	1024	4.47	4.48	4.52	193.74	191.82	200.13
Asym-CNN7	0.001	0.5	1024	1.36	3.42	3.39	39.26	109.59	113
Asym-CNN7	0.001	0.25	1024	1.13	1.95	1.96	30.31	61.82	62.76
Asym-CNN7	0.001	-	128	0.98	0.97	1.02	26.03	28.22	26.97
Asym-CNN10	0.001	-	1024	4.47	4.49	4.52	23.16	25.83	29.12

The RMSE between the input and the reconstructed wind speed and insolation patterns for training, validation and test sets for selected runs are listed in Table 4.2. Though the results of CNN3-FC1 is competitive, the application of symmetric architecture leads to a 1-D encoder and is not suitable for the 2-D clustering algorithm. We also investigated the influence of other hyperparameters like the number of convolutional layers (from 2 to 10), the number of filters (for example, 4, 8, 16 filters for the first convolutional layer), and the kernel size (3×3 to 7×7) of convolutional filters on the overall performance. It is found that the performance of an algorithm with less than 7 convolutional layers is not as satisfactory while using more than 7 convolutional layers can overfit the results. Overall, the best accuracy is from Asym-CNN7 (refer to Table 4.2).

The maximum number of epochs is set to 100 with a batch size of 128, and the accuracy performance is estimated after each epoch. The learning curves are shown in the two panels of Figure 4.10 which illustrated the change of loss with epochs for wind speed and insolation patterns using Asym-CNN7. It is found that after 60 epochs, the decrease of RMSE of wind speed and insolation patterns tends to be relatively negligible for validation sets.

A few sensitivity runs are performed with the Asym-CNN7 architecture to quantify the impacts of: (i) learning rate, (ii) dropout, and (iii) number of neurons in the fully connected (FC) layers. The best result with Asym-CNN7 is achieved with a learning rate of 0.001. For a larger learning rate (e.g., 0.005), the RMSE increases dramatically, while for a smaller learning rate (e.g., 0.0005), there is no further improvement in performance. To investigate the influence of regularization, a dropout rate of 0.5 and 0.25 is added to the

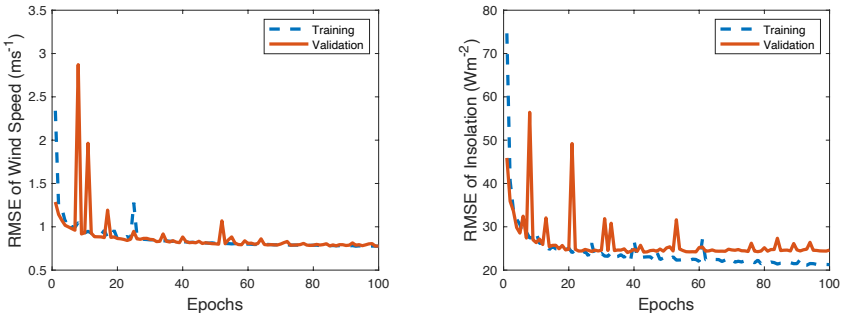

Figure 4.10: Examples of learning curves for wind speed (left panel) and insolation patterns (right panel). Loss is measured as RMSE between the input and the reconstructed wind speed and insolation patterns.

FC layers sequentially. With increasing dropout rates, the RMSE values increase. Thus, dropout is not deemed to be an effective regularization strategy for this particular problem. In order to quantify the importance of the FC layers, an additional sensitivity run was performed. In this run, the number of neurons in the two FC layers are decreased to 128 and 256, respectively. In contrast, in the default case, these FC layers have 1024 and 2048 neurons, respectively. It is evident from Table 4.2 that the RMSE of reconstruction increases considerably with the reduction of the neurons in the FC layers. In other words, the FC layers with sufficient complexity are needed to recreate the wind speed and insolation patterns accurately.

4.7.3 Appendix C: K-means Clustering

A clustering approach groups all the objects into some subsets of similar wind speed and insolation patterns. k-means clustering algorithm is widely used for its capability in clustering a great number of objects. It employs the squared error criterion of similarity which turns out to work well with a diversity of clusters [63]. The squared error function in a cluster is calculated as the sum of squares of the distance between the patterns in each cluster and the cluster center as follows.

$$e^2 = \sum_{j=1}^{K} \sum_{i=1}^{n_j} \| \mathbf{x}_{i,j} - \mathbf{c}_j \|^2 \tag{4.5}$$

where $x_{i,j}$ is the i^{th} sample in the j^{th} cluster. There are K clusters in total and each cluster has a centroid, e.g. c_j for the j^{th} cluster.

The clustering begins with a random partition and then assigns the samples to the closest cluster centroid by measuring the data similarity and distance between the samples and the cluster centers. Here the centroid is the mean value of the patterns in each cluster. Subsequently, the cluster centers are recomputed, and the reassignment continues until there is no additional reduction of squared point-to-centroid distance after several iterations.

The number of clusters K is specified a priori and will influence the performance of the criterion function. In this study, we use two competing approaches to estimate the optimal value of K.

First, we calculate inertia [64] to denote how well the data is clustered by k-means by summing the squared distances of samples to their closest cluster center. In the left panel of Figure 4.11, it can be seen that the K value of 20 to 30 is optimal with low inertia, and there is little improvement of squared distance when the number of clusters is larger than 30.

Next, the Davies-Bouldin index is used [65]; refer to the right panel of Figure 4.11. This index is defined as the average similarity of each cluster with the cluster most similar to it. Thus, the smaller magnitude of the index means that clusters are better separated, leading to better clustering. According to Figure 4.11 (right panel), the Davies-Bouldin index fluctuates somewhat erratically. There is a minimum corresponding to 2 clusters. For higher number of clusters, there is a general decreasing trend. However, it is not possible to estimate an optimal value of K from this plot. Hence, based on the inertia calculations, we opt for $K = 25$.

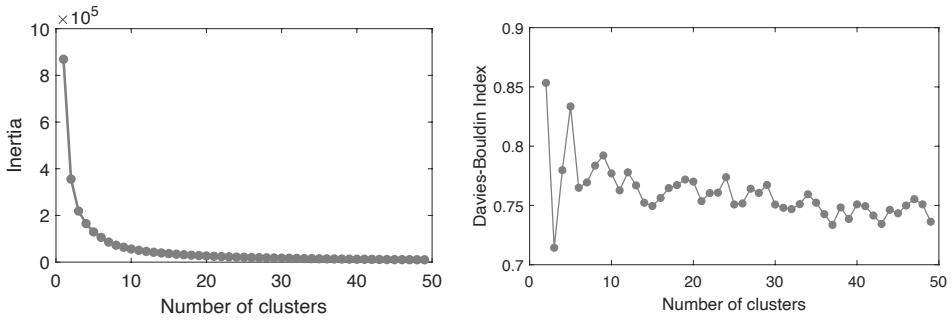

Figure 4.11: The change of inertia (left panel) and Davies–Bouldin index (right panel) vary as a function of the number of clusters.

4.7.4 Appendix D: K-means Clustering without using a Gaussian kernel

The region-dependent clustering technique aims to cluster weather patterns with a focus on a region or country of interest. A Gaussian kernel is used for convolution. In order to quantify the importance of this kernel, we document additional K-means clustering results in Figure 4.12. In this computation, we do not use a Gaussian kernel. This figure should be compared against Figure 7.2 where a Gaussian kernel is utilized. According to Figure 4.12, it is clear that several clusters (e.g., C3, C6, C21) represent simultaneous low wind speed and low insolation conditions. However, the spatial patterns are rather diffused instead of focused on a specific country.

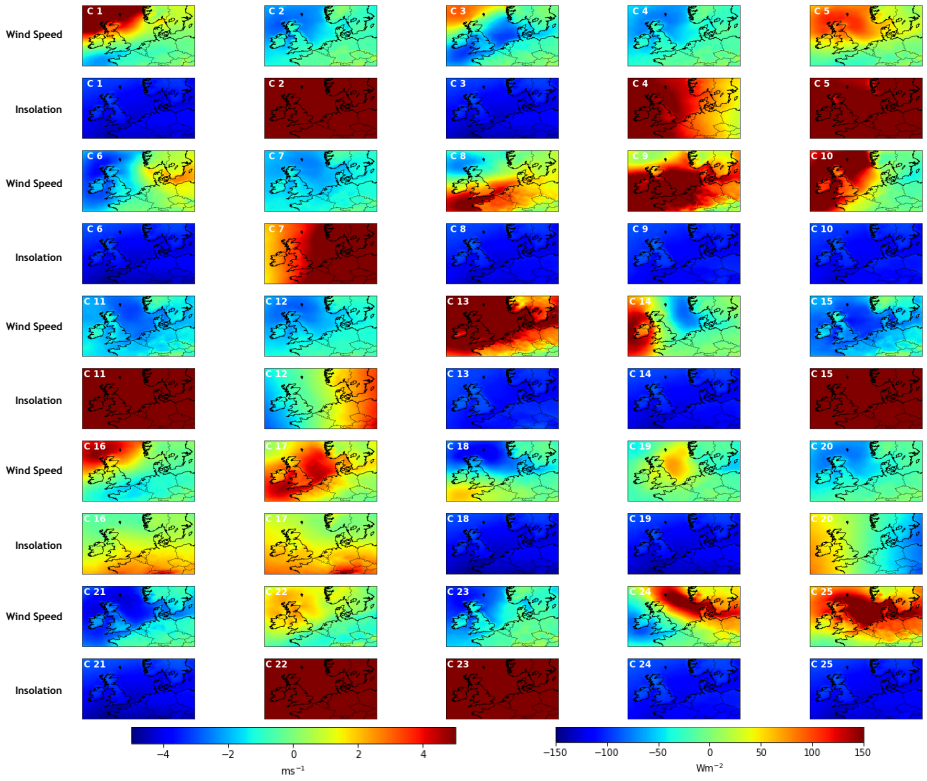

Figure 4.12: Anomalies of wind speed and insolation based on the 10-year mean for the 25 clusters (C1–C25) using the CNN-AE patterns. The Gaussian kernel is not included in the clustering technique.

Table 4.3: The positive ratio in each cluster based on Belgian wind and solar power data and the clustered wind speed and insolation data using SOM between 2013 and 2018. Here we include all events regardless of the duration.

Cluster	**S1**	S2	S3	S4	S5	S6	S7	S8	S9
Positive Ratio	**0.7112**	0.3125	0.3556	0.0063	0.0017	0.3195	0.0620	0.2352	0.1551
Cluster	S10	**S11**	S12	S13	S14	S15	**S16**	**S17**	S18
Positive Ratio	0.0840	**0.7868**	0.5177	0.5013	0.1134	0.0271	**0.7017**	**0.6470**	0.4068
Cluster	S19	S20	**S21**	S22	S23	S24	S25		
Positive Ratio	0.1068	0.0200	**0.6520**	0.4806	0.1323	0.0523	0.0282		

4.7.5 Appendix E: Self-Organizing Map

Self-organizing map (SOM) is a popular unsupervised machine learning approach and was originally developed by Kohonen [66, 67]. A SOM can extract nonlinear patterns from data, and as such, is more powerful than commonly used linear approaches (e.g., principal component analysis, empirical orthogonal functions). The SOM-based classifcations have been widely used in the atmospheric science field [27, 68, 69, 70, 71, 72]. In this appendix, we use SOM as a baseline to cluster wind speed and insolation patterns and compare its results with the WISRnet framework.

Before training a SOM network, wind speed and insolation data are first normalized and then concatenated together. The MiniSom package [73], is employed here with a 5 ×5 SOM grid. The total number of nodes in this grid determines the number of resulting clusters. Since our WISRnet framework uses 25 clusters, we use the same number of clusters with SOM. The learning rate of 0.01, neighborhood size of 1, and a high number of iterations of 1,000,000 are used in SOM implementation.

In Table 4.3, we examine the fraction of Dunkelflaute events as a ratio of total events in each cluster (Positive Ratio) based on actual Belgian wind and solar power generation data for the period 2013 to 2018. The top five clusters (S1, S11, S16, S17, and S21) in terms of positive ratio are shown in bold. It can be seen that approximately 70% of the events in clusters S1, S11, and S16 are Dunkelflaute events and there is a positive ratio of around 65% for S17 and S21. The clustering results using SOM are reasonably good; however, it underperforms compared to the WISRnet. In the case of WISRnet, there are three clusters with a positive ratio larger than 90%; one cluster above 80% and one at 64%.

The performance of the SOM approach may be improved by coupling it with a K-means clustering approach in conjunction with a Gaussian kernel-based convolution. Such an approach is beyond the scope of the present study.

References

[1] Bowen Li, Sukanta Basu, and Simon J Watson. “Automated Identification of “Dunkelflaute” Events: A Convolutional Neural Network–Based Autoencoder Approach”. In: *Artificial Intelligence for the Earth Systems* 1.4 (2022), e220015.

[2] Frank Meinke-Hubeny et al. “Energy transition in Belgium–Choices and costs”. In: *EnergyVille in Opdracht van Febeliec: Genk, Belgium* (2017).

[3] D Wetzel. “Die „Dunkelflaute “bringt Deutschlands Stromversorgung ans Limit”. In: *Die Welt “vom* 6 (2017). https://www.welt.de/wirtschaft/article161831272/Die-

Dunkelflaute-bringt-Deutschlands-Stromversorgung-ans-Limit.html. Accessed December 18, 2021., p. 2017.

[4] Bowen Li et al. "Quantifying the predictability of a 'Dunkelflaute'event by utilizing a mesoscale model". In: *Journal of Physics: Conference Series*. Vol. 1618. 6. IOP Publishing. 2020, p. 062042.

[5] Bowen Li et al. "A brief climatology of dunkelflaute events over and surrounding the North and Baltic Sea areas". In: *Energies* 14.20 (2021), p. 6508.

[6] Bowen Li et al. "Mesoscale modeling of a "Dunkelflaute" event". In: *Wind Energy* 24.1 (2021), pp. 5–23.

[7] Yann LeCun, Yoshua Bengio, and Geoffrey Hinton. "Deep learning". In: *nature* 521.7553 (2015), pp. 436–444.

[8] Ian Goodfellow et al. *Deep learning*. Vol. 1. 2. MIT press Cambridge, 2016.

[9] Cunzhao Shi et al. "Deep convolutional activations-based features for ground-based cloud classification". In: *IEEE Geoscience and Remote Sensing Letters* 14.6 (2017), pp. 816–820.

[10] Jinglin Zhang et al. "CloudNet: Ground-based cloud classification with deep convolutional neural network". In: *Geophysical Research Letters* 45.16 (2018), pp. 8665–8672.

[11] Congcong Li et al. "Comparison of classification algorithms and training sample sizes in urban land classification with Landsat thematic mapper imagery". In: *Remote sensing* 6.2 (2014), pp. 964–983.

[12] Jian Xu et al. "A novel ozone profile shape retrieval using full-physics inverse learning machine (FP-ILM)". In: *IEEE Journal of Selected Topics in Applied Earth Observations and Remote Sensing* 10.12 (2017), pp. 5442–5457.

[13] Amy McGovern et al. "Using artificial intelligence to improve real-time decision-making for high-impact weather". In: *Bulletin of the American Meteorological Society* 98.10 (2017), pp. 2073–2090.

[14] Gregory R Herman and Russ S Schumacher. "Money doesn't grow on trees, but forecasts do: Forecasting extreme precipitation with random forests". In: *Monthly Weather Review* 146.5 (2018), pp. 1571–1600.

[15] Stephan Rasp and Sebastian Lerch. "Neural networks for postprocessing ensemble weather forecasts". In: *Monthly Weather Review* 146.11 (2018), pp. 3885–3900.

[16] João Trevizoli Esteves, Glauco de Souza Rolim, and Antonio Sergio Ferraudo. "Rainfall prediction methodology with binary multilayer perceptron neural networks". In: *Climate Dynamics* 52.3 (2019), pp. 2319–2331.

[17] Yunjie Liu et al. "Application of deep convolutional neural networks for detecting extreme weather in climate datasets". In: *arXiv preprint arXiv:1605.01156* (2016).

[18] Evan Racah et al. "Semi-supervised detection of extreme weather events in large climate datasets". In: *arXiv preprint arXiv:1612.02095* (2016).

[19] Shai Shalev-Shwartz and Shai Ben-David. *Understanding machine learning: From theory to algorithms*. Cambridge university press, 2014.

[20] Sotiris B Kotsiantis, I Zaharakis, and P Pintelas. "Supervised machine learning: A review of classification techniques". In: *Emerging artificial intelligence applications in computer engineering* 160.1 (2007), pp. 3–24.

[21] Stefano Zanero and Sergio M Savaresi. "Unsupervised learning techniques for an intrusion detection system". In: *Proceedings of the 2004 ACM symposium on Applied computing*. 2004, pp. 412–419.

[22] Xinhua Cheng and John M Wallace. "Cluster analysis of the Northern Hemisphere wintertime 500-hPa height field: Spatial patterns". In: *Journal of atmospheric sciences* 50.16 (1993), pp. 2674–2696.

[23] DR Fereday et al. "Cluster analysis of North Atlantic–European circulation types and links with tropical Pacific sea surface temperatures". In: *Journal of Climate* 21.15 (2008), pp. 3687–3703.

[24] Susmitha Joseph et al. "Can El Niño–Southern Oscillation (ENSO) events modulate intraseasonal oscillations of Indian summer monsoon?" In: *Journal of Geophysical Research: Atmospheres* 116.D20 (2011).

[25] Ming Bao and John M Wallace. "Cluster analysis of Northern Hemisphere wintertime 500-hPa flow regimes during 1920–2014". In: *Journal of the Atmospheric Sciences* 72.9 (2015), pp. 3597–3608.

[26] AK Sahai et al. "A bias-correction and downscaling technique for operational extended range forecasts based on self organizing map". In: *Climate dynamics* 48.7-8 (2017), pp. 2437–2451.

[27] Daniel E Horton et al. "Contribution of changes in atmospheric circulation patterns to extreme temperature trends". In: *Nature* 522.7557 (2015), pp. 465–469.

[28] Laura Ferranti, Susanna Corti, and Martin Janousek. "Flow-dependent verification of the ECMWF ensemble over the Euro-Atlantic sector". In: *Quarterly Journal of the Royal Meteorological Society* 141.688 (2015), pp. 916–924.

[29] Robert Neal et al. "A flexible approach to defining weather patterns and their application in weather forecasting over Europe". In: *Meteorological Applications* 23.3 (2016), pp. 389–400.

[30] Sonja Totz et al. "Winter precipitation forecast in the European and Mediterranean regions using cluster analysis". In: *Geophysical Research Letters* 44.24 (2017), pp. 12–418.

[31] Richard Grotjahn et al. "North American extreme temperature events and related large scale meteorological patterns: a review of statistical methods, dynamics, modeling, and trends". In: *Climate Dynamics* 46.3 (2016), pp. 1151–1184.

[32] Nicolas Vigaud et al. "Multiscale variability in North American summer maximum temperatures and modulations from the North Atlantic simulated by an AGCM". In: *Journal of Climate* 31.7 (2018), pp. 2549–2562.

[33] Ashesh Chattopadhyay, Pedram Hassanzadeh, and Saba Pasha. "Predicting clustered weather patterns: A test case for applications of convolutional neural networks to spatio-temporal climate data". In: *Scientific reports* 10.1 (2020), pp. 1–13.

[34] Lei Dong et al. "Wind power day-ahead prediction with cluster analysis of NWP". In: *Renewable and Sustainable Energy Reviews* 60 (2016), pp. 1206–1212.

[35] Kejun Wang et al. "Deep belief network based k-means cluster approach for short-term wind power forecasting". In: *Energy* 165 (2018), pp. 840–852.

[36] John J Cassano et al. "Predicted changes in synoptic forcing of net precipitation in large Arctic river basins during the 21st century". In: *Journal of Geophysical Research: Biogeosciences* 112.G4 (2007).

[37] Nathaniel C Johnson, Steven B Feldstein, and Bruno Tremblay. "The continuum of Northern Hemisphere teleconnection patterns and a description of the NAO shift with the use of self-organizing maps". In: *Journal of Climate* 21.23 (2008), pp. 6354–6371.

[38] Sukyoung Lee and Steven B Feldstein. "Detecting ozone-and greenhouse gas–driven wind trends with observational data". In: *Science* 339.6119 (2013), pp. 563–567.

[39] Alex Krizhevsky, Ilya Sutskever, and Geoffrey E Hinton. "Imagenet classification with deep convolutional neural networks". In: *Advances in neural information processing systems* 25 (2012), pp. 1097–1105.

[40] Haixia Xiao et al. "Classification of ice crystal habits observed from airborne Cloud Particle Imager by deep transfer learning". In: *Earth and Space Science* 6.10 (2019), pp. 1877–1886.

[41] Nantheera Anantrasirichai et al. "Application of machine learning to classification of volcanic deformation in routinely generated InSAR data". In: *Journal of Geophysical Research: Solid Earth* 123.8 (2018), pp. 6592–6606.

[42] L Denby. "Discovering the importance of mesoscale cloud organization through unsupervised classification". In: *Geophysical Research Letters* 47.1 (2020), e2019GL085190.

[43] Xin Jiang et al. "Rapid and large-scale mapping of flood inundation via integrating spaceborne synthetic aperture radar imagery with unsupervised deep learning". In: *ISPRS Journal of Photogrammetry and Remote Sensing* 178 (2021), pp. 36–50.

[44] Longlong Jing and Yingli Tian. "Self-supervised visual feature learning with deep neural networks: A survey". In: *IEEE transactions on pattern analysis and machine intelligence* 43.11 (2020), pp. 4037–4058.

[45] Alexander Kolesnikov, Xiaohua Zhai, and Lucas Beyer. "Revisiting self-supervised visual representation learning". In: *Proceedings of the IEEE/CVF conference on computer vision and pattern recognition*. 2019, pp. 1920–1929.

[46] Bo Peng et al. "Urban Flood Mapping With Bitemporal Multispectral Imagery Via a Self-Supervised Learning Framework". In: *IEEE Journal of Selected Topics in Applied Earth Observations and Remote Sensing* 14 (2020), pp. 2001–2016.

[47] Diego Acuña-Escobar, Monserrate Intriago-Pazmiño, and Julio Ibarra-Fiallo. "Weather Recognition Using Self-supervised Deep Learning". In: *International Conference on Smart Technologies, Systems and Applications*. Springer. 2022, pp. 161–174.

[48] Geoffrey E Hinton and Richard S Zemel. "Autoencoders, minimum description length, and Helmholtz free energy". In: *Advances in neural information processing systems* 6 (1994), pp. 3–10.

[49] Evan Racah et al. “Extremeweather: A large-scale climate dataset for semi-supervised detection, localization, and understanding of extreme weather events”. In: *Advances in neural information processing systems* 30 (2017).

[50] Ganggang Dong et al. “A review of the autoencoder and its variants: A comparative perspective from target recognition in synthetic-aperture radar images”. In: *IEEE Geoscience and Remote Sensing Magazine* 6.3 (2018), pp. 44–68.

[51] Ashesh Chattopadhyay, Ebrahim Nabizadeh, and Pedram Hassanzadeh. “Analog forecasting of extreme-causing weather patterns using deep learning”. In: *Journal of Advances in Modeling Earth Systems* 12.2 (2020), e2019MS001958.

[52] Hans Hersbach et al. “The ERA5 global reanalysis”. In: *Quarterly Journal of the Royal Meteorological Society* 146.730 (2020), pp. 1999–2049.

[53] VRT. *België telde negen dagen Dunkelflaute in januari*. https://www.vrt.be/vrtnws/nl/2017/02/24/belgie_telde_negendagendunkelflauteinjanuari-2900900/. Accessed January 26, 2022. 2017.

[54] Marc’Aurelio Ranzato et al. “Unsupervised learning of invariant feature hierarchies with applications to object recognition”. In: *2007 IEEE conference on computer vision and pattern recognition*. IEEE. 2007, pp. 1–8.

[55] Vijay Badrinarayanan, Alex Kendall, and Roberto Cipolla. “Segnet: A deep convolutional encoder-decoder architecture for image segmentation”. In: *IEEE transactions on pattern analysis and machine intelligence* 39.12 (2017), pp. 2481–2495.

[56] Forest Agostinelli et al. “Learning activation functions to improve deep neural networks”. In: *arXiv preprint arXiv:1412.6830* (2014).

[57] Diederik P Kingma and Jimmy Ba. “Adam: A method for stochastic optimization”. In: *arXiv preprint arXiv:1412.6980* (2014).

[58] Stuart Lloyd. “Least squares quantization in PCM”. In: *IEEE transactions on information theory* 28.2 (1982), pp. 129–137.

[59] Bilal Babar, Rune Graversen, and Tobias Boström. “Solar radiation estimation at high latitudes: Assessment of the CMSAF databases, ASR and ERA5”. In: *Solar Energy* 182 (2019), pp. 397–411.

[60] Yesi Sianturi, Marjuki, and Kwarti Sartika. “Evaluation of ERA5 and MERRA2 reanalyses to estimate solar irradiance using ground observations over Indonesia region”. In: *AIP Conference Proceedings*. Vol. 2223. 1. AIP Publishing LLC. 2020, p. 020002.

[61] Martın Abadi et al. “Tensorflow: A system for large-scale machine learning”. In: *12th {USENIX} symposium on operating systems design and implementation ({OSDI} 16)*. 2016, pp. 265–283.

[62] Antonio Gulli and Sujit Pal. *Deep learning with Keras*. Packt Publishing Ltd, 2017.

[63] Anil K Jain, M Narasimha Murty, and Patrick J Flynn. “Data clustering: a review”. In: *ACM computing surveys (CSUR)* 31.3 (1999), pp. 264–323.

[64] F. Pedregosa et al. “Scikit-learn: Machine Learning in Python”. In: *Journal of Machine Learning Research* 12 (2011), pp. 2825–2830.

[65] David L Davies and Donald W Bouldin. "A cluster separation measure". In: *IEEE transactions on pattern analysis and machine intelligence* 2 (1979), pp. 224–227.

[66] Teuvo Kohonen. "The self-organizing map". In: *Proceedings of the IEEE* 78.9 (1990), pp. 1464–1480.

[67] Teuvo Kohonen. "Essentials of the self-organizing map". In: *Neural networks* 37 (2013), pp. 52–65.

[68] Jennifer Francis and Natasa Skific. "Evidence linking rapid Arctic warming to mid-latitude weather patterns". In: *Philosophical Transactions of the Royal Society A: Mathematical, Physical and Engineering Sciences* 373.2045 (2015), p. 20140170.

[69] Masamichi Ohba, Shinji Kadokura, and Daisuke Nohara. "Impacts of synoptic circulation patterns on wind power ramp events in East Japan". In: *Renewable Energy* 96 (2016), pp. 591–602.

[70] Peter B Gibson et al. "On the use of self-organizing maps for studying climate extremes". In: *Journal of Geophysical Research: Atmospheres* 122.7 (2017), pp. 3891–3903.

[71] Paul C Loikith, Benjamin R Lintner, and Alex Sweeney. "Characterizing large-scale meteorological patterns and associated temperature and precipitation extremes over the northwestern United States using self-organizing maps". In: *Journal of Climate* 30.8 (2017), pp. 2829–2847.

[72] Bedassa R Cheneka, Simon J Watson, and Sukanta Basu. "Associating Synoptic-Scale Weather Patterns with Aggregated Offshore Wind Power Production and Ramps". In: *Energies* 14.13 (2021), p. 3903.

[73] Giuseppe Vettigli. *MiniSom: minimalistic and NumPy-based implementation of the Self Organizing Map.* 2018. URL: `https://github.com/JustGlowing/minisom/`.

5

Mesoscale modeling of a 'Dunkelflaute' event

In the near future, wind and solar generation are projected to play an increasingly important role in Europe's energy sector. With such fast-growing renewable energy development, the presence of simultaneous calm wind and overcast conditions could cause significant shortfalls in production with potentially serious consequences for system operators. Such events are sometimes dubbed 'Dunkelflaute' events and have occurred several times in recent history. The capabilities of contemporary mesoscale models to reliably simulate and/or forecast a Dunkelflaute event are not known in the literature. In this paper, a Dunkelflaute event near the coast of Belgium is simulated utilizing the Weather Research and Forecasting (WRF) model. Comprehensive validation using measured power production data and diverse sets of meteorological data (e.g., floating lidars, radiosondes, weather stations) indicates the potential of WRF to reproduce and forecast the boundary layer evolution during the event. Extensive sensitivity experiments with respect to grid-size, wind farm parameterization, and forcing datasets provide further insights on the reliability of the WRF model in capturing the Dunkelflaute event.

This chapter is partly based on *Li, B., Basu, S., Watson, S. J., and Russchenberg, H. W. (2021). Mesoscale modeling of a "Dunkelflaute" event. Wind Energy, 24(1), 5-23.* [1].

Under various energy transition scenarios, a rapid growth in renewable energy generation can be foreseen, leading to a more sustainable energy system in Europe. In order to fulfill the target of 40% greenhouse gas emission reduction by 2030 (compared to the emission level of 1990), it is projected that a significant share (≈ 32%) of the total energy consumption in Europe will be from renewable sources by 2030[2]. This share could be as high as ≈ 66% by 2050[3]. In order to meet these ambitious targets, the North Sea region will play an increasingly important role. By the year 2045, an offshore wind energy installation of around 180 GW in the region is expected [4]. Belgium's massive investment in the renewable energy sector, including offshore wind farms over the North Sea, indicates that a complete shut-down of nuclear power plants by 2025 is attainable [5]. As far as the Netherlands is concerned, the roll-out of offshore wind farms is anticipated to expand at a rate of 1 GW per year up until 2030[6]. By 2050, an aggregated 75 GW installation of offshore wind farms is planned.

Unlike fossil fuel-based energy sources, some of the renewable energy sources (especially, wind and solar) strongly rely on meteorological conditions. As such sources of energy play a larger role in electricity networks, this presents an increasing challenge in terms of balancing supply and demand. Therefore, it is important to increase our understanding and forecasting capability of certain weather phenomena which can result in adverse renewable energy production from a system operator perspective. Such advanced knowledge and tools will further support the continuing growth of renewables in the foreseeable future.

In this paper, we focus on one such weather phenomenon called 'Dunkelflaute' as it is rapidly becoming a major concern for the renewable energy community [7]. The word Dunkelflaute was coined by combining two German words 'Dunkelheit' (darkness) and 'Windflaute' (little wind) to describe heavy overcast skies and weak wind conditions. These meteorological events can last from a few hours to a few consecutive days. It is needless to say that under the influence of such a meteorological condition, little or no wind and solar energy can be produced.

On the 30th April 2018, an unexpected Dunkelflaute event occurred over the southern part of the North Sea and caused a large imbalance in renewable power generation and overall consumption. Given the acuteness of the situation, TenneT – the main transmission system operator for Germany and the Netherlands – had to issue an emergency alert in the Netherlands [8, 9]. The crisis could not be avoided by simple load management or by making use of reserve power; instead, a substantial amount of electricity had to be imported from neighboring countries at high market price.

This Dunkelflaute event was not an isolated episode. As a matter of fact, over the past few years, several Dunkelflaute events occurred in Belgium[10, 11, 12, 13], Germany[7, 14, 15, 16], and other neighboring countries. Some of them caused significant impacts on the power grids and electricity markets. There is no reason to believe that the occurrences of Dunkelflaute will subside in the future. Instead, with the ever increasing penetration of renewables in the power grid, the (negative) impacts of Dunkelflaute events will likely become more and more detrimental.

As a first step towards better forecasting of Dunkelflaute events, in this study, we investigate a recent Dunkelflaute event which occurred in Belgium. We analyze a diverse suite of observational datasets for detailed characterization. We evaluate the performance of a state-of-the-art mesoscale model, called the Weather Research and Forecasting (WRF)

model[17, 18], in capturing this event. The organization of this paper is as follows. In Section 2, we briefly provide the meteorological background of the Dunkelflaute phenomenon. The selected case study is discussed in Section 3. The observational datasets and our atmospheric modeling framework are described in Sections 4 and 5, respectively. The simulated results along with in-depth analysis are documented in Section 6. At the end, we summarize our findings and elaborate on potential future research in this arena. A brief climatology of Dunkelflaute events in Belgium is documented in Appendix A.

5.1 Dunkelflaute: A Meteorological Perspective

The word Dunkelflaute does not exist in the vocabulary of meteorologists. Instead, they commonly refer to this phenomenon as the "anticyclonic gloom" [19, 20]. There are also localized names to describe this dull and drab weather phenomenon. For example, in the dialect of Lincolnshire, UK, it is known as *moäky* or *moke*[21].

One of the earliest references to anticyclonic gloom can be found in a sublime article by Captain C. K. M. Douglas[22]. Exactly one hundred years ago, he conducted a comprehensive study on cloud characterization using aerial photography and stated:

> "It is not generally realised that when the sky is covered with a gloomy canopy of cloud, with the inevitable smoky haze over towns and for a considerable distance to leeward, one has only to ascend about a mile in order to enter a region with clear blue sky above, and a sea of white billowy cloud underneath, which stretches in all directions to a distant horizon which stands out sharply owing to the perfect visibility.
> ...
> In winter the sky is very frequently overcast with a single sheet of low cloud varying in thickness from 500 to 2000 feet. This type of cloud is very characteristic of anticyclonic weather. There may be several days or a week of overcast sky, a state of affairs described by Mr. W. H. Dines as anticyclonic gloom."

Over the years, our overall understanding of anticyclonic gloom has been steadily increasing. We now know that it is characterized by a high pressure system, extensive stratus and/or stratocumulus cloud cover, strong subsidence inversion, near-calm wind, low surface temperature, and possibly foggy nights[23, 24]. We are also aware of the fact that anticyclonic gloom is predominantly a winter-time phenomenon. Although, it can happen during the summer months under appropriate synoptic meteorological conditions and sea state, e.g. Galvin[25].

In spite of basic characterizations, more detailed knowledge (e.g., radiation and heat budgets, dynamical evolution and dissipation) pertaining to anticyclonic gloom is severely lacking in the atmospheric science literature. For example, after the (inconclusive) studies by Priestley and Swinbank[26] and Robinson[27] around 1950, we have not come across any follow-up publication on heat budgets of anticyclonic gloom. In the era of advanced instrumentation (including remote-sensing) and cutting-edge numerical modeling (e.g., large-eddy simulation), such a critical knowledge-gap should not exist.

In this context, it is important to note that there have been several comprehensive modeling studies[28, 29, 30] probing both stratus- and stratocumulus-topped boundary layers. However, to the best of our knowledge, none of these studies focused on the weak

wind (or calm) regime – a necessary ingredient for the genesis of anticyclonic gloom. It is the sole purpose of the present study to investigate this specific regime using the WRF model.

5.2 Description of Case Study

In January 2017, Belgium experienced a total of nine days of Dunkelflaute (anticyclonic gloom) [10, 11, 12, 13]. During these days, due to gentle breeze and overcast conditions, the energy production from wind and solar farms were far below their rated values. To further aggravate the situation, a nuclear power plant malfunctioned at the same time. Several measures, including more electricity generation from natural gas, additional power imports from neighbouring countries, and other flexibility options were undertaken to handle this acute problem[31]. Modeling by Elia of a similar extended period of low renewable energy generation (wind and PV) under a future 2040 scenario indicated that there could be an overall shortage of more than 1000 GWh of energy [11] which would be difficult to fill with existing storage technology.

The aggregated wind (onshore and offshore) and solar power production data for Belgium are publicly available from Elia (`http.elia.be`) – the transmission system operator in Belgium. The production data for the month of January 2017 are shown Fig. 5.1. In lieu of any objective (quantitative) criterion in the literature, here, we define a period as Dunkelflaute when onshore wind, offshore wind, and solar power generation all fall below 10% of their respective nominal capacities. These periods are marked as lightly shaded grey regions in Fig. 5.1. The weak wind conditions, occurring during nighttime hours (no solar power generation), are demarcated by a darker shade. In this paper, we focus on two of these Dunkelflaute periods: January 15–17 and January 22–25.

The surface analyses for January 15th and January 25th are shown on the top panel of Fig. 5.2. It is clear that the Azores high was present in the eastern Atlantic on January 15th. At the same time, over the North Sea region, the gradients of surface pressure were relatively strong and were conducive to adequate wind power generation (see top-panel of Fig. 5.1). In the following days, a stronger anticyclone (high pressure center) developed over continental Europe and moved slowly eastward. At its peak, it reached an impressive magnitude of 1042 hPa (not shown). On and around January 25th, the anticyclone was located over Germany. Given the vast expanse of the high pressure regions (refer to top-right panel of Fig. 5.2), the pressure gradients were rather slack and led to extremely calm wind conditions. It is needless to say that neither the onshore nor the offshore wind farms in Belgium produced any energy on that day.

During both Dunkelflaute events of January 15th–17th and January 22th–25th, the southern part of the North Sea was overcast with thick clouds (bottom panels of Fig. 5.2), resulting in very little solar radiation reaching the surface. As shown in the bottom panel of Fig. 5.1, the solar energy production was virtually negligible during these Dunkelflaute periods.

Even though it is completely out of the scope of the present study, we would like to point out that the atmospheric circulation patterns over continental Europe were very unusual during January 2017 (refer to Appendix B). They caused extreme cold and violent storms at various places resulting in numerous deaths[32]. From that perspective, these Dunkelflaute events were far less sinister in nature.

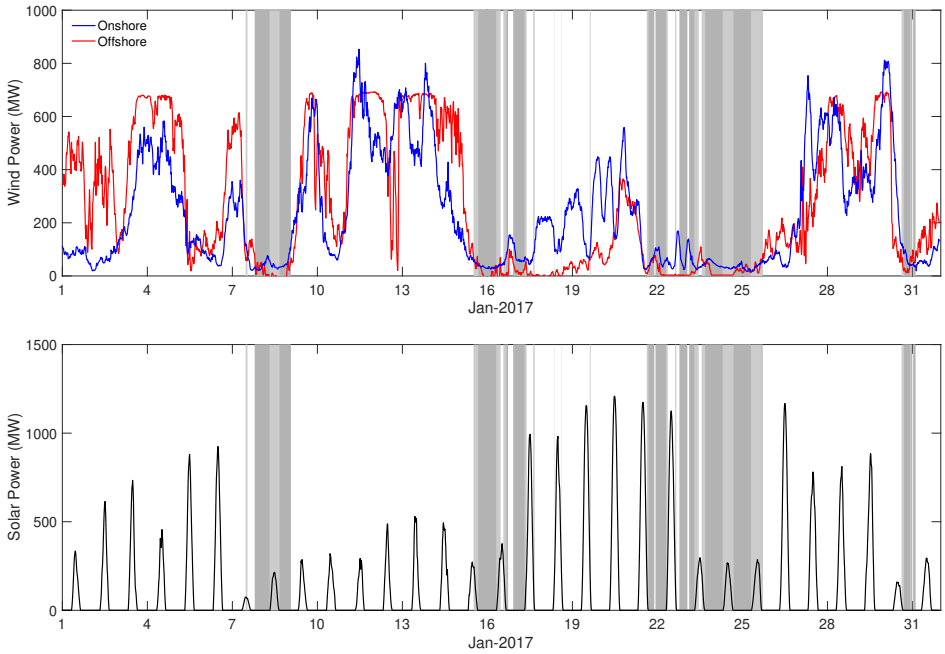

Figure 5.1: Time series of wind energy (top panel) and solar energy (bottom panel) production during January 2017 (data source: Elia.be). The daytime Dunkelflaute periods are represented with lightly shaded grey regions. The weak wind conditions, occurring during nighttime hours (no solar power generation), are demarcated by a darker shade. If two grey regions are separated by no more than one hour, they have been merged together.

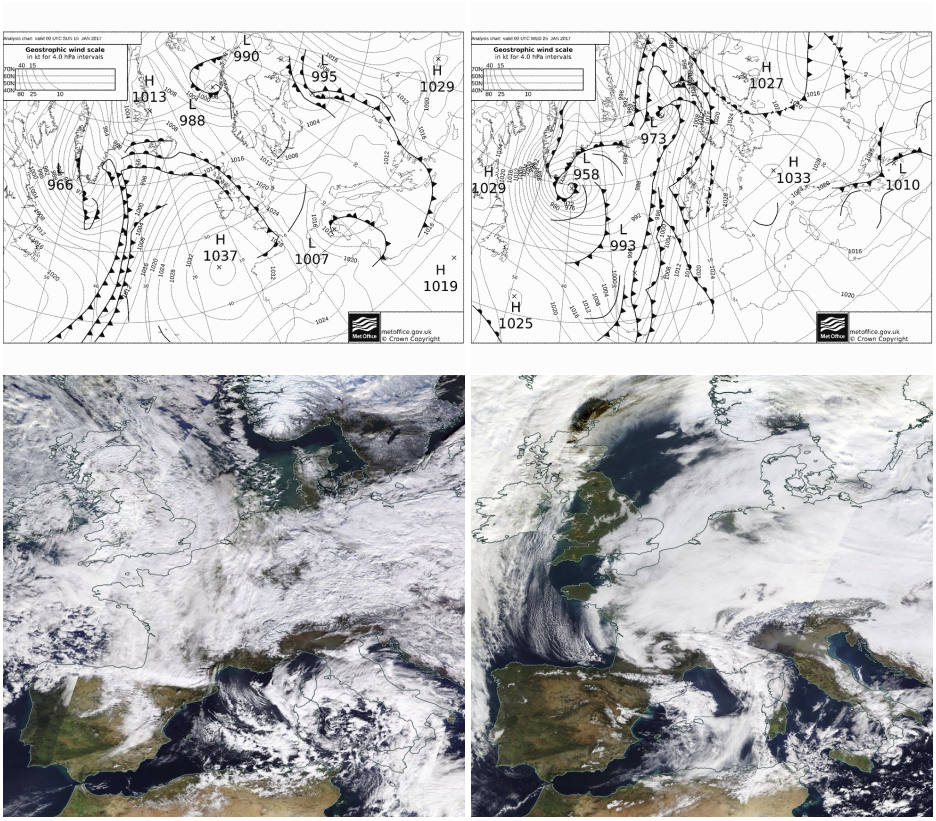

Figure 5.2: Synoptic weather maps for January 15th (top-left panel) and January 25th (top-right panel) of 2017. Source: `http://www.wetterzentrale.de/`. MODIS satellite-based reflectance maps for January 15 (bottom-left panel) and January 25th (bottom-right panel) of 2017. Source: `https://worldview.earthdata.nasa.gov`.

5.3 Description of Observational Datasets

During January 2017, Belgium had only three operational offshore wind farms, C-Power, Northwind, and Belwind I, with a combined capacity of 712 MW. These wind farms and their associated wakes can be seen in the left panel of Fig. 5.3. In this paper, we have used aggregated power production data from these wind farms in conjunction with solar farms to characterize the Dunkelflaute phenomenon. The temporal granularity of these datasets is 15 minutes. Note that these data have been post-processed by Elia to account for missing data or other data anomalies[33, 34].

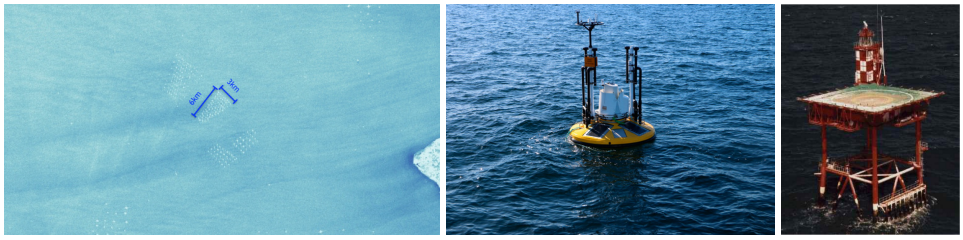

Figure 5.3: Left panel: synthetic aperture radar (SAR) image of Belgian offshore wind farms (source: Google Earth Engine); middle panel: image of the SEAWATCH wind lidar buoy located at Borssele Wind Farm Zone (BWFZ, source: BWFZ Project and Site Description); right panel: image of Lichteiland Goeree (LEG, source: DNV-GL[35]).

In addition to the power production data, we use meteorological data from several offshore and onshore locations. First of all, we make use of several lidar-based wind datasets which are publicly available via TNO (fomerly ECN, the Energy Research Center of the Netherlands). Floating lidars (middle panel of Fig. 5.3), as well as lidars on fixed platforms (right panel of Fig. 5.3) were utilized to collect wind data. At Borssele Wind Farm Zone (BWFZ) and Hollandse Kust Zuid (HKZ), SEAWATCH floating lidar systems (equipped with ZX, formerly ZephIR, 300S lidars) were deployed by Fugro. These lidars provided wind profiling data for 10 heights between 30 m and 200 m above mean sea level (MSL). The temporal resolution of all the wind time-series is 10 min.

The wind dataset from BWFZ has only a handful of missing samples. These measurements were validated against a cup-anemometer at Vlakte van de Raan wind station and were found to be of high quality[36, 37]. In the HKZ region, two floating lidars were taking wind measurements at locations called HKZA and HKZB. Unfortunately, due to intermittent transmission failures, the wind dataset from HKZA has several gaps. The lidar at HKZB did not suffer from a similar data-loss problem. In fact, the wind data at HKZB were strongly correlated with conventional anemometer-based data from Lichteiland Goeree (LEG) and EuroPlatform (EPL) stations attesting to its high quality[38, 39]. At LEG and EPL platforms, ZX wind lidars were also deployed and measured at several heights (from 90 m to 315 m) every 10 minutes[40, 41]. The locations of BWFZ, HKZ, LEG, EPL, and the offshore wind farms can be seen in the left panel of Fig. 5.4.

Next, measurements from the Stabroek automated weather station (AWS) are utilized in this study. This AWS is operated by the Royal Meteorological Institute (RMI) of Belgium and its location can be seen in the left panel of Fig. 5.4. The recorded shortwave radiation data have a temporal resolution of 10 minutes[42].

Lastly, sounding datasets from three land-based stations (Herstmonceux, Norderney, and EDZE Essen, locations shown in the right panel of Fig. 5.4), are utilized for the characterization of the vertical structure of the atmosphere during the Dunkelflaute periods. These datasets are provided by the University of Wyoming[43] and contain vertical profiles of wind speed, potential temperature, and several other meteorological variables.

5.4 Model Setup

The Weather Research and Forecasting (WRF) model (version 3.9.1.1), is employed here to simulate the atmospheric conditions associated with the aforementioned Dunkelflaute event. A total of six different simulations are performed by varying large-scale forcing data and physical parameterizations; see Table 5.1 for details. The first five simulations start at 00 UTC on January 14th, 2017, and last for a total of 14 days. The last simulation (called WRF–GFS+) is initialized at 00 UTC of January 21st. Model output are saved every 10 minutes.

All the simulations utilize 51 vertical levels with nonuniform grid spacing with the top of the model reaching approximately 16 km from the surface. The lowest grid level is approximately at 8 m from the surface and there are 18 levels in the lowest 1 km of the model atmosphere. In every simulation (with one exception), grid nudging is applied above approximately 2 km in order to keep the simulations in sync with the large-scale forcing data. In addition, the sea-surface temperature field is continuously updated throughout the simulations.

Numerous physical parameterization options are available in the WRF model to represent turbulence, land-atmosphere interactions, radiation, cloud microphysics and other processes. Based on our past experience, we have used the following parameterizations: NOAH land surface model[44], Rapid Radiative Transfer Model for Global Climate Models (RRTMG) for longwave radiation and shortwave radiation[45], WRF Single-Moment 5-class microphysics scheme[46], and Kain-Fritsch cumulus scheme[47] (only activated for grid sizes coarser than 5 km). We have selected the Mellor-Yamada-Nakanishi-Niino (MYNN) 2.5 level scheme[48] as the default planetary boundary layer (PBL) parameterization. However, in one of the WRF runs, we use the Yonsei University scheme[49, 50] to investigate the sensitivity of the simulated results with respect to PBL parameterizations.

The wind farm parameterization by Fitch et al.[51] is activated in three of the WRF runs to simulate the effects of the Belgian offshore wind turbines on the atmospheric flow fields. The effects of the wind turbines are represented as drag-induced energy sink and increased turbulence in the vertical levels containing the rotor disk. The Fitch parameterization assumes that a fraction of the total energy flowing through the wind farm is used for power production (based on the turbine power coefficient) and the rest is converted into turbulent kinetic energy (determined by the turbine thrust coefficient). The simulated wind farm area consists of three Belgian offshore wind farms: C-Power, Northwind, and Belwind I. In the left panel of Fig. 5.4, they are depicted as white dots. There are a total of 182 wind turbines of five different types (Table 5.2). The power curves and thrust curves of these turbines are listed in Appendix C.

Three different large-scale forcing datasets are used for initial conditions (IC) and boundary conditions (BC). The ERA5 reanalysis dataset (horizontal grid size: ~31 km; sampling rate: 1 hourly) is available from 1979 to present day from the European Centre

for Medium-Range Weather Forecasts (ECMWF) [52]. The ERA-Interim reanalysis dataset (horizontal grid size: ~79 km; sampling rate: 6 hourly) is also available from ECMWF [53]. In addition to these reanalysis datasets, we also use an operational forecast dataset (horizontal grid size: 0.25°; sampling rate: 3 hourly for 0 to 240 h period and 12 hourly for 240 h to 384 h) from the Global Forecast System (GFS) to investigate if the Dunkelflaute periods could have been predicted in a real-time forecast scenario. The WRF–GFS and WRF–GFS+ simulations are initialized on January 14th and 21st, respectively to investigate the impacts of prediction horizons on Dunkelflaute forecasting.

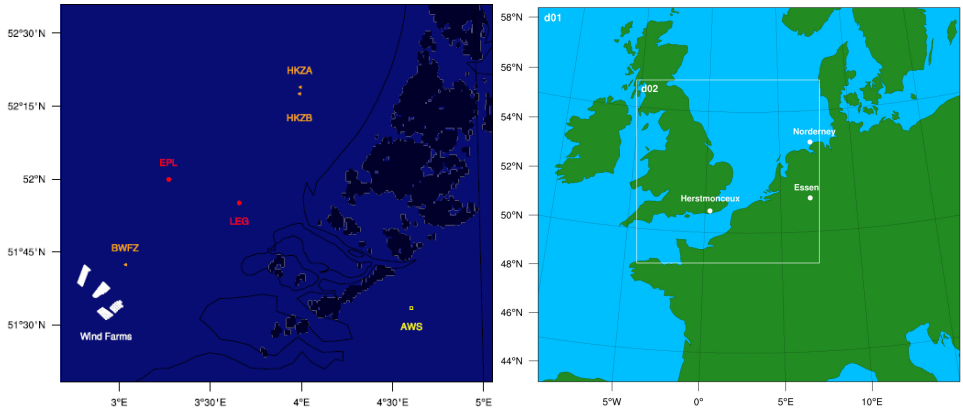

Figure 5.4: Left panel: locations of the Belgian offshore wind farms and the meteorological stations. Right panel: domain configuration for the WRF simulations when the ERA5 reanalysis dataset is used for initial and boundary conditions. The locations of the radiosonde launch locations are overlaid on this plot.

For the WRF runs involving ERA5, two nested domains are used (right panel of Fig. 5.4). These domains are coupled in an one-way nesting mode. The outermost domain (d01) has a grid size of 9 km (domain size: 1890 km × 1674 km); whereas, the inner domain (d02) employs a grid size of 3 km (domain size: 819 km × 819 km). Given the coarser spatial resolution of the ERA-Interim and the GFS datasets, we deemed it necessary to use a three domain configuration. The largest domain (d01) for these runs uses a grid size of 27 km (domain size: 2673 km × 2943 km); it is not shown. The second domain (d02) and the third domain (d03) use grid sizes of 9 km and 3 km, respectively. Their corresponding domain sizes exactly match the ones shown in the right panel of Fig. 5.4.

Table 5.1: Technical Details of the WRF Simulations

WRF Run	IC/BC	Grid Size (km)	Time Step (s)	PBL Scheme	Wind Farm Scheme	Grid Nudging	Initialization Date
WRF–ERA5	ERA5	9/3	45/15	MYNN 2.5 level	on	on	Jan 14th, 2017
WRF–ERA5*	ERA5	9/3	45/15	MYNN 2.5 level	off	on	Jan 14th, 2017
WRF–ERA5#	ERA5	9/3	45/15	YSU	off	off	Jan 14th, 2017
WRF–ERA-I	ERA-Interim	27/9/3	90/45/15	MYNN 2.5 level	on	on	Jan 14th, 2017
WRF–GFS	GFS operational	27/9/3	90/45/15	MYNN 2.5 level	on	on	Jan 14th, 2017
WRF–GFS+	GFS operational	27/9/3	90/45/15	MYNN 2.5 level	on	on	Jan 21st, 2017

Table 5.2: Information on the three Belgian offshore wind farms used in this study

Wind Farm	Nameplate Capacity (MW)	Turbines	Hub Height (m)	Rotor Diameter (m)
C-Power	325	6 Senvion 5 MW + 48 Senvion 6.2 MW	94	126
Northwind	216	72 Vestas V112 3 MW	71	112
Belwind I	171	55 Vestas V90 3 MW + 1 Alstom 6 MW	72	90

5.5 Results

In this section, we compare the WRF model-based simulated results against various observational data. In addition, we investigate the sensitivities of the simulated results with respect to grid-size, IC/BC, and wind farm parameterization.

5.5.1 Time Series Analysis

Measured wind speed time-series for the period of 14th–28th January of 2017 are shown in the top panel of Fig. 5.5. It is evident that the wind speeds were mostly lower than 5 m s^{-1} during the Dunkelflaute periods. More interestingly, wind speed shears within the layer of 40–180 m were virtually absent for almost the entire two-week period; thus, it can be inferred that the lower part of the boundary layer was well-mixed. Starting January 27th, we do see some signatures of wind speed shear in the measurements.

Measured wind speed time-series from four stations (i.e., LEG, EPL, BWFZ, HKZ) over the North Sea are intercompared in the top-right panel of Fig. 5.5. The selected measurement heights are close to the hub-height of a Senvion 5 MW turbine (94 m). Specifically, at LEG and EPL, the selected measurement heights were at 91 m; whereas, at BWFZ and HKZ, they were at 100 m. As illustrated by Fig. 5.5, the overall consensus of all the wind speed time-series is very high. Since these four stations are spread over a large area (see the left panel of Fig. 5.4), it is safe to deduce that the wind speeds during the chosen time-period were spatially rather homogeneous.

The simulated wind speed time-series from the WRF–ERA5 and WRF-ERA-I runs are shown in the bottom panel of Fig. 5.5. The selected grid points are close to the BWFZ station. Output from both the runs show similar temporal evolution patterns and strongly agree with the measured data in terms of magnitudes of both wind speeds and wind shears. On January 21st, the simulated data exhibited a small level of shear which were not present in the measurements.

As illustrated by Fig. 5.6, the observed and simulated wind direction time-series varied a lot during January 14th–28th. The WRF–ERA5 run has more-or-less captured the overall trend. Some deviations are however noticeable.

In the left panel of Fig. 5.7, the WRF model-generated wind power production data are overlaid on top of the measured data by Elia. It is clear that the wind farm parameterization of the WRF model is able to accurately capture the magnitudes of the power production including the rapid ramp-down and ramp-up events. During the Dunkelflaute periods, the measured power production data had a few sporadic episodes of power generation; the simulated data were unable to capture such traits.

Given the spatio-temporally intermittent cloud patterns (see the bottom panel of Fig. 5.2), rigorous validation of the WRF model-generated radiation data is a challenging task. As a poor man's choice, we have decided to compare the simulated (downwelling) shortwave radiation data against the observational data from the Stabroek station. From the right panel of Fig. 5.7, it is clear that the WRF model significantly overestimated the magnitudes of shortwave radiation during the Dunkelflaute periods; in other words, the cloudiness was weaker in the model than in the reality.

The measured and simulated air temperature time-series are compared in the left panel of Fig. 5.8. Once again, we have selected the BWFZ location for comparison. The temperature data were measured at a height of 4 m. However, the simulated data are from

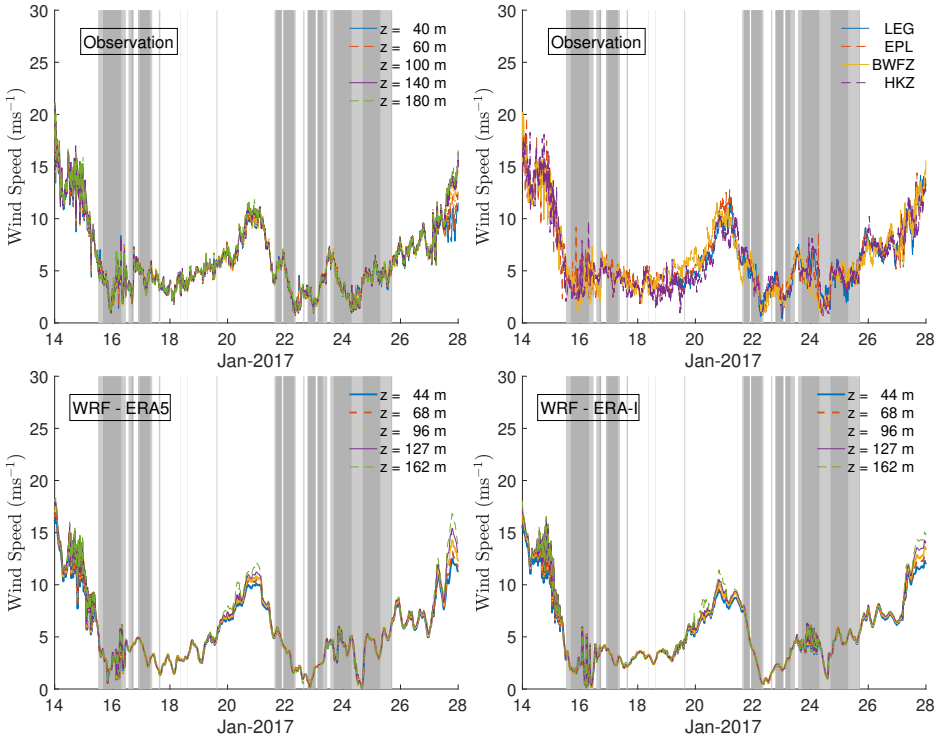

Figure 5.5: Top-left panel: wind speed time series from various heights measured at the BWFZ station. Top-right panel: hub-height (~91–100 m) wind speed time series measured at four locations over the North Sea (i.e., LEG, EPL, BWFZ, HKZ). Simulated wind speed time series from various heights extracted from the WRF-ERA5 and WRF-ERA-I runs are shown in the bottom-left and bottom-right panels, respectively. Only the simulated data from the innermost domains (i.e., grid size of 3 km) are shown. The selected grid points are in close proximity to the BWFZ station. The daytime Dunkelflaute periods are represented with lightly shaded grey regions. The weak wind conditions, occurring during nighttime hours (no solar power generation), are demarcated by a darker shade.

2 m height. In spite of the height difference, the measured and simulated data portray similar trends. As often happens in marine boundary layers, no sign of a diurnal cycle can be found in the temperature data during January 14th–28th. However, during this period, the air temperature dipped below freezing twice, due to the passages of cold fronts. Such temperature drops increased the energy demand, and in turn, the energy deficits during the Dunkelflaute event.

The simulated sea-surface temperature (SST) and surface sensible heat flux values from BWFZ are shown in the left and right panels of Fig. 5.8, respectively. During the two-week simulation period, the SST decreased marginally. Since SST was almost always higher than the air temperature, there is expected to be positive sensible heat flux at the surface. Under such meteorological conditions, the surface layer is considered to be unstable (convective) and it promotes turbulent mixing. Wind shears decrease drastically due to mixing as depicted earlier in Fig. 5.5.

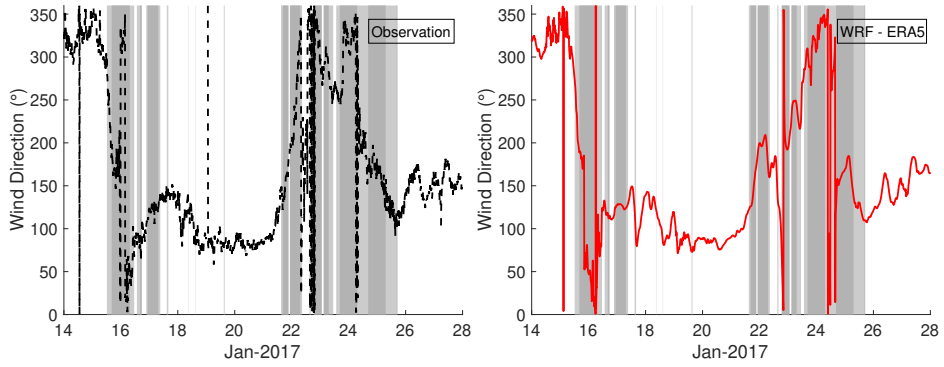

Figure 5.6: Left panel: measured hub-height (100 m) wind direction time series at the BWFZ station. Right panel: simulated wind direction time series (96 m) extracted from the WRF–ERA5 run (d02 domain). The selected grid point from the WRF model is in close proximity of the BWFZ station. The daytime Dunkelflaute periods are represented with lightly shaded grey regions. The weak wind conditions, occurring during nighttime hours (no solar power generation), are demarcated by a darker shade.

During January 27th–28th, due to warm air advection, the air temperature became warmer than the sea-surface and created stably stratified conditions. Such atmospheric conditions are conducive to high wind shears as can be seen in Fig. 5.5.

5.5.2 Boundary Layer Structure

Measured profiles of potential temperature and wind speed spanning the entire boundary layer are not available over the southern part of the North Sea region. As a substitute, we utilize radiosondes launched from three neighboring locations over land (Herstmonceux, Norderney, and EDZE Essen; see right panel of Fig. 5.4) to characterize the boundary layer structure. In Figs. 5.9–5.11, we compare measured and simulated profiles for January 15th and 24th. For both days, we show profiles corresponding to 00 UTC (close to local midnight) and 12 UTC (close to local noon time). Simulated data from three runs (WRF–ERA5, WRF–ERA5#, and WRF–ERA-I) are considered. In addition, we also plot the vertical profiles which are directly extracted from the ERA5 reanalysis data.

Overall, all the simulations and ERA5 data more-or-less capture the magnitudes and shapes of the profiles. Among them, the ERA5 is a clear winner and the WRF–ERA-I performs the worst. The performances of the WRF–ERA5 and WRF-ERA5# runs are slightly poorer than ERA5. This reduction in performance is possible because the WRF runs only utilize ERA5 data during initialization and as boundary conditions. All the internal grid points of the WRF domains dynamically evolve without any data assimilation. The effects of grid nudging is felt only above 2 km.

Since the radiosondes were launched over land, the potential temperature profiles often portray the telltale signs of the circadian cycles. For example, nocturnal stably stratified conditions are noticeable at: Herstmonceux (00 UTC of January 15th and 24th), Norderney (00 UTC of January 24th), and EDZE Essen (00 UTC of January 15th and 24th). The daytime unstable conditions (mixed profiles) are evident at: Herstmonceux (12 UTC of January 24th), Norderney (12 UTC of January 15th and 24th), and EDZE Essen (12 UTC of January

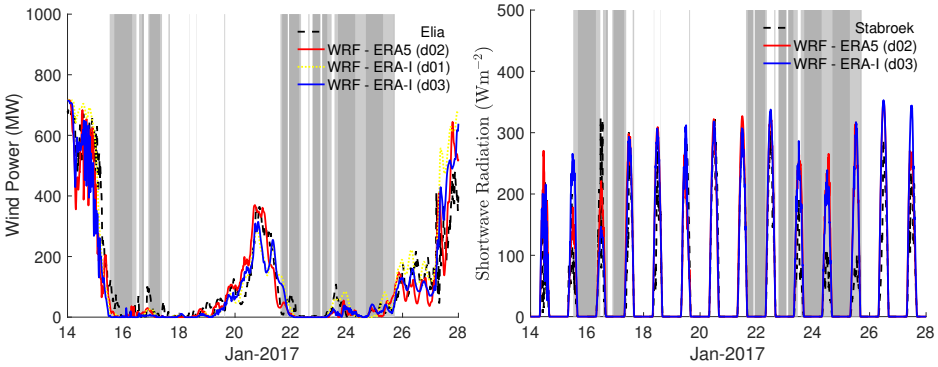

Figure 5.7: Left panel: measured and simulated wind power production data. The measured data are obtained from Elia. Right panel: comparison of measured and simulated (downwelling) shortwave radiation data. The automated weather station is located at Stabroek, Belgium. Only the simulated data from the innermost domains (i.e., grid-size of 3 km) of the WRF–ERA5 and WRF–ERA-I runs are shown in these plots. The daytime Dunkelflaute periods are represented with lightly shaded grey regions. The weak wind conditions, occurring during nighttime hours (no solar power generation), are demarcated by a darker shade.

24th). The other potential temperature profiles do not follow a canonical diurnal pattern. For example, at 12 UTC of January 15th, a deep stable layer persists over Herstmonceux and EDZE Essen.

The WRF simulations have, most of the time, captured the shape and amplitudes of the potential temperature profiles. However, they failed to capture the mixed layer evolution on January 24th at Herstmonceux and EDZE Essen. They underestimated the residual layer height at 00 UTC. The growth of the mixed layer is rather slow for all the simulations. In comparison to the MYNN scheme, the YSU scheme significantly delays the formation of the mixed layer. It is plausible that the entrainment rate is better simulated by the MYNN scheme for this specific case.

The observed wind speeds at higher altitudes were quite strong on January 15th and the simulated ones closely resembled them. However, the WRF results overestimated the turbine-layer wind speeds at Herstmonceux. On January 24th, the wind speeds subsided drastically. At all the locations, the observed and simulated wind speeds were approximately 5 m s^{-1} or even weaker in the lowest 1 km of the boundary layer.

In lieu of observed boundary layer profiles near the Belgian offshore wind farm region, we only document simulated time-height plots of wind speeds and potential temperatures in Fig. 5.12. The estimated PBL heights are overlaid on these plots. From the temperature plot, it is clear that the PBL height was rather shallow (less than 500 m) for the large part of the two-week simulation period. Furthermore, the temperature profiles are found to be uniform in height (i.e., well-mixed) within the boundary layer for most of the time. This result further corroborates our previous finding that the marine boundary layer near the BWFZ station was unstable during January 14th–27th of 2017.

The top-left panel of Fig. 5.12 suggests that a sudden reduction of the wind speed happens on January 15th and persists until January 21st. The gentle breezy condition returned again on January 22nd and lasted until January 27th. The depth of the weak flow field extends much higher than the PBL height. Thus, it is caused by a synoptic scale

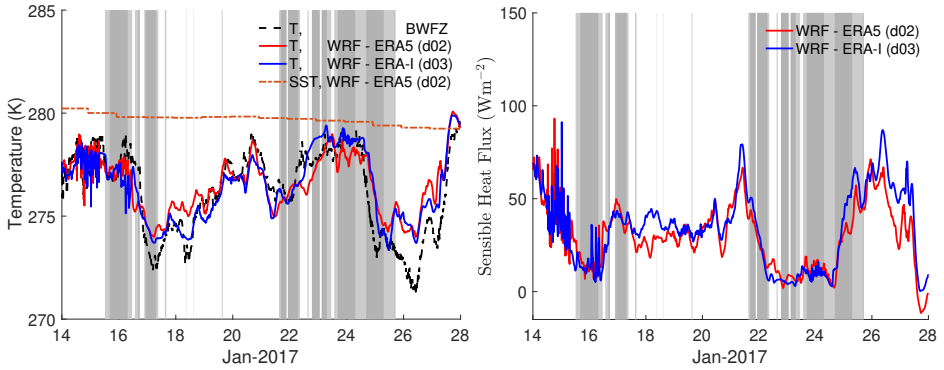

Figure 5.8: Left panel: measured and simulated air temperature time series at the BWFZ station. The measurement height was 4 m; whereas, the simulated data are from 2 m height. The simulated sea-surface temperature (SST) is also overlaid for comparison. Right panel: temporal evolution of sensible heat flux at the surface from the WRF simulations. Only the simulated data from the innermost domains (i.e., grid-size of 3 km) of the WRF–ERA5 and WRF–ERA-I runs are shown in these plots. The daytime Dunkelflaute periods are represented with lightly shaded grey regions. The weak wind conditions, occurring during nighttime hours (no solar power generation), are demarcated by a darker shade.

system (an anticyclone) and not modulated by boundary layer processes. The localized increase of wind speeds on January 21st could be due to an offshore low-level jet; it is a mere speculation and cannot be substantiated in this study.

In order to quantify the impact of the PBL schemes on the simulated results, we have computed the differences of simulated results from the WRF–ERA5# run (invokes the YSU PBL scheme) and the WRF–ERA5 run (utilizes the MYNN 2.5 level PBL scheme). The time-height plots of the differences of wind speeds and potential temperatures are shown in the bottom panel of Fig. 5.12. In terms of potential temperature, the differences are not large. Most of the differences occur in the (subsidence) inversion zone overlying the boundary layer. The wind speed values also differ significantly within this zone. Within the PBL, the YSU scheme often produces slightly stronger wind speeds in comparison to the MYNN scheme.

5.5.3 Sensitivity to Grid-Size and IC/BC

The observed and simulated hub-height (~ 100 m) wind speeds from the BWFZ location are shown in the top panel of Fig. 5.13. The simulated time series from WRF-ERA5 and WRF-ERA-I are quite similar. More interestingly, for both the runs, the simulated results are virtually insensitive to grid-sizes. The ERA5 reanalysis data match the observed data remarkably well, as found earlier in the context of vertical profiles.

In the context of (downwelling) shortwave radiation, the differences between different simulations are significant (see the middle and bottom panel of Fig. 5.13). All the WRF-based results overestimate the magnitude of radiation during the Dunkelflaute periods. For other times, the simulated results are not too far off from from the observations.

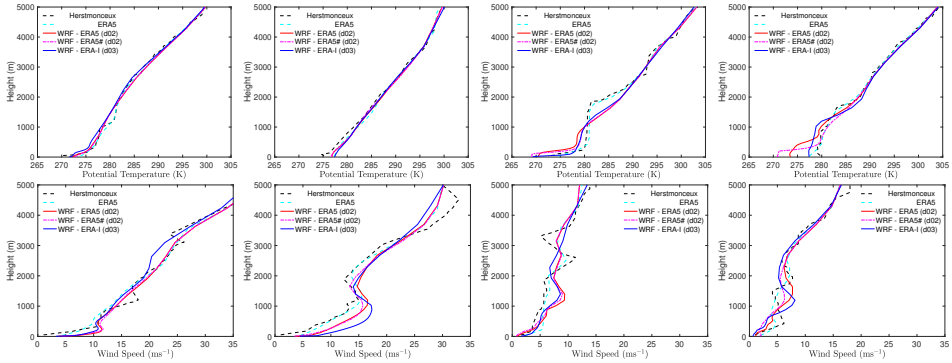

Figure 5.9: Observed and simulated potential temperature (top panel) and wind speed (bottom panel) profiles at the Herstmonceux radiosonde launch location. From left to right, the plots correspond to the following times, respectively: 00 UTC of January 15th, 12 UTC of January 15th, 00 UTC of January 24th, and 12 UTC of January 24th. For the WRF runs (i.e., WRF–ERA5, WRF–ERA5#, WRA–ERA-I), only the simulated results from the 3 km domains are shown and compared. Extracted data from the ERA5 reanalysis data are also included as a baseline.

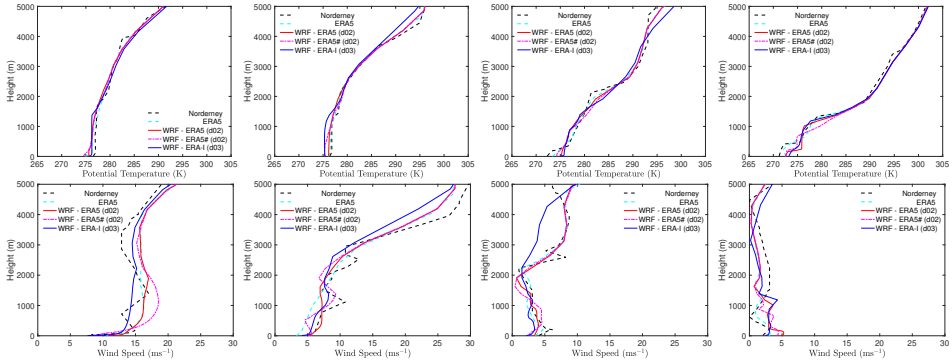

Figure 5.10: Same as Fig. 5.9, except for the Norderney radiosonde launch station.

5.5.4 Sensitivity to Wind Farm Parameterization

The numerical configuration and the physical parameterization options of the WRF–ERA5* run is identical to the default run WRF–ERA5. Except, in the WRF–ERA5* run, the wind farm parameterization scheme is turned off. Whereas, in the WRF–ERA5 run, it is used in conjunction with 182 wind turbines. The differences in the simulated wind speeds and turbulent kinetic energy at the BWFZ station are shown in Fig. 5.14.

The BWFZ station is located about 10 km from the Belgian offshore wind farms (refer to the left panel of Fig. 5.4). It can experience wind farm wake effects when the prevailing wind direction is within 180–270 degrees. According to Fig. 5.6, such wind directions happened a few times during Jan 14th–28th. During such periods (e.g., January 16th and 24th), the wake effects can be clearly seen in Fig. 5.14. These differences are quite substantial in terms of both mean wind speeds and turbulent kinetic energy. For other periods, there are small differences as well. This is due to the fact that in mesoscale simulations any perturbations (here imposed by the wind farm parameterization) in flow fields change future evolution

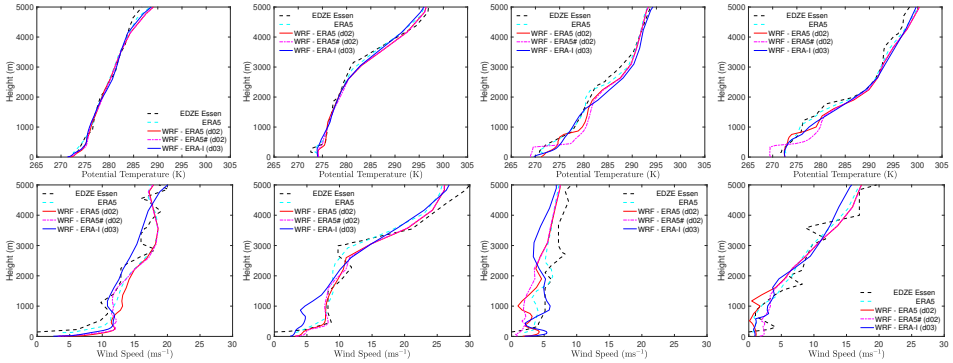

Figure 5.11: Same as Fig. 5.9, except for the EDZE Essen radiosonde launch station.

(the so-called 'butterfly effect').

5

5.5.5 Reanalysis versus Real-time

In addition to initial fields, the WRF model (or any other mesoscale model) requires boundary conditions spanning the entire simulation period. For retrospective simulations, such boundary conditions can be extracted from the reanalysis datasets (e.g., ERA5 and ERA-Interim). Due to extensive data assimilation, such boundary conditions tend to be very accurate. However, in the context of real-time forecasting, such high-fidelity boundary conditions are not available. Rather, one has to use operational forecast data from a global model (e.g., GFS).

In this section, we compare the results from the WRF–GFS run against the default WRF–ERA5 run. We expect the accuracy of the WRF–GFS to be comparable with WRF–ERA5 run at the beginning of the simulation period; however, its performance will likely deteriorate with increasing prediction horizon. The top-left panel of Fig. 5.15 is in line with our expectation. During the period of January 14th-18th, in terms of wind power production, the performance of the WRF–GFS run is at par with WRF–ERA5. Afterwards, its results deviate significantly from the measured data from Elia. Even though the WRF–GFS run predicts the commencement of the second Dunkelflaute period rather accurately, it underestimates its duration. It predicts that the power output from the Belgian wind farms return to the nameplate capacity level by Jan 25th; in reality, such recovery happened after January 28th. In contrast, the WRF–GFS+ run, initialized on January 21st, significantly improves the quality of the wind power forecast for the second Dunkelflaute period (particularly during January 21–26) due to the reduction in prediction horizon (refer to bottom-left panel of Fig. 5.15). In terms of (downwelling) shortwave radiation, the performance of the WRF–ERA5, WRF–GFS, and WRF–GFS+ runs are poor (right panel of Fig. 5.15). More validation work, potentially involving satellite remote-sensing-based radiation data, is needed in this arena.

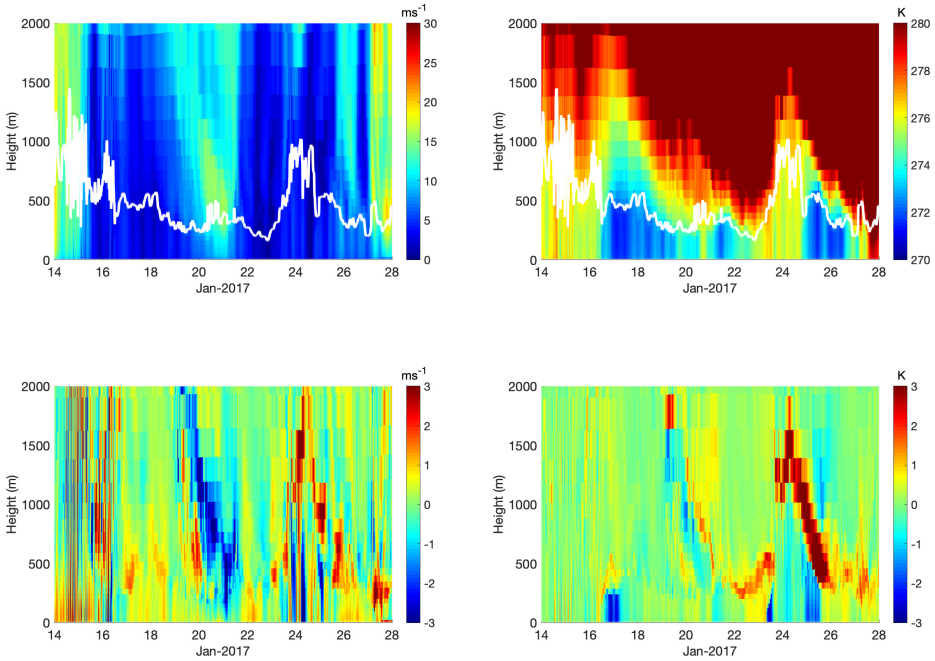

Figure 5.12: Time-height plots of simulated wind speeds (top-left panel) and potential temperature (top-right panel) from the d02 domain (grid size of 3 km) of the WRF–ERA5 run. The simulated PBL heights are overlaid on these plots as white lines. Time-height plots of the differences between the WRF–ERA5# and WRF–ERA5 runs (d02 domains) are shown in the bottom panels. The bottom-left and bottom-right panels represent differences of wind speeds and potential temperatures, respectively. The grid point closest to the BWFZ station is selected for all these plots.

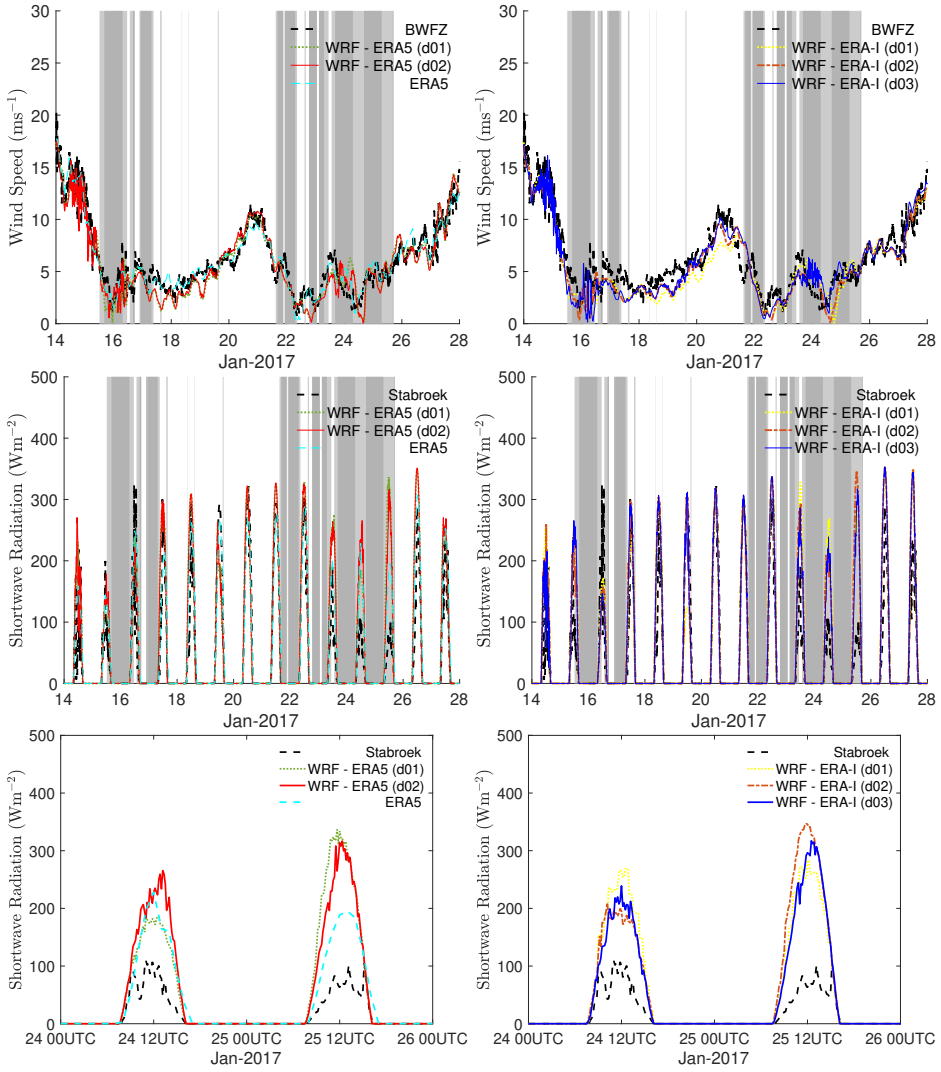

Figure 5.13: Measured and simulated wind speed time series (top panels) and (downwelling) shortwave radiation (middle panels) for January 14th - 28th. The bottom panels show measured and simulated shortwave radiation time series for a shorter duration of January 24th - 25th for clarity. The observational wind speeds and radiation data are from the BWFZ station and Stabroek station, respectively. Simulated results from all the computational domains of the WRF–ERA5 (left panels) and WRF–ERA-I (right panels) are plotted for comparison. Extracted data from the ERA5 reanalysis data are also included as a baseline. The daytime Dunkelflaute periods are represented with lightly shaded grey regions. The weak wind conditions, occurring during nighttime hours (no solar power generation), are demarcated by a darker shade.

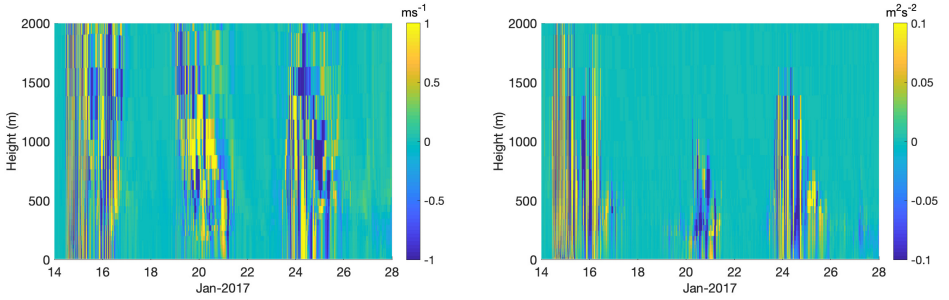

Figure 5.14: Time-height plots of the differences between the WRF–ERA5 and WRF–ERA5* runs (d02 domains). The left and right panels represent differences of wind speeds and turbulent kinetic energy, respectively. The grid point closest to the BWFZ station is selected for all these plots.

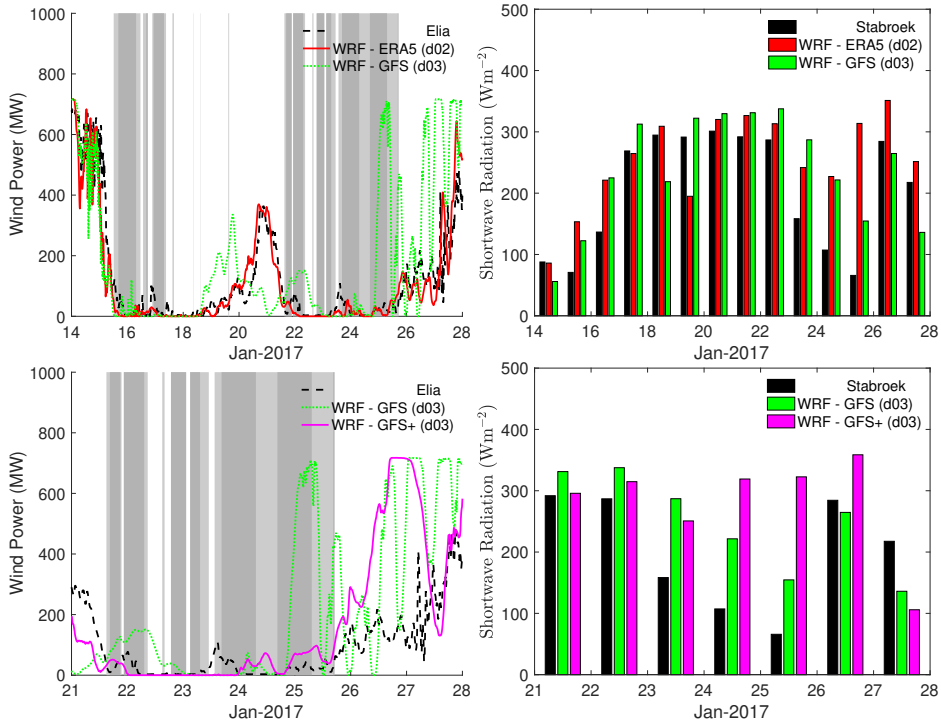

Figure 5.15: Measured and simulated wind power production data (top-left panel) and (downwelling) solar radiation at 12 UTC during January 14th–28th (top-right panel). The simulated results from WRF–GFS+ run, initialized on January 21st, are shown in the bottom panel. The measured wind power data are obtained from Elia. Only the simulated data from the innermost domains (i.e., grid-size of 3 km) of the WRF–ERA5 and WRF–GFS runs are shown in these plots. The daytime Dunkelflaute periods are represented with lightly shaded grey regions. The weak wind conditions, occurring during nighttime hours (no solar power generation), are demarcated by a darker shade.

5.6 Concluding Remarks

In this work, we simulate and characterize a Dunkelflaute (aka anticyclonic gloom) event via mesoscale modeling. An extensive suite of observational data assisted in the model validation. In addition to weak wind and cloudy conditions, we have found that the marine boundary layer was frequently well-mixed during this event. As a consequence, wind speed shears were negligible in measurements over the North Sea and also in corresponding simulated data. Over land, however, the observed and simulated profiles portray traits of stratification and wind speed shears.

For basic climatological characterizations of Dunkelflaute events, the ERA5 reanalysis dataset could be utilized owing to its global coverage, long-term availability, and high accuracy. However, this dataset does not include the wake effects of wind farms. In order to account for such effects, one should utilize the WRF model or other mesoscale models in conjunction with a suitable wind farm parameterization. Mesoscale simulations can also provide more advanced diagnostics (e.g., turbulent kinetic energy), and by virtue of their high spatial resolutions, they can resolve coastal effects.

In this study, we have noticed that in retrospective mode, some of the features (e.g., hub-height wind speeds, power production) of the Dunkelflaute can be reliably simulated using coarse grid-sizes (e.g., 27 km). If this finding holds true for modeling of other Dunkelflaute events, then it will be possible to simulate these events with a relatively low computational costs. In a real-time forecasting scenario, however, this specific event could not be predicted beyond four days. In our future work, we will find out if we can improve on the predictability of these events by coupling mesoscale modeling with deep learning approaches.

Before closing, we would like to mention that the renewable energy community is not the only stakeholder who is interested in a better understanding and forecasting capability of the Dunkelflaute phenomenon. It is also relevant for the air pollution community [54, 55] and the astronomy community [56].

5.7 Appendix

5.7.1 Appendix A: Climatology of Dunkelflaute Events in Belgium

We analyzed wind and solar power production data from `Elia.be` for the years 2013–2018. These data have a sampling rate of 15 min; thus, in a given year, we have approximately 35,000 samples. A particular sample is classified as a Dunkelflaute event if the production by onshore wind, offshore wind, as well as, solar farms fall below 10% of their respective nominal capacities during that particular 15 min period. We do not tag a sample as a Dunkelflaute event if solar power production is exactly zero and it happens outside the time-window of 09 UTC – 15 UTC; this way, we effectively exclude nighttime conditions from the climatological analysis. It is clear from Fig. 5.16 that every year all the three renewable power generation sources drop below 10% of their capacities for a substantial period of time (approximately ranging from 30% to 50%). Typically, offshore wind power production has a higher capacity factor in comparison to its onshore counterpart. On average, the Dunkelflaute events account for around 7% – 8% of the time per year. These numbers do not vary much across the years.

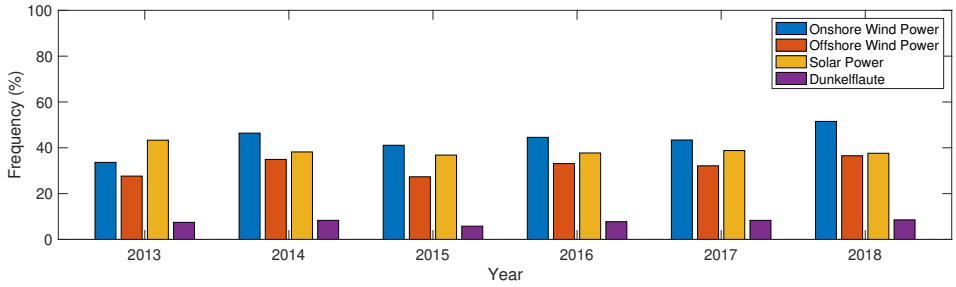

Figure 5.16: Annual climatology of Dunkelflaute events in Belgium. The colored bars represent the percentage of the time when Belgian onshore wind, offshore wind, solar power output and all three simultaneously (classified as Dunkelflaute) are less than 10% of rated output.

5.7.2 Appendix B: Anomaly Patterns over Europe

The synoptic condition during the month of January of 2017 was quite unusual as can be seen in Fig. 5.17; see also Dunstone et al.[57]. These anomaly plots are created using the ERA5 data. First, a climatological mean is computed for the month of January from ERA5 data spanning the years 1981 to 2010. Then, this mean is subtracted from the monthly average of January 2017.

It is evident that during January 2017, over the North Sea, sea level pressure was a lot higher than the climatological mean over the North Sea region. Similar behavior was observed in the case of 500 mb geopotential height. Both zonal and meridional winds showed negative anomaly for the southern part of North Sea and surrounding areas. Extremely cold conditions prevailed over the southern part of continental Europe.

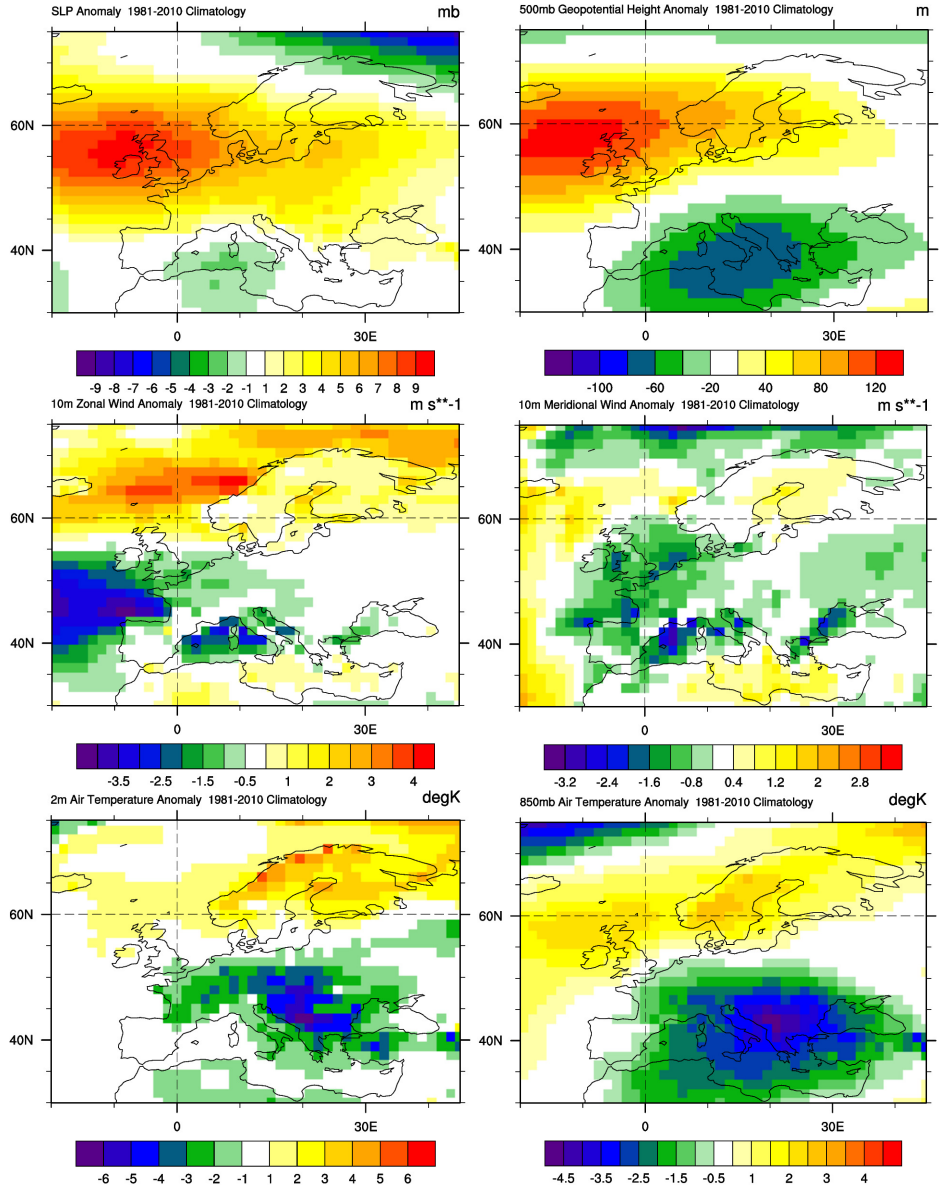

Figure 5.17: Anomaly maps from: `https://www.esrl.noaa.gov/psd/cgi-bin/data/testdap/plot.comp.pl`.

5.7.3 Appendix C: Power and Thrust Curves

The power and thrust curves of the wind turbines from the Belgian offshore wind farms are extracted from various sources (see Table 5.3) and are plotted in Fig. 5.18. In some cases, in lieu of actual turbine data in the public domain, we had to utilize data from proxy turbines with similar characteristics.

Table 5.3: Sources of Power and Thrust Curves

Turbine	Power Curve	Thrust Curve
Vestas V90 3 MW	Source: manufacturer	Source: Bot[58]
Vestas V112 3 MW	Source: manufacturer	Source: manufacturer
Senvion (formerly REPower) 5 MW	Source: windPRO	Source: windPRO
Senvion 6.2 MW	Source: manufacturer	Proxy: Senvion 5 MW
Alstom 6 MW	Proxy: ECN 6 MW[59]	Proxy: ECN 6 MW[59]

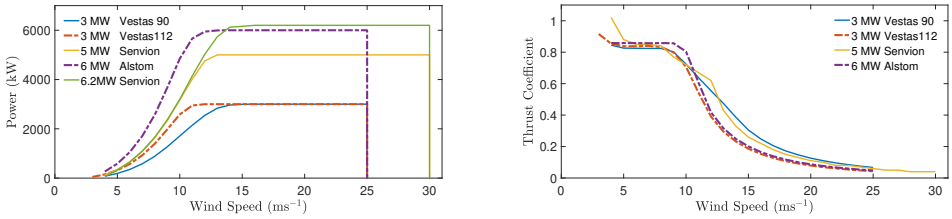

Figure 5.18: Power curves (left panel) and thrust curves (right panel) of the turbines from the Belgian offshore wind farms.

References

[1] Bowen Li et al. “Mesoscale modeling of a “Dunkelflaute” event”. In: *Wind Energy* 24.1 (2021), pp. 5–23.

[2] Commission European. *Report from the Commission to the European Parliament, the Council, the European Economic and Social Committee and the committee of the regions on the implementation of EU macro-regional strategies*. Tech. rep. Technical Report. https://eur-lex.europa.eu/legal-content/EN/TXT/?uri=COM:2019:21:FIN. Accessed June 19, 2019. European Commission. Brussels, 2019.

[3] European Commission. “Energy Roadmap 2050”. In: (2012), pp. 1–20.

[4] M Müller et al. *Translate COP21 - 2045 outlook and implications for offshore wind in the North Seas*. Tech. rep. Technical Report. Online: https://www. ecofys.com/en/publications/translate-cop21/. Accessed June 20, 2019. Ecofys. Utrecht, 2017.

[5] CONCERE. *National Energy and Climate Plans (NECPs) - Belgium. Plan National intégré Energie Climat Belge 2021-2030*. Tech. rep. Technical Report. https://ec.europa.eu/energy/sites/ener/fi
Accessed June 20, 2019. Commission nationale Climat. Belgium, 2018.

[6] *Energy Agenda: Towards a low-carbon energy supply*. Tech. rep. Technical Report. https://www.government.nl/binaries/government/documents/reports/2017/03/01/energy-agenda-towards-a-low-carbon-energy-supply/Energy+agenda.pdf. Accessed June 20, 2019. Ministry of Economic Affairs, The Netherlands, 2017.

[7] F Huneke, C Perez Linkenheil, and M Niggemeier. *Kalte Dunkelflaute: Rubustheit des Stromsystems bei Extremwetter*. Tech. rep. Technical Report. Energy Brain Pool, Greenpeace Energy, Berlin, 2017.

[8] NOS. *Netbeheerder moest groot inkopen om stroomtekort op te vangen*. https://nos.nl/artikel/2229787-netbeheerder-moest-groot-inkopen-om-stroomtekort-op-te-vangen.html. Accessed June 20, 2019. 2018.

[9] NRC. *Netbeheerder Tennet wendt landelijk stroomtekort af*. https://www.nrc.nl/nieuws/2018/04/30/landelijk-stroomtekort-afgewend-door-netbeheerder-tennet-a1601355. Accessed June 20, 2019. 2018.

[10] VRT. *België telde negen dagen Dunkelflaute in januari*. https://www.vrt.be/vrtnws/nl/2017/02/24/belgie_telde_negendagendunkelflauteinja
1-2900900/. Accessed January 26, 2022. 2017.

[11] Elia. *Electricity Scenarios for Belgium towards 2050, Elia's Quantified Study on the Energy Transition in 2030 and 2040*. Tech. rep. Technical Report. Elia. Brussels, 2017.

[12] Frank Meinke-Hubeny et al. "Energy transition in Belgium–Choices and costs". In: *EnergyVille in Opdracht van Febeliec: Genk, Belgium* (2017).

[13] CREG. *Study on the functioning and price evolution of the Belgian wholesale electricity market - monitoring report 2017*. Tech. rep. Technical Report. Commission for Electricity and Gas Regulation. Brussels, 2018.

[14] D Wetzel. *Die Dunkelflaute bringt Deutschlands Stromversorgung ans Limit*. https://www.welt.de/wirtschaft/article161831272/Die-Dunkelflaute-bringt-Deutschlands-Stromversorgung-ans-Limit.html. Accessed June 20, 2019. 2017.

[15] S Schultz. *Ist der Winter wirklich zu düster für den Ökostrom?* https://www.spiegel.de/wirtschaft/soziales/oekostrom-knapp-panikmache-mit-der-dunkelflaute-a-1133450.html. Accessed June 20, 2019. 2017.

[16] Deutscher Bundestag. *Sicherstellung der Stromversorgung bei Dunkelflauten*. Tech. rep. Technical Report. Deutscher Bundestag, WD 5: Wirtschaft und Verkehr, Ernährung, Landwirtschaft und Verbraucherschutz. Berlin, 2019.

[17] William C Skamarock and Joseph B Klemp. "A time-split nonhydrostatic atmospheric model for weather research and forecasting applications". In: *Journal of computational physics* 227.7 (2008), pp. 3465–3485.

[18] William C Skamarock et al. "A description of the Advanced Research WRF version 3. NCAR Technical note-475+ STR". In: (2008).

[19] A Watts. *Weather Wise: Reading Weather Signs*. Adlard Coles. London, 2013.

[20] O Perkins. *Reading the Clouds: How You Can Forecast the Weather*. Bloomsbury Publishing. London, 2018.

[21] D N Robinson. "Describing the weather in Lincolnshire dialect". In: *Weather* 23 (1968), pp. 72–74.

[22] CKM Douglas. "Clouds as seen from an aeroplane". In: *Q J Roy Meteor Soc* 46.195 (1920), pp. 233–242.

[23] M Allaby. *Encyclopedia of Weather and Climate*. Facts on File. Atlanta, 2007.

[24] J Weller and JE Thornes. "An investigation of winter nocturnal air and road surface temperature variation in the West Midlands, UK under different synoptic conditions". In: *Meteorological Applications* 8.4 (2001), pp. 461–474.

[25] J Galvin. "Anticyclonic gloom". In: *Weather* 59 (2004), pp. 236–236.

[26] C H B Priestley and W C Swinbank. "Vertical transport of heat by turbulence in the atmosphere". In: *Proc. Roy. Soc. Lon. Ser. A* 189 (1947), pp. 543–561.

[27] GD Robinson. "The vertical convective heat flux in the atmosphere–a critical essay". In: *Q J Roy Meteor Soc* 77.331 (1951), pp. 61–73.

[28] C-H Moeng. "Large-eddy simulation of a stratus-topped boundary layer. Part I: Structure and budgets". In: *J Atmos Sci* 43 (1986), pp. 2886–2900.

[29] P G Duynkerke et al. "Observations and numerical simulations of the diurnal cycle of the EUROCS stratocumulus case". In: *Q J Roy Meteorol Soc* 130 (2004), pp. 3269–3296.

[30] B Stevens et al. "Evaluation of large-eddy simulations via observations of nocturnal marine stratocumulus". In: *Mon Wea Rev* 133 (2005), pp. 1443–1462.

[31] ENTSOG. *Winter Review 2016/2017*. Tech. rep. Technical Report. European Network of Transmission System Operators for Gas. Brussels, 2017.

[32] C Anagnostopoulou et al. "The exceptionally cold January of 2017 over the Balkan Peninsula: a climatological and synoptic analysis". In: *Atmosphere* 8.12 (2017), p. 252.

[33] K Clement-Nyns. *Forecast and actual wind power generation*. Tech. rep. Technical Report. https://www.elia.be/~/media/files/Elia/Grid-data/Power%20Generation/WindForecasting_EN.pdf. Accessed June 20, 2019. Elia. Brussels, 2016.

[34] J Smet. *Forecast and actual solar-PV power generation*. Tech. rep. Technical Report. https://www.elia.be/~/media/files/Elia/Grid-data/Power%20Generation/SolarForecasting_EN.pdf. Accessed July 17, 2020. Elia. Brussels, 2017.

[35] DNV-GL. *Assessment Wind Measurement Program North Sea*. Tech. rep. 14-2781, Rev. 1. 57 pp. 2014.

[36] AS Fugro Norway. *Supply of Meteorological and Oceanographic data at Borssele Wind Farm Zone (BWFZ), Monthly Progress Report: Period 26 December 2016- 26 January 2017*. Tech. rep. Technical Report. https://offshorewind.rvo.nl/file/download/49027622/Data+%26amp%3B+Val +Fugro. Accessed June 20, 2019. The Netherlands Enterprise Agency (RVO). Utrecht, 2017.

[37] AS Fugro Norway. *Supply of Meteorological and Oceanographic data at Borssele Wind Farm Zone (BWFZ), Monthly Progress Report Period: 26 January- 26 February 2017*. Tech. rep. Technical Report. https://offshorewind.rvo.nl/file/download/50256672/Data+%26amp%3B+Va +Fugro. Accessed June 20, 2019. The Netherlands Enterprise Agency (RVO). Utrecht, 2017.

[38] AS Fugro Norway. *Supply of Meteorological and Oceanographic data at Hollandse Kust (zuid), Monthly Progress Report Period: January 2017*. Tech. rep. Technical Report. https://offshorewind.rvo.nl/file/view/50355882/Data+%26amp%3B+Reports+- +January+2017+-+Fugro. Accessed June 20, 2019. The Netherlands Enterprise Agency (RVO). Utrecht, 2017.

[39] AS Fugro Norway. *Hollandse Kust (zuid) Field Measurement Campaign, Validation Report - January 2017*. Tech. rep. Technical Report. https://offshorewind.rvo.nl/file/view/50355882/Da +January+2017+-+Fugro. Accessed June 20, 2019. The Netherlands Enterprise Agency (RVO). Utrecht, 2017.

[40] ECN. *LEG: Introductie*. https://windopzee.net/lichteiland-goeree-leg/. Accessed July 4, 2019. 2016.

[41] ECN. *EPL: Introductie*. https://windopzee.net/europlatform-epl/. Accessed July 4, 2019. 2016.

[42] RMI. *Automatic weather station (AWS) daily observations*. https://data.gov.be/en/dataset/aws1day. Accessed July 4, 2019. 2016.

[43] University of Wyoming. *Wyoming Atmospheric Soundings*. http://weather.uwyo.edu/upperair/sounding.html. Accessed November 13, 2019. 2019.

[44] F Chen and J Dudhia. "Coupling an advanced land surface–hydrology model with the Penn State–NCAR MM5 modeling system". In: *Mon Weather Rev* 129.4 (2001), pp. 587–604.

[45] MJ Iacono et al. "Radiative forcing by long-lived greenhouse gases: Calculations with the AER radiative transfer models". In: *J Geophys Res Atmos* 113.D13103 (2008).

[46] SY Hong, J Dudhia, and SH Chen. "A revised approach to ice microphysical processes for the bulk parameterization of clouds and precipitation". In: *Mon Weather Rev* 132.1 (2004), pp. 103–120.

[47] JS Kain. "The Kain–Fritsch convective parameterization: an update". In: *J Appl Meteorol* 43.1 (2004), pp. 170–181.

[48] M Nakanishi and H Niino. "An improved Mellor–Yamada level-3 model: Its numerical stability and application to a regional prediction of advection fog". In: *Bound-Lay Meteorol* 119.2 (2006), pp. 397–407.

[49] SY Hong, Y Noh, and J Dudhia. "A new vertical diffusion package with an explicit treatment of entrainment processes." In: *Mon Weather Rev* 134.9 (2006), pp. 2318–2341.

[50] Song-You Hong. "A new stable boundary-layer mixing scheme and its impact on the simulated East Asian summer monsoon". In: *Q J Roy Meteorol Soc* 136 (2010), pp. 1481–1496.

[51] AC Fitch et al. “Local and mesoscale impacts of wind farms as parameterized in a mesoscale NWP model”. In: *Mon Weather Rev* 140.9 (2012), pp. 3017–3038.

[52] C3S. *ERA5: Fifth generation of ECMWF atmospheric reanalyses of the global climate*. `https://cds.climate.copernicus.eu/cdsapp#!/home`. Accessed February 20, 2020. 2017.

[53] P Berrisford et al. *The ERA-interim archive*. Tech. rep. https://www.ecmwf.int/node/8173. Accessed July 17, 2020. ECMWF, Reading, UK, 2009.

[54] G Spellman. “Analysing air pollution meteorology”. In: *Weather* 53 (1998), pp. 34–42.

[55] GR McGregor, S Walters, and J Wordley. “Daily hospital respiratory admissions and winter air mass types, Birmingham, UK”. In: *Int J Biometeorol* 43.1 (1999), pp. 21–30.

[56] A M Varela et al. “Astronomical site selection: on the use of satellite data for aerosol content monitoring”. In: *Mon Not R Astronom Soc* 391 (2008), pp. 507–520.

[57] N Dunstone et al. “Predictability of European winter 2016/2017”. In: *Atmos Sci Lett* 19 (2018), e868.

[58] E T G Bot. *FarmFlow validation against full scale wind farms*. Tech. rep. ECN-E--15-045. https://publications.ecn.nl/ECN-E--15-045. Accessed June 20, 2019. ECN Wind Energy. Petten, 2015.

[59] B H Bulder et al. *Quick scan wind farm efficiencies of the Borssele location*. Tech. rep. ECN-E--14-050. https://publications.ecn.nl/ECN-E--14-050. Accessed June 20, 2019. ECN Wind Energy. Petten, 2015.

6

Estimation of 'Dunkelflaute' Events using Gradient Boosting Machines

In Europe's energy system, wind and solar power generation are projected to develop considerably in the coming years, so its estimation during unfavorable weather conditions, such as Dunkelflaute (near-calm, overcast conditions), is crucial. In recent literature, physics-based models, known as mesoscale models, have been used for such predictions. The purpose of this study is to investigate whether we can utilize machine learning algorithms as viable alternatives to mesoscale models for Dunkelflaute predictions. In particular, gradient-boosting machines are applied to predict solar and wind power (both onshore and offshore) production directly from observational datasets. The proposed approach outperforms a popular mesoscale model (called the Weather Forecasting and Research model), as well as a random forest model. In addition, the proposed approach allowed us to quantify the importance of various meteorological features in the prediction of Dunkelflaute events.

As wind and solar power play an increasingly prominent role in the European energy system, extreme weather events (e.g., Dunkelflaute events) can have significant impacts on power production [1, 2, 3, 4, 5, 6]. Northern European countries may experience Dunkelflaute events several times a year when wind and solar energy levels are very low for a few consecutive days [4]. They can challenge the reliability of power system operation in terms of the balance between electricity supply and demand. It is therefore imperative to predict these Dunkelflaute events in advance and plan the grid system for the upcoming shortage of power production. Reliable predictions can play a key role in electricity dispatching and the stable operation of the power system, and in turn, can help reduce the reserve capacity and the operating cost of the power system.

The first study on the estimation of Dunkelflaute events was conducted by [5]. They investigated the capability of a physics-based mesoscale model, called the Weather Research and Forecasting (WRF) model, to simulate (hindcast) Dunkelflaute events in Belgium in January 2017. Through comprehensive validation, they demonstrated the capability of the WRF model to predict wind speed and insolation fields during Dunkelflaute events. Similar high-level performances of other physics-based models in the prediction of wind speed [7, 8] and wind power [9, 10] have been reported in the literature.

Although physics-based models are quite capable of forecasting wind and solar power, there is significant room for improvements [11]. These types of models are susceptible to errors in initial and boundary conditions, as well as to imperfections in numerical and physical parameterizations [12]. They also require significant amounts of computational resources. Thus, it is worth investigating if machine learning-based approaches can provide at-par or better power predictions at a reduced cost. We address this question in this study, albeit with a focus on Dunkelflaute events.

ML is an artificial intelligence approach that learns intricate structures from large datasets and makes predictions or decisions for specific purposes [13, 14]. It has been widely used in many aspects of the atmospheric science field recently, such as cloud image classification [15], weather forecasting [16, 17], solar and wind energy forecasting [18] , *etc.* Besides, ML techniques have shown their potential for clustering weather patterns of wind speed and insolation and identifying Dunkelflaute periods that occurred in a specified country [6]. Based on the study of [6], a reliable estimation of Dunkelflaute events is significantly valuable for the next steps and can provide early warning of such events.

To handle the aforementioned uncertainties in power forecasting from NWP models, machine learning approaches have also been implemented to establish a hybrid model. For example, [19] applied feature selection approaches and Long Short-Term Memory to correct the errors of WRF output. This deep learning network has reduced the errors from numerical simulation by around 30%. Besides, ML algorithms can post-process wind-related features, which are forecasted by numerical weather models, to output power production. Typical research is done by [20], who applied Multilayer Perceptron on the decomposed time-series components for power forecasting utilizing the historical and NWP datasets. Other algorithms including gradient boosting machines [21], support vector machine, and artificial neural network [22] also perform well in different research. These hybrid approaches are also efficient in solar power forecasting, either correcting the prediction errors from numerical simulation [23] or outputting power production based on the solar-related features from numerical models [24]. Therefore, ML algorithms are efficient in

power production forecasting and have the potential to forecast Dunkelflaute periods.

This is the first research using ML algorithms to estimate wind and solar power production during the Dunkelflaute periods. A gradient boosting machine is employed to predict solar, offshore wind, and onshore wind power production with observational datasets. The rest of the paper is organized as follows. We briefly introduce ML algorithms in Section 2. The datasets used in the experiments are described in Section 3. In Section 4, we discuss the proposed algorithms. Prediction and comparison results are documented in Section 5 followed by a summarized discussion in Section 6.

6.1 Decision Tree-based Forecasting Approaches

6.1.1 Decision Tree Regression

Decision tree (DT)-based approaches are among the most effective ML workhorses for tabular regression problems. Recent AIML competitions have shown that DT methods provide impressive accuracy in sales forecasting and other applications [25, 26]. DTs employ explanatory variables (called features in the ML literature) to predict a dependent variable (or target). Given that DTs are a rule-based regression approach, their training requires decisions on several factors, including the feature chosen for splitting the root and each branch, the rule (cut-point value) to use on each selected feature for performing the splitting, and the condition for stopping the splitting. These decisions are automatically made by the algorithm utilized to train the model.

For the input n samples each with feature vector $\boldsymbol{x} \in \mathbf{R}^l$ and the target value $y \in \mathbf{R}$, where l is the feature scale, a DT algorithm recursively splits the feature space to group the samples with similar target values. For a specific node set A_m with n_m samples, a possible splitting threshold $t_{m,j}, j \in [1,l]$ may split the set into two subsets $A_{m,1}$ and $A_{m,2}$ [27, 28]:

$$\begin{aligned} A_{m,j,1} &= \{(\boldsymbol{x}, \boldsymbol{y}) | \boldsymbol{x}(j) < t_{m,j}\} \\ A_{m,j,2} &= A_m \backslash A_{m,j,1} \end{aligned} \tag{6.1}$$

where $\boldsymbol{x}_j$ is the jth column of $\boldsymbol{x}$, representing the sample vector corresponding to the jth feature. To optimize the parameters of the DT model, an optimization process is applied to minimize the ensemble loss:

$$\begin{aligned} E(A_m, j) &= \frac{n_{m,j,1}}{n_m} L(A_{m,j,1}) + \frac{n_{m,j,2}}{n_m} L(A_{m,j,2}) \\ t^*_{m,j} &= \arg\min_{t_{m,j}} E(A_m, j) \end{aligned} \tag{6.2}$$

where, $n_{m,j,1}$ is the sample number in $A_{m,1}$, $n_{m,j,2}$ is the sample number in $A_{m,2}$, and $L(\cdot)$ is the loss function. Usually, the mean square error is used as the loss function:

$$L(A) = \frac{1}{n_a} \sum_{y \in A} (y - \frac{1}{n_a} \sum_{y \in A} y)^2 \tag{6.3}$$

where n_a is the sample number in the node set A. After the optimization, the two subsets $A_{m,1}$ and $A_{m,2}$ becomes two new node sets, and the tree continuously grows by iterating the aforementioned steps. The split of the node set stops when the tree reaches the maximum depth or the sample number is below the minimum one. For any input feature vector $\boldsymbol{x_0}$, the prediction by the DT model $T(\cdot)$ is:

$$\hat{y_0} = T(x_0) = \frac{1}{n_a} \sum_{y \in A} y, \text{ if } x_0 \in A \tag{6.4}$$

However, the algorithm used for training a single DT can be sensitive to randomness and extreme values even if the DT is pruned and trimmed. In order to tackle the limitation and improve accuracy, the methods to create ensembles (combinations) of multiple DTs have been proposed. Here, we introduce two widely used methods, Random Forests (RFs) [29, 30] and Gradient Boosting (GB) [31].

6.1.2 Random Forest Regression

RF regression is an ensemble learning approach that constructs multiple DTs for the regression task. Specifically, each DT has access to a different subset of variables at each node and the results from these tree models are averaged. In this way, the forecasts can be less sensitive to extreme values and can reduce variance more than individual models.

For the input n samples each with feature vector $\boldsymbol{x} = (x_1, x_2, ..., x_l) \in \mathbf{R}^l$ and the target value $y \in \mathbf{R}$, a random subspace of feature vector $\boldsymbol{x_{s_i}} = (x_{j1}, x_{j2}, ...)$ and the target value y can be used to train a DT model T_i with the aforementioned algorithm. By randomly constructing M trees, the prediction of the RF model on the input feature vector $\boldsymbol{x_0}$ is:

$$\hat{y_0} = \frac{1}{M} \sum_{i=1}^{M} T_i(x_0) \tag{6.5}$$

One issue of RFs is that bias reduction cannot be achieved since each tree is built on a bootstrap sample with quite similar distribution as the initial training set. Therefore, it is worth exploring other DT-based approaches.

6.1.3 Gradient Boosting Regression

GB combines successive weak learners to focus on the resulted errors sequentially through boosting approach and model the residuals adaptively for all the data so that each new tree improved on the forecast accuracy of the existing trees [32, 33]. As a result, GB reduces both bias and variance [34, 18], and its results mostly outperform RFs in more specialized applications [35].

For the input n samples each with feature vector $\boldsymbol{x} \in \mathbf{R}^l$ and the target value $y \in \mathbf{R}$, the GB regression calculates the ensemble prediction as:

$$\hat{y} = G_M(x) = \sum_{i=1}^{M} T_i(x) \tag{6.6}$$

where, $G_M(\cdot)$ represents the GB model and $T_i, i = 1, 2, ..., M$ are the DT models. These DT models are weak learners as the tree size is limited. The GB algorithm constructs the DT recursively as:

$$G_m(x) = G_{m-1}(x) + T_m(x) \tag{6.7}$$

Therefore for each step, a new DT model is implemented to minimize the ensemble loss:

$$T_m(x) = \arg\min_{T_m} \sum_{(x,y)\in S} L(y, G_m(x)) = \arg\min_{T_m} \sum_{(x,y)\in S} L(y, G_{m-1}(x) + T_m(x)) \tag{6.8}$$

where, $L(\cdot)$ is the loss function, which is usually a square error function $L(y,\hat{y}) = (y-\hat{y})^2$, and S is the sample set. To simplify the calculation, a first-order Taylor approximation is used to estimate the loss:

$$L(y, G_{m-1}(x) + T_m(x)) \approx L(y, G_{m-1}(x)) + T_m(x)[\frac{\partial L(y, G_{m-1}(x))}{\partial G_{m-1}(x)}] \tag{6.9}$$

where, $g_m(x) = \frac{\partial L(y, G_{m-1}(x))}{\partial G_{m-1}(x)}$ is the partial derivative of the loss function. Then the equation (6.10) can be rewritten as:

$$T_m(x) = \arg\min_{T_m} \sum_{(x,y)\in S} T_m(x) g_m(x) \tag{6.10}$$

The DT model generated from this minimizing optimization is thereby proportional to the negative gradient $-g_m(x)$. Since the ensemble loss is minimized, the updated GB model results in smaller errors by implementing the new DT. Therefore, the bias and variance decrease with the GB algorithm.

There are several variants of the GB method in common use, like Light gradient boosting machine [36] (LightGBM), XGBoost [37], or Categorical Boosting (CatBoost) [38]. These methods all share the same idea of gradient boosting but differ in the way they grow or aggregate the individual trees. Among these, XGBoost, has been used by the top winners in Kaggle competitions [37], and CatBoost shows promising performance especially for generalization accuracy [38]. Recently, light gradient boosting machine (LightGBM) has shown its excellent performance of high prediction accuracy, fast training speed and reduced memory consumption to process large data sets, and ability to minimize over-fitting problems.

Regarding lightGBM, the major differences from XGBoost are the deployment of histogram-based algorithms and a leaf-wise growth strategy with depth constraints. For the histogram algorithm, there is no extra storage requirement for the pre-sorted results, and the value after the discretization of features can be stored with an 8-bit integer. Instead of using a level-wise growth strategy, LightGBM employs a more effective leaf-wise method, which finds the leaves with the highest accuracy at each step throughout all the leaves. These two algorithms together with the depth limitation make it achieve high accuracy with less time and memory consumption [35]. As a result, it has been widely used in many fields, e.g. music recommendation [39], acoustic scene classification [40], and smart grid load forecasting [41]. LightGBM was also used by most of the winning teams in the M5, demonstrating the method's ability to forecast multiple time series of diverse patterns and features [42]. It has not yet been applied in estimating wind and solar power production during the Dunkelflaute periods, which is a concern in our research.

6.2 Description of the Datasets

6.2.1 Reanalysis Data

For the purpose of Belgian Dunkelflaute estimation, time series of gridded meteorological reanalysis data and historical power production data are used as input features and corresponding outputs, respectively. Since observed meteorological data can be sparsely located and temporally discontinuous, the ERA5 reanalysis dataset from the European Centre for Medium Range Weather Forecasts [43] is used instead in this study. It contains the hourly data with a spatial resolution of ~31 km, which is the highest among its counterparts. In addition, this dataset was demonstrated reliable for capturing numerous traits of Dunkelflaute events [4, 5, 6].

The previous studies of Gradient Boosted (GB) trees emphasize the importance of including more features to achieve smaller errors [44]. Therefore, many meteorological variables from ERA5 are used as input features. The local wind speed, solar radiation flux and cloud cover are closely related to the Dunkelflaute events so these variables at different heights are included. Besides, some variables describing the stability of the boundary layer are considered, including the boundary layer height, temperature, heat fluxes, and surface pressure. Other preprocessed variables like the sine or cosine formats of the day and hour to be estimated are also included.

For forecasting outputs, the data of aggregated wind and solar power production in Belgium are obtained from the system operator Elia (https://www.elia.be). These measured power data are aggregated from the sampling rate of 15 min to 60 min to be consistent with the hourly meteorological data from ERA5. All the data in 2016 are divided into training and validation sets, and those from January and February of 2017 are used as two test sets. In January 2017, Belgium experienced a total of nine days of Dunkelflaute [5], which is concerned with evaluating the ML forecasting model.

6.2.2 Location Selected of Parameters

The interested domain for the forecasting is chosen as 49°N to 52°N and 2°E to 7°E, which covers the Belgian onshore and offshore areas. The weather variables at one or more locations in the domain grid will be chosen as the LightGBM model input.

At the domain grid, the correlation coefficients between the power production and the related meteorological variable are calculated in order to find the most power-related locations where we retrieve ERA5 variables for the modeling. Figure 6.1 shows the correlation coefficients between solar power and mean surface downward long-wave radiation flux (MSDWSWRF), as well as those between wind power and 100-meter wind speed (M100). It is clear that the highest coefficients for solar and onshore wind power are obtained in the middle of the domain; while for offshore wind power, the highest coefficient locates in the Belgian offshore region. Considering all these three power, we find the three points with the highest coefficients, which are p1 (50.75°N, 4.5°E), p2 (51.75°N, 3°E), and p3 (50.5°N, 5.5°E). ERA5 variables at points (p1), (p1, p2), and (p1, p2, p3) will be input into three LightGBM models, called LGB - 1GP, LGB - 2GP, and LGB - 3GP, respectively.

Taking the p1 location as an example, the correlations between the above power and the corresponding weather variables are illustrated in Figure 6.2. The linear correlation between solar power and irradiance is quite clear. For wind power, there is a trend similar

Table 6.1: Variables retrieved from ERA5 used to predict power.

Feature Number	Symbol	Variable	Unit	Feature Number	Symbol	Variable	Unit
1	**BLH**	Boundary layer height	m	**2**	**LSM**	Land-sea mask	-
3	**MSL**	Mean sea level pressure	Pa	**4**	**SP**	Surface pressure	Pa
5	**SST**	Sea surface temperature	K	**6**	**TCC**	Total cloud cover	-
7	**CAPE**	Convective available potential energy	J kg**-1	**8**	**M10**	10 metre wind speed	m s**-1
9	**SinX10**	Sine of 10 metre wind direction	-	**10**	**CosX10**	Cosine of 10 metre wind direction	-
11	**D2M**	2 metre dewpoint temperature	K	**12**	**LCC**	Low cloud cover	-
13	**ISHF**	Instantaneous surface sensible heat flux	W m**-2	**14**	**SKT**	Skin temperature	K
15	**T2M**	2 metre temperature	K	**16**	**M100**	100 metre wind speed	m s**-1
17	**SinX100**	Sine of 100 metre wind direction	-	**18**	**CosX100**	Cosine of 10 metre wind direction	-
19	**I10FG**	Instantaneous 10 metre wind gust	m s**-1	**20**	**SinDay**	Sine of day number in a year	-
21	**CosDay**	Cosine of day number in a year	-	**22**	**SinHour**	Sine of hour number in a day	-
23	**CosHour**	Cosine of hour number in a day	-	**24**	**MSDWSWRF**	Mean surface downward short-wave radiation flux	W m**-2
25	**MSDWLWRF**	Mean surface downward long-wave radiation flux	W m**-2				

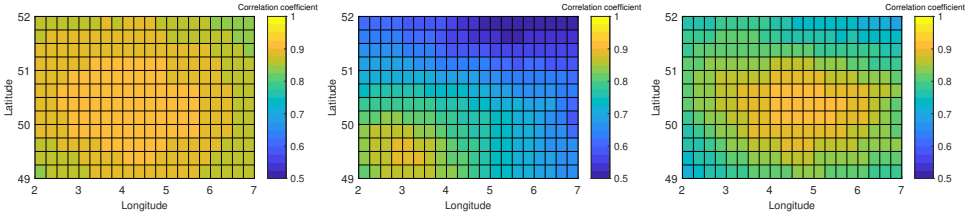

Figure 6.1: Correlation coefficients of power data and related variables. We use data for the year of 2016.

to the wind power curve with a cut-in speed of 3-4 m/s, and a cut-off speed of around 20 m/s. Compared with offshore wind power, the slope of the onshore one is relatively gentle.

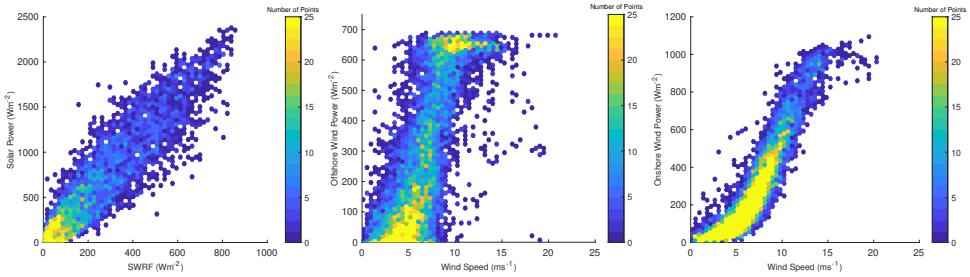

Figure 6.2: Bivariate histogram of power data and related variables. We use data at p1 for the year of 2016.

6.3 Methodology

6.3.1 Model Training

While there are a handful of features that can be used for the tree model, it is important to decide on useful features depending on whether these features can provide a split that decreases the forecast error. Therefore, hyper-parameters, such as maximum tree depths and leaves, are important to control the configuration of the tree, e.g., avoiding the conditions that the trees are too shallow or too deep. In order to optimize the hyper-parameters for the LightGBM model, an auto ML software called 'FLAML' is used. FLAML can automatically tune the hyper-parameters to find the accurate model at low computational cost [45]. It uses a re-sample strategy to reduce the required training sample for each learner and then calculates the estimated computational cost to either recursively increase the sampling size or use new hyper-parameter configurations. Another advantage of FLAML is that it can include models like RF and XGBoost, which can be used for comparison. While training the models, K-fold cross-validation is employed with the k of 5. The hyper-parameters are optimized by minimizing the validation error. The Mean Absolute Error (MAE) is used since the deviation can be obtained directly and it is widely used in the renewable energy area [18]. Then the model with optimized hyper-parameters is used for forecasting January or February of 2022.

6.3.2 ELI5

After training the LightGBM model, it is crucial to understand the effect of each feature on the model output. ELI5 is a visualization tool in Python, and it can evaluate feature importance for tree-based models [46, 47]. To compute the importance of each feature, only this input feature is randomly shuffled in the test data and a new prediction is made. The reduction of the square errors between the new prediction and the original one represents the feature importance. Therefore, a feature is more significant with a larger reduction, and this approach can be a good measure of feature importance to interpret the estimation results.

6.4 Results

6.4.1 Prediction of Power using LightGBM

As aforementioned, three LightGBM models (LGB - 1GP, LGB - 2GP, and LGB - 3GP) are trained with 25, 46, and 67 input variables, respectively. The performance of the models is evaluated by comparing the estimation with the observed power data. The comparison of estimated solar, offshore wind and onshore wind power with observed power are presented in Fig. 6.3, Fig. 6.4, and Fig. 6.5, respectively. The measured time series are in black while the estimated ones are in red.

It is clear in Fig. 6.3 that solar power is estimated well with the model of LGB - 1GP for both test sets. However, the model does not achieve a good performance in wind power estimation. Although the estimated trends are similar to the measured power, the short-time fluctuations show large biases. Besides, for the second test set, the time with sudden high wind power production is not promising. The estimation of offshore wind power production is even worse. Neither the extremely low nor the high production are estimated well. The reason can be that only variables from one grid point near the coastal area are not enough to limit the errors.

In the second model, LGB - 2GP, two grid points are considered, one onshore and the other offshore. This model, therefore, requires nearly double the number of input variables. According to Fig. 6.4, the predictions of wind and solar power production have improved considerably. The trends and short-term fluctuations in wind power production are both well estimated. However, sudden high levels of wind power production are still underestimated. Despite this, the model's high performance suggests that two grid points are indeed needed.

The third grid point is then included in LGB - 3GP. However, from the visual point of view, there is no distinct difference when compared with the results from LGB - 2GP.

A summary of the root-mean-square error (RMSE) and coefficient of determination (R^2) for these three models are listed in Table 6.2. The smallest RMSE for all datasets and the best R^2 for test sets are labeled in bold. Overall, LGB - 2GP and LGB - 3GP models outperform the LGB - 1GP model, especially for wind power production. This is due to the different locations of onshore and offshore wind farms. The best LightGBM models achieve a low magnitude of RMSE and high R^2 values, indicating the accurate estimation of the two test sets. For example, the R^2 of estimating solar power is around 0.9 for all three models. For onshore and offshore wind power, the R^2 of LGB - 2GP and LGB - 3GP ranges from 0.84 to 0.91. Their promising performance indicates the remarkably accuracy

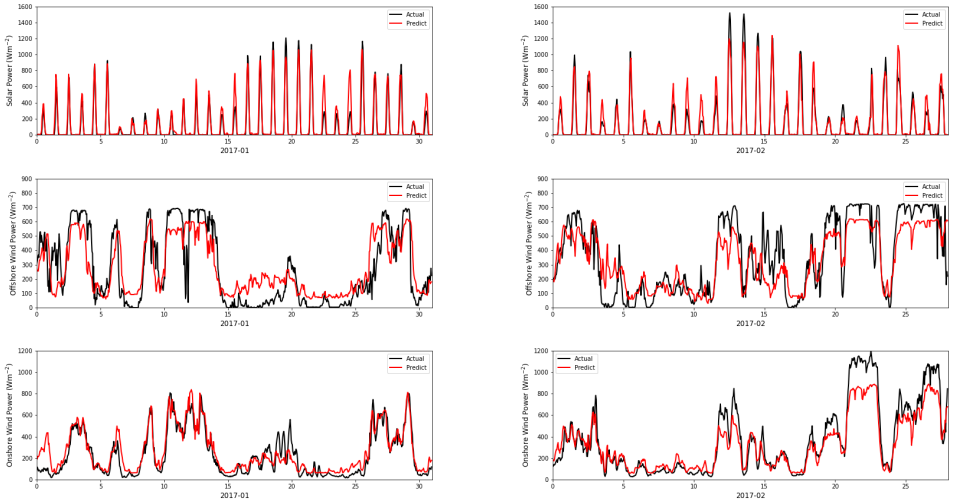

Figure 6.3: Prediction of solar (top panel), offshore wind (middle panel) and onshore wind power (bottom panel) using LGB - 1GP for the first test set: Jan, 2017 (left panel) and the second test set: Feb, 2017 (right panel).

6

regarding the power estimation for the Dunkelflaute and non-Dunkelflaute periods.

Table 6.2: RMSE and R^2 (marked in parentheses) for LGB-1GP, LGB-2GP, LGB-3GP.

LGB Runs	Solar Power				Offshore Wind Power				Onshore Wind Power			
Name	Trn	Val	Tst	Tst2	Trn	Val	Tst	Tst2	Trn	Val	Tst	Tst2
LGB - 1GP	33	**78**	81 (0.86)	88 (0.88)	129	131	137 (0.70)	130 (0.75)	65	65	87 (0.82)	120 (0.85)
LGB - 2GP	**23**	79	71 (0.91)	83 (0.91)	50	**77**	75 (0.91)	**90 (0.87)**	57	63	82 (0.84)	101 (0.90)
LGB - 3GP	38	81	**66 (0.92)**	**79 (0.92)**	**48**	**77**	**74 (0.91)**	104 (0.84)	**51**	**59**	**81 (0.85)**	**94 (0.92)**

6.4.2 ELI5 Results

Taking LGB - 2GP as an example, we use ELI5 to understand the modeling results and feature importance (top 6 features in Table 6.3). The features with the highest weight contribute the most to the model prediction. For example, regarding the estimation of solar power, the most correlated variables are the components of surface downward radiation flux. This is reasonable since the irradiance directly determines the power production of solar panels. The components at the offshore grid point (second grid point) matter more than their onshore counterpart.

In terms of the prediction of wind power production, it is promising that the wind speeds at the heights of 100 m and 10 m are the most relevant variables. Other parameters describing the flow, e.g. instantaneous wind gusts are also of great importance in the prediction. Besides, boundary-layer-related parameters are also important. Including these variables can provide extra information on the thermal and convective processes in the boundary layer, which have a close correlation with the occurrence of Dunkelflaute ([5, 4]). It turns out that these variables are indeed among the most important components for the modeling.

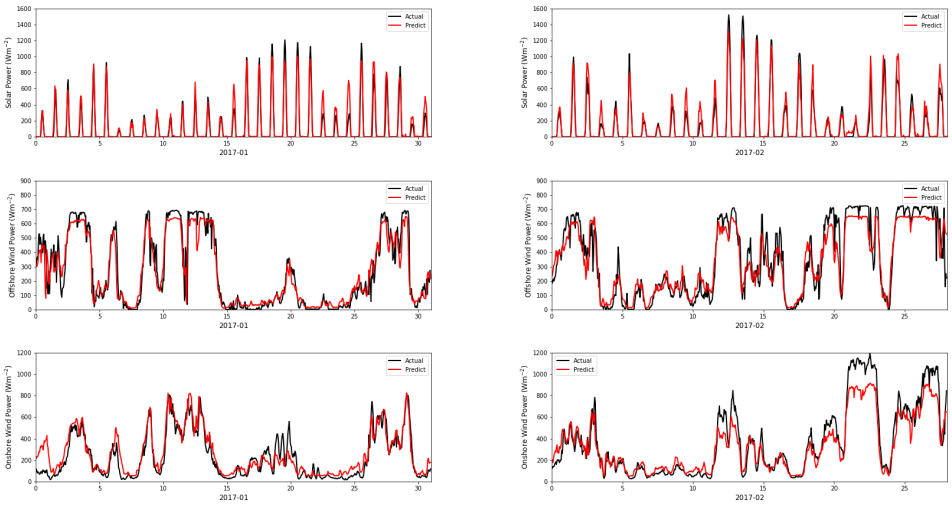

Figure 6.4: Same as Fig. 6.3, except for using LGB - 2GP.

Table 6.3: Weights of Top Features for the LGB-2GP Model.

Solar	**Feature**	MSDWSWRF-p2	MSDWLWRF-p2	MSDWSWRF-p1	MSDWLWRF-p1	ISHF-p2	SKT-p2
	Weight	0.352	0.246	0.153	0.082	0.022	0.022
Offshore wind	**Feature**	M100-p1	M10-p1	I10FG-p1	M100-p2	M10-p2	BLH
	Weight	0.323	0.290	0.141	0.065	0.043	0.020
Onshore wind	**Feature**	M100-p2	I10FG-p2	M10-p2	M100-p1	M10-p1	ISHF-p2
	Weight	0.598	0.228	0.070	0.057	0.030	0.012

6.4.3 Comparison with Other Tree-based Models

Two other tree-based models, RF and XGBoost, are compared with LightGBM for performance evaluation. The input variables are from 2 or 3 grid points, called 2GP or 3GP. The RMSE and R^2 of the comparison results are shown in Table 6.4. For solar power estimation, these tree-based models have close performance, with RMSE around 80 MW and R^2 around 0.9. For wind power estimation, the LightGBM model outperforms the other two, with a visible decrease in RMSE and an increase in R^2. However, when estimating onshore wind power on the second test set, XGBoost seems to be more promising than LightGBM. Nonetheless, the overall better performance indicates that LightGBM has advantages in estimating solar and wind power production.

Table 6.4: RMSE and R^2 (marked in parentheses) for XGBoost, RF and LightGBM models.

Models		**Solar Power**		**Offshore Wind Power**		**Onshore Wind Power**	
		Tst	**Tst2**	**Tst**	**Tst2**	**Tst**	**Tst2**
2GP	**XGBoost**	71 (0.91)	84 (0.91)	78 (0.90)	99 (0.85)	83 (0.84)	95 (0.91)
	RF	76 (0.89)	86 (0.90)	77 (0.90)	104 (0.83)	85 (0.83)	113 (0.88)
	LightGBM	71 (0.91)	83 (0.91)	75 (0.91)	90 (0.87)	82 (0.84)	101 (0.90)
3GP	**XGBoost**	69 (0.91)	79 (0.92)	77 (0.90)	112 (0.81)	82 (0.84)	91 (0.92)
	RF	76 (0.89)	84 (0.91)	77 (0.90)	120 (0.78)	84 (0.84)	99 (0.91)
	LightGBM	66 (0.92)	79 (0.92)	74 (0.91)	104 (0.84)	81 (0.85)	94 (0.92)

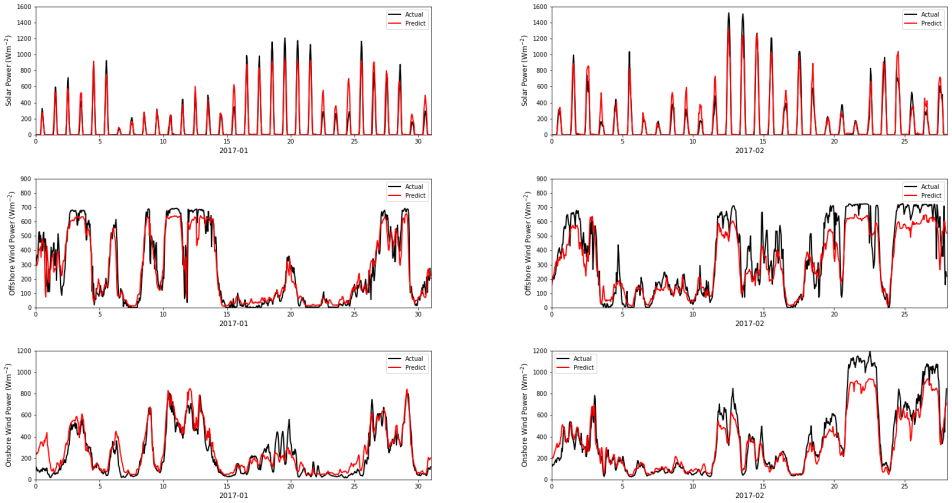

Figure 6.5: Same as Fig. 6.3, except for using LGB - 3GP.

6.4.4 Comparison with WRF-ERA5

In this section, we compare the offshore wind power prediction using LightGBM with that using the state-of-the-art mesoscale model (Weather Research and Forecasting, WRF). For running the WRF model, ERA5 has been used as large-scale forcing data. Wind farm parameterization by [48] is used to simulate the Belgian offshore wind turbines with 182 wind turbines of five different types. The detailed turbine curves, domain configuration, and physical parameterizations can refer to [5].

In the left panel of Fig. 6.6, the WRF model has reproduced the wind power production quite well in comparison with the measured data from Elia. In the right panel of Fig. 6.6, the equally high correlation between the predicted power production using LGM - 2GP and the observed power series is visible. In order to evaluate the overall forecasting performance of the two methods, statistics metrics like root mean square error (RMSE) and coefficient of determination (R^2) are used. The RMSE between WRF-ERA5 and the measured power data is 73MW, and the RMSE between the LGB - 2GP and the measured power data is 44MW. Furthermore, a larger square of the correlation between the predicted value and the actual value is seen for using LGB-2GP (0.94) than using WRF-ERA5 (0.83). The metrics indicate the capability of LightGBM to accurately capture the magnitudes of the power production including the Dunkelflaute periods. It takes less time than numerical modeling, while it outperforms WRF.

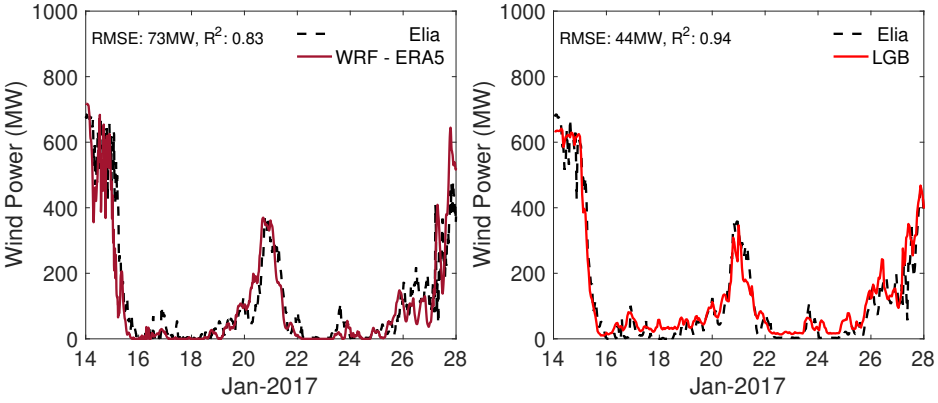

Figure 6.6: Comparison of WRF-ERA5-based and LGB-2GP-based results (Jan, 2017).

6.5 Concluding Remarks

In this work, we estimate wind and solar power production during several Dunkelflaute events via machine learning. This paper is the first to demonstrate the capability of LightGBM for estimating wind and solar power production during Dunkelflaute periods with public-domain data (e.g., reanalysis datasets). The crucial elements for the model are the meteorological variables at the location of onshore or offshore grid points. A high correlation is seen between observed power production and those estimated using LightGBM models, especially the LGB - 2GP and LGB - 3GP. By comparison, the LightGBM models also outperform other tree-based models. It is also clear that the proposed algorithm is applicable in power production not only during the Dunkelflaute periods but also during other time periods.

The prediction of power production includes diverse meteorological variables. In addition to insolation and wind speed, some of the variables (e.g., boundary layer height and sensible heat flux) are closely related to the prediction of solar, onshore, and offshore wind power. The inclusion of these variables in the extra second or third grid point can enhance the overall performance considerably. Furthermore, the power production is reproduced considerably well using mesoscale simulation (WRF), while our LightGBM prediction can even perform better. It is needless to say that the accurate and reliable prediction of the Dunkelflaute events can be of great importance for the maintenance and planning of grid systems.

In this proof-of-concept study, we input variables from the ERA5 reanalysis dataset into the model. The modeling using inputs from other operational models (e.g., GFS) can be a valuable next step for a real-time forecasting scenario. In addition, other machine learning methods may be more effective than our current approach. We hope to experiment with some of these alternatives in our future work.

References

[1] Frank Meinke-Hubeny et al. “Energy transition in Belgium–Choices and costs”. In: *EnergyVille in Opdracht van Febeliec: Genk, Belgium* (2017).

[2] D Wetzel. "Die „Dunkelflaute "bringt Deutschlands Stromversorgung ans Limit". In: *Die Welt "vom* 6 (2017). https://www.welt.de/wirtschaft/article161831272/Die-Dunkelflaute-bringt-Deutschlands-Stromversorgung-ans-Limit.html. Accessed December 18, 2021., p. 2017.

[3] Bowen Li et al. "Quantifying the predictability of a 'Dunkelflaute'event by utilizing a mesoscale model". In: *Journal of Physics: Conference Series*. Vol. 1618. 6. IOP Publishing. 2020, p. 062042.

[4] Bowen Li et al. "A brief climatology of dunkelflaute events over and surrounding the North and Baltic Sea areas". In: *Energies* 14.20 (2021), p. 6508.

[5] Bowen Li et al. "Mesoscale modeling of a "Dunkelflaute" event". In: *Wind Energy* 24.1 (2021), pp. 5–23.

[6] Bowen Li, Sukanta Basu, and Simon J Watson. "Automated Identification of "Dunkelflaute" Events: A Convolutional Neural Network–Based Autoencoder Approach". In: *Artificial Intelligence for the Earth Systems* 1.4 (2022), e220015.

[7] Eric P James, Stanley G Benjamin, and Melinda Marquis. "Offshore wind speed estimates from a high-resolution rapidly updating numerical weather prediction model forecast dataset". In: *Wind Energy* 21.4 (2018), pp. 264–284.

[8] Jaemo Yang et al. "An analog technique to improve storm wind speed prediction using a dual NWP model approach". In: *Monthly Weather Review* 146.12 (2018), pp. 4057–4077.

[9] Christos Stathopoulos et al. "Wind power prediction based on numerical and statistical models". In: *Journal of Wind Engineering and Industrial Aerodynamics* 112 (2013), pp. 25–38.

[10] Madasthu Santhosh, Chintham Venkaiah, and DM Vinod Kumar. "Current advances and approaches in wind speed and wind power forecasting for improved renewable energy integration: A review". In: *Engineering Reports* 2.6 (2020), e12178.

[11] Jing Zhao et al. "An improved multi-step forecasting model based on WRF ensembles and creative fuzzy systems for wind speed". In: *Applied Energy* 162 (2016), pp. 808–826.

[12] Jing Zhao et al. "Multi-step wind speed and power forecasts based on a WRF simulation and an optimized association method". In: *Applied energy* 197 (2017), pp. 183–202.

[13] Yann LeCun, Yoshua Bengio, and Geoffrey Hinton. "Deep learning". In: *nature* 521.7553 (2015), pp. 436–444.

[14] Ian Goodfellow et al. *Deep learning*. Vol. 1. 2. MIT press Cambridge, 2016.

[15] Jinglin Zhang et al. "CloudNet: Ground-based cloud classification with deep convolutional neural network". In: *Geophysical Research Letters* 45.16 (2018), pp. 8665–8672.

[16] Stephan Rasp and Sebastian Lerch. "Neural networks for postprocessing ensemble weather forecasts". In: *Monthly Weather Review* 146.11 (2018), pp. 3885–3900.

[17] João Trevizoli Esteves, Glauco de Souza Rolim, and Antonio Sergio Ferraudo. "Rainfall prediction methodology with binary multilayer perceptron neural networks". In: *Climate Dynamics* 52.3 (2019), pp. 2319–2331.

[18] Alberto Torres-Barrán, Álvaro Alonso, and José R Dorronsoro. "Regression tree ensembles for wind energy and solar radiation prediction". In: *Neurocomputing* 326 (2019), pp. 151–160.

[19] Weifeng Xu et al. "Multi-step wind speed prediction by combining a WRF simulation and an error correction strategy". In: *Renewable Energy* 163 (2021), pp. 772–782.

[20] Sahra Khazaei et al. "A high-accuracy hybrid method for short-term wind power forecasting". In: *Energy* 238 (2022), p. 122020.

[21] Wenqing Xu, Like Ning, and Yong Luo. "Wind speed forecast based on post-processing of numerical weather predictions using a gradient boosting decision tree algorithm". In: *Atmosphere* 11.7 (2020), p. 738.

[22] Asnor Muizan Ishak et al. "Error correction modelling of wind speed through hydro-meteorological parameters and mesoscale model: a hybrid approach". In: *Water resources management* 27.1 (2013), pp. 1–23.

[23] Sara Pereira et al. "Development of an ANN based corrective algorithm of the operational ECMWF global horizontal irradiation forecasts". In: *Solar Energy* 185 (2019), pp. 387–405.

[24] Dávid Markovics and Martin János Mayer. "Comparison of machine learning methods for photovoltaic power forecasting based on numerical weather prediction". In: *Renewable and Sustainable Energy Reviews* 161 (2022), p. 112364.

[25] Casper Solheim Bojer and Jens Peder Meldgaard. "Kaggle forecasting competitions: An overlooked learning opportunity". In: *International Journal of Forecasting* 37.2 (2021), pp. 587–603.

[26] Spyros Makridakis, Evangelos Spiliotis, and Vassilios Assimakopoulos. "The M4 Competition: 100,000 time series and 61 forecasting methods". In: *International Journal of Forecasting* 36.1 (2020), pp. 54–74.

[27] Roman Timofeev. "Classification and regression trees (CART) theory and applications". In: *Humboldt University, Berlin* 54 (2004).

[28] Clifton D Sutton. "Classification and regression trees, bagging, and boosting". In: *Handbook of statistics* 24 (2005), pp. 303–329.

[29] Leo Breiman. "Random forests". In: *Machine learning* 45.1 (2001), pp. 5–32.

[30] Khaled Fawagreh, Mohamed Medhat Gaber, and Eyad Elyan. "Random forests: from early developments to recent advancements". In: *Systems Science & Control Engineering: An Open Access Journal* 2.1 (2014), pp. 602–609.

[31] Jerome H Friedman. "Stochastic gradient boosting". In: *Computational statistics & data analysis* 38.4 (2002), pp. 367–378.

[32] Llew Mason et al. "Boosting algorithms as gradient descent". In: *Advances in neural information processing systems* 12 (1999).

[33] Jane Elith* et al. "Novel methods improve prediction of species' distributions from occurrence data". In: *Ecography* 29.2 (2006), pp. 129–151.

[34] Jane Elith, John R Leathwick, and Trevor Hastie. "A working guide to boosted regression trees". In: *Journal of animal ecology* 77.4 (2008), pp. 802–813.

[35] Junliang Fan et al. "Light Gradient Boosting Machine: An efficient soft computing model for estimating daily reference evapotranspiration with local and external meteorological data". In: *Agricultural water management* 225 (2019), p. 105758.

[36] Guolin Ke et al. "Lightgbm: A highly efficient gradient boosting decision tree". In: *Advances in neural information processing systems* 30 (2017).

[37] Tianqi Chen and Carlos Guestrin. "Xgboost: A scalable tree boosting system". In: *Proceedings of the 22nd acm sigkdd international conference on knowledge discovery and data mining*. 2016, pp. 785–794.

[38] Liudmila Prokhorenkova et al. "CatBoost: unbiased boosting with categorical features". In: *Advances in neural information processing systems* 31 (2018).

[39] Qingwen Zhang et al. "Improvement of Makkink model for reference evapotranspiration estimation using temperature data in Northwest China". In: *Journal of Hydrology* 566 (2018), pp. 264–273.

[40] Eduardo Fonseca et al. "Acoustic scene classification by ensembling gradient boosting machine and convolutional neural networks". In: *Virtanen T, Mesaros A, Heittola T, Diment A, Vincent E, Benetos E, Martinez B, editors. Detection and Classification of Acoustic Scenes and Events 2017 Workshop (DCASE2017); 2017 Nov 16; Munich, Germany. Tampere (Finland): Tampere University of Technology; 2017. p. 37-41.* Tampere University of Technology. 2017.

[41] Wenjie Zhang, Hao Quan, and Dipti Srinivasan. "Parallel and reliable probabilistic load forecasting via quantile regression forest and quantile determination". In: *Energy* 160 (2018), pp. 810–819.

[42] Spyros Makridakis, Evangelos Spiliotis, et al. "The M5 competition and the future of human expertise in forecasting". In: *Foresight: The International Journal of Applied Forecasting* 60 (2021), pp. 33–37.

[43] Hans Hersbach et al. "The ERA5 global reanalysis". In: *Quarterly Journal of the Royal Meteorological Society* 146.730 (2020), pp. 1999–2049.

[44] Naveen Goutham et al. "Using machine-learning methods to improve surface wind speed from the outputs of a numerical weather prediction model". In: *Boundary-Layer Meteorology* 179.1 (2021), pp. 133–161.

[45] Chi Wang et al. "FLAML: A fast and lightweight automl library". In: *Proceedings of Machine Learning and Systems* 3 (2021), pp. 434–447.

[46] Namita Agarwal and Saikat Das. "Interpretable machine learning tools: a survey". In: *2020 IEEE Symposium Series on Computational Intelligence (SSCI)*. IEEE. 2020, pp. 1528–1534.

[47] Murat Kuzlu et al. "Gaining insight into solar photovoltaic power generation forecasting utilizing explainable artificial intelligence tools". In: *IEEE Access* 8 (2020), pp. 187814–187823.

[48] AC Fitch et al. “Local and mesoscale impacts of wind farms as parameterized in a mesoscale NWP model”. In: *Mon Weather Rev* 140.9 (2012), pp. 3017–3038.

7

Will there be more 'Dunkelflaute' Events in the Near Future?

The decarbonization plan in European countries, aiming at alleviating climate change, promotes the development of renewable power, which can itself be impacted by a changing climate. A low level of renewable power production during unfavorable weather conditions, such as 'Dunkelflaute' (simultaneous calm and cloudy periods), will significantly challenge grid stability; such behavior requires in-depth research. Here we present the first evaluation of potential climate change impacts on periods of Dunkelflaute. An unsupervised deep-learning framework (named WISRnet) is improved to cluster projected wind speed and insolation. Specifically, we encode spatial weather patterns taken from an ensemble of five EURO-CORDEX climate simulations for 2010-2050. The encoded patterns are then used for country-dependent clustering, where five clusters out of twenty-five are closely related to Dunkelflaute events. By analyzing these clusters focusing on Belgium and then the UK, a decreasing trend in the occurrence of Dunkelflaute is seen for the negative-emission scenario of RCP2.6, while there is a robust growth of Dunkelflaute occurrence in the RCP4.5 and RCP8.5 scenarios. The expected growing occurrence of Dunkelflaute periods in the future could challenge grid operators and necessitate taking an increase in such events into account in future power system plans and design.

7.1 Introduction

Given the carbon reduction targets, European power systems are incorporating increasing shares of renewable power production. In 2017, 17.5% of European energy consumption came from renewable sources [1], while the magnitude is projected to grow to at least 32% and 66% by 2030 [2] and 2050 [3], respectively. With such high penetration of renewable energies (like wind and solar power) in the power grid, the power supply will have a growing dependence on meteorological conditions [4, 5]. Therefore, extreme weather conditions which impact renewable production could have significant consequences on the stability of the future power grid. Dunkelflaute [6, 7, 8, 9, 10] is such an extreme event, which causes simultaneous low levels of wind and solar power production. In a study of the brief climatology of Dunkelflaute in northern European countries using historical wind and solar power production data, Li et al. [10] found that Dunkelflaute events happened frequently in winter and multiple events existed longer than one day. With the increasingly important roles of renewables, this extreme weather and the related adverse effects will likely become more and more detrimental. Therefore, it is important to quantify the trend in Dunkelflaute event occurrences in future climate scenarios.

A changing climate can influence the large to regional-scale circulations [11, 12], and thus the near-surface wind and solar resources can be affected [13, 14]. The impacts of climate change on wind and solar power production have been investigated in many previous studies [15, 16, 17, 18], and the overall results are limited and negative. The projected decrease in wind and solar power production can be between 0-10% over Europe, with a larger reduction northward for solar power [18, 19], and southward for wind power [15, 20, 21]. Jerez et al. [22] looked at the combined response of wind and solar power generation to climate change. A reverted annual cycle of these two power production was shown, and their temporal changes in projected scenarios are lower than 5%. Furthermore, certain studies investigated the seasonal variability of wind and solar resources under future climate conditions. One study showed a projected 3-5% decrease in solar generation in winter compared with a negligible increase in summer in Europe [23], as well as decreased wind speed in winter but increased in summer in the Mediterranean area [24]. These projected trends of wind and solar power in winter are of great interest since Dunkelflaute events have been shown to mainly occur in winter [10]. However, will there be more simultaneous windless and cloudy periods in future winters, and what impact could climate change have on the occurrence of Dunkelflaute events in Europe? These questions remained as yet unanswered.

The core purpose of this work is to shed light on climate change impacts on the occurrence of Dunkelflaute events. Climate models have been widely used to explore the future climate under different emission scenarios. Regional climate models (RCMs) are commonly applied on the regional scale to downscale the simulated domains of global climate models (GCMs) [13]. The framework of the Coordinated Regional Climate Downscaling Experiment (CORDEX) consists of many RCM simulations all over the World. The European branch of CORDEX, the EURO-CORDEX framework (http://www.euro-cordex.net), simulates an ensemble of European climate projections. It uses a relatively high resolution (12.5 km for EUR-11) and has shown to be useful in assessing the impacts of a changing climate on wind and solar variables [15, 18, 25]. However, many studies have found several types of uncertainty in the projected results for wind and solar variables resulting from

the choice of climate models [20, 23, 24]. To address the uncertainties, some researchers used an ensemble including different boundary conditions and modeling approaches [26, 27, 28]. Likewise, we here consider an ensemble of five global-regional climate simulations under the Representative Concentration Pathway (RCP) 2.6, RCP4.5, and RCP8.5 scenarios to investigate future changes of Dunkelflaute occurrence and evaluate the relevant uncertainties.

Meteorological data like wind speed and insolation from climate models are usually used to estimate climate effects on wind and solar power [23, 29]. However, utilizing these meteorological data to derive wind power data is usually complex, especially when extrapolating surface wind speed to a higher level [30, 31] and obtaining realistic power curves. The case is similar for solar power, whose calculation requires surface irradiance and temperature as inputs to a power curve [18, 23].

The unsupervised data-driven WiSRnet model described in [32] provides an opportunity to directly identify Dunkleflaute events from wind speed and insolation data. The WISRnet model uses a deep convolutional neural network(CNN)-based autoencoder (AE) to encode the inputted patterns of wind speed and insolation. The encoded two-dimensional patterns are clustered using an improved k-means method for further region-dependent identification of Dunkelflaute events. A detailed review of machine learning algorithms is provided in [32].

In this work, the WiSRnet framework is improved and used to investigate the occurrence of Dunkelaute events from future climate change time series projections. This is the first study to assess the occurrence of Dunkelflaute events given a changing climate. Dunkelflaute occurrence under different pathways of future climate forcing using various climate models is evaluated. This analysis is significant for future power systems with high penetrations of renewable power.

The paper is structured as follows. In Section 2, we describe the climate data and the methodologies applied in this work. Section 3 documents the results of weather pattern clustering and the occurrence of Dunkelflaute events in Belgium under different future projections. The uncertainties under different projections are also discussed. Section 4 presents a similar analysis for the UK. Finally, we summarise our conclusions in Section 5.

7.2 Data and Methodology

7.2.1 Climate Data

In this paper, projected climate data from the EURO-CORDEX framework is used. Covering the European domain, EURO-CORDEX has a grid resolution of approximately 12.5 km (0.11°) and a temporal interval of three hours. Here we use an ensemble of data from five EURO-CORDEX global-regional models (GCM-RCM). As shown in Table 7.1, the ensemble consists of three RCMs, including SMHI-RCA4 (named RCA4 hereafter) [33], KNMI-RACMO22E (named RACMO22E hereafter) [34], and DMI-HIRHAM5 model (named HIRHAM5 hereafter) [35]. They are driven by three GCMs, namely MPI-M-MPI-ESM-LR, EC-EARTH, and HadGEM2-ES, to obtain the lateral boundary conditions. The five GCM-RCM simulations listed in Table 7.1 are abbreviated as RMMM, 0HE, 1REE, 2RH, and 3REE, respectively.

The RCM simulations mainly cover the North Sea and the bordering countries (see

Table 7.1: List of climate simulations used in this study.

abbr.	Institution	RCM	GCM driving run
RMMM	Swedish Meteorological and Hydrological Institute	RAC4	MPI-M-MPI-ESM-LR (r1i1p1) run at the Max Planck Institute for Meteorology (MPI-M)
0HE	Danish Meteorological Institute	HIRHAMS	EC-EARTH (r1i1p1) run at the Irish Centre for High-End Computing (ICHEC)
1RE	Swedish Meteorological and Hydrological Institute	RAC4	EC-EARTH (r1i1p1) run at the Irish Centre for High-End Computing (ICHEC)
2RH	Swedish Meteorological and Hydrological Institute	RAC4	HadGEM2-ES (r1i1p1) run at Met Office Hadley Centre (MOHC)
3REE	Royal Netherlands Meteorological Institute	RACMO22E	EC-EARTH (r1i1p1) run at the Irish Centre for High-End Computing (ICHEC)

'Input' part in Figure 7.1) since this area is expected to have a large number of ongoing and proposed wind farm installations. These simulations have consistent domains with 192 × 192 latitude-longitude grid points. The weather data for 10-m wind speed and surface downward solar radiation are archived from all simulations spanning over 40 years for the period 2010-2050. The insolation data are pre-processed to have the same temporal resolution as the wind speed. All the simulations were developed under the RCP8.5 scenario, except the RMMM simulation which is also forced by another two emission scenarios, RCP4.5 and RCP2.6. These three RCP scenarios represent different levels of greenhouse gas emission causing a radiative forcing of 8.5, 4.5, 2.6 W/m^2 in 2100, which represent strong, stabilized, and negative emission scenarios, respectively.

7.2.2 Methodology

The WiSRnet framework, which is a data-driven automated classification algorithm using wind speed and insolation data, was proposed by Li et al. [32]. There are two steps in the framework: spatial pattern extraction using a deep-CNN-based autoencoder and; weather pattern clustering centering over a certain country or region. It has been demonstrated to be effective as most observed Dunkeflaute periods are successfully categorized into Dunkelflaute clusters for the country of interest [32]. The WiSRnet framework is improved in this study and used to identify future Dunkelflaute events based on climate projection data from EURO-CORDEX. It should be noted that the grid resolution for EURO-CORDEX (about 12.5km) is different to that for for ERA5 (about 31km). This means that the input used in this study has 192 × 192 grid points as opposed to a previous study using ERA5 which used 128 × 64 latitude-longitude grid points [32].

The improved WiSRnet framework used in this work is shown in Figure 7.1. For the first step of the WiSRnet framework, an asymmetric CNN-based autoencoder (CNN-AE) is used to extract the inputted fields for further classification. Wind speed and insolation

fields are first inputted to the encoder individually, comprising seven convolutional layers and three max-pooling layers. The output of the encoder is a two-dimensional bottleneck layer with a dimension of 24 × 24, which is important in capturing both the magnitude and spatial information in the inputted weather patterns. The encoded patterns are then linked to the decoding part to recreate the original weather fields. The decoder includes two fully-connected (FC) layers, five convolutional layers and three up-pooling layers to reconstruct input weather patterns. To examine the accuracy of this CNN-AE model, we use the root-mean-squared error (RMSE) as a loss function.

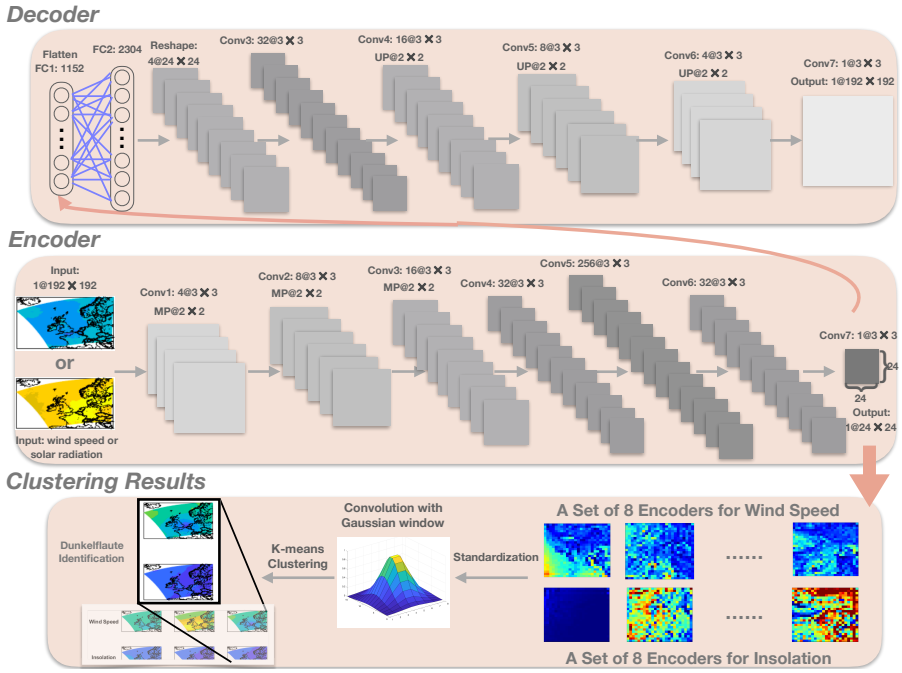

Figure 7.1: Schematic of the proposed architecture for the weather pattern clustering. The inputted variables of wind speed (in units of m/s) and insolation (in units of W/m^2) have a size of 192 × 192. The encoder consists of 7 convolutional layers that have 4, 8, 16, 32, 256, 32, and 1 filter, respectively. Each filter has a kernel size of 3 × 3. Each convolutional layer is followed by a ReLU layer and max-pooling (MP) layer for the first three layers (filter size of 2 × 2). The down-scaled encoder is connected to a decoder part to reconstruct the inputted data. The decoding model consists of two fully connected (FC) layers, five convolutional layers, and three up-pooling (UP) layers. The encoded pattern (i.e., bottleneck layer) has a size of 24 × 24. Many sets including eight bottleneck layers for wind and solar patterns are first normalized using a standard scaling (by removing the mean and scaling to unit variance) and then convolved with a Gaussian window centered on the location of interest. Finally, the k-means clustering algorithm is used for the clustering of weather patterns.

The second step of the WiSRnet framework is weather pattern clustering utilizing the encoded patterns. The encoded patterns are first normalized and then convolved with a two-dimensional Gaussian kernal centered over a specific country to achieve a region-dependent clustering. Subsequently, the convolved patterns are used for k-means clustering. Instead of directly clustering hourly data as in [32], here we improve the method

by clustering 24-hour data at one time to pay more attention to the long-lasting events. We achieve this by clustering the maximum of every successive eight samples (3-hourly). In this way, the inputted weather patterns are clustered into 25 clusters for the country of interest.

For the training of the AE, we use 40-year data from the RMMM simulation for all three RCP scenarios. To assess the accuracy of the CNN-AE model, data are divided into a training set, a validation set and a test set consisting of the first 60%, 10%, and the last 30% of samples, respectively. Each set for the individual RCP scenarios is concatenated together and fed into the autoencoder. In the implementations, we use the Adam (adaptive moment estimation) optimizer [36] with maximum epochs of 50 and a batch size of 128. A detailed description of the implementations, performance comparisons and optimizations are provided in [32].

The RMSE of the input minus the reconstructed wind speed and insolation grid point values for the training, validation and test sets from the RMMM simulation are listed in Table 7.2. The accuracy is similar to [32] based on ERA5 reanalysis data. The framework is then inferenced using data from the 0HE, 1RE, 2RH, and 3REE models. As seen in Table 7.2, the accuracy is similar.

Table 7.2: RMSE of the input minus the reconstructed wind speed and insolation values over all grid points for the different climate simulations.

Variable	**Wind Speed (m/s)**						
Model	**RMMM - 3RCP Scenarios**			**0HE**	**1RE**	**2RH**	**3REE**
Dataset	**train**	**validation**	**test**	**all**	**all**	**all**	**all**
RMSE	0.7708	0.7749	0.7712	0.90	0.77	0.77	0.87
Variable	**Insolation(W/m^2)**						
RMSE	25.50	25.77	25.16	25.14	25.41	25.02	24.47

Finally, all the encoded patterns from the five simulations are clustered together centered over the country of interest, namely, Belgium and the UK in this study. The several clusters that are most characteristic of long-lasting Dunkelflaute periods will be studied in the next section.

7.3 Results: Trend of Dunkelflaute Occurrence centered over Belgium

7.3.1 Weather Pattern Clustering Centered over Belgium

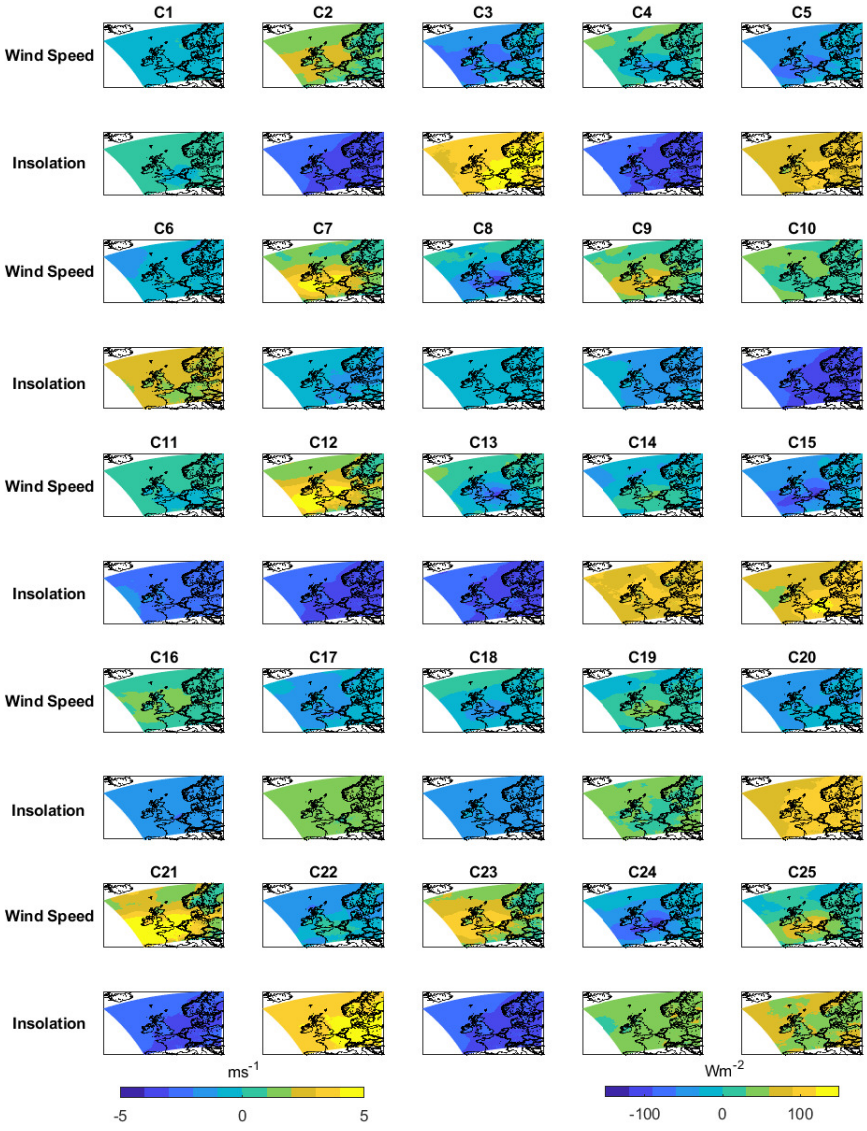

Figure 7.2: Anomalies of wind speed and insolation based on the 40-year mean for the 25 clusters (C1–C25) using the RMMM simulation (RCP4.5 scenario). The Gaussian kernel is centered on Belgium.

In Figure 7.2, we show the clustering results of the weather patterns with the Gaussian weighting kernel first centered on Belgium. Taking the RMMM simulation (RCP4.5 scenario) as an example, the mean wind speed and insolation anomalies are calculated based on the 10-year mean values for all 25 clusters. These clusters show different distributions of wind speed and insolation with a clear focus over the Belgian area.

It is visually clear that the C4, C13, C18 clusters are the most representative of Dunkelflaute with quite low wind speed and insolation over the Belgian onshore and offshore areas. Thus these three clusters are the 'Top3' Dunkelflaute candidate clusters (named 'Top3-DF clusters'). Furthermore, though with marginally larger anomalies of wind speed, the C10 and C11 clusters also exhibit typical Dunkelflaute characteristics. Therefore, these five clusters are considered the 'Top5' suitable candidates for Dunkelflaute clusters (named as 'Top5-DF clusters').

In Table 7.3, we list the number and fraction of samples in each cluster, as well as the mean wind speed (named mean WS) and insolation (named mean SR) for the 25 clusters. The Top5-DF clusters visually identified before are shown in bold. These five clusters have the lowest mean wind speed and insolation as expected. For the Top3-DF clusters, the mean wind speed is especially low at less than 3.5m/s. For the C10 and C11 clusters, the mean wind speed slightly increases but is still lower than 5m/s. The mean insolation for these five clusters is quite low with values lower than 90 W/m^2. These Top3 and Top5 Dunkelflaute clusters account for about 12% and 21% of all the samples, respectively.

Table 7.3: Information for the 25 clusters (C1–C25). The clustering is based on the RMMM simulation (RCP4.5 scenario) and the Gaussian weight function is centered on Belgium.WS=wind speed (in m/s); SR=insolation (in W/m^2).

Clusters	**C1**	**C2**	**C3**	**C4**	**C5**	**C6**	**C7**
Number	6805	5892	4410	**4700**	6210	6442	1908
Fraction	0.0582	0.0504	0.0377	**0.0402**	0.0531	0.0551	0.0163
Mean WS	4.3591	6.2277	3.4981	**3.4330**	3.0677	4.4888	8.3381
Mean SR	116.75	33.91	295.05	**37.58**	230.07	180.24	95.17
Clusters	**C8**	**C9**	**C10**	**C11**	**C12**	**C13**	**C14**
Number	3806	4782	**5093**	**5891**	2882	**3749**	3686
Fraction	0.0326	0.0409	**0.0436**	**0.0504**	0.0247	**0.0321**	0.0315
Mean WS	2.1800	6.7628	**4.9426**	**4.2314**	8.6898	**2.2017**	5.4116
Mean SR	113.28	85.69	**32.44**	**59.50**	30.90	**44.76**	221.01
Clusters	**C15**	**C16**	**C17**	**C18**	**C19**	**C20**	**C21**
Number	4557	6215	7820	**5667**	5974	5646	1016
Fraction	0.0390	0.0532	0.0669	**0.0485**	0.0511	0.0483	0.0087
Mean WS	2.2227	5.4927	3.3196	**3.2013**	5.6380	4.0885	10.1700
Mean SR	269.33	72.30	160.07	**85.20**	142.22	238.08	36.16
Clusters	**C22**	**C23**	**C24**	**C25**			
Number	1932	4846	4973	1970			
Fraction	0.0165	0.0415	0.0426	0.0169			
Mean WS	4.8548	7.4223	2.0955	6.9653			
Mean SR	296.53	34.37	181.58	181.13			

Figure 7.3 shows the probability density function (PDF) for the Top5-DF clusters at the location of the geographical center of Belgium. Nearly all the samples in the Top3-DF clusters have wind speeds lower than 5m/s, and lower than 7 m/s for the Top5-DF clusters. Concerning the PDF of insolation, the majority of samples are in the range 0-100 W/m^2, at most reaching approximately 200 W/m^2. This confirms the findings in [32] that Top3-DF clusters are reliable indicators of Dunkelflaute events.

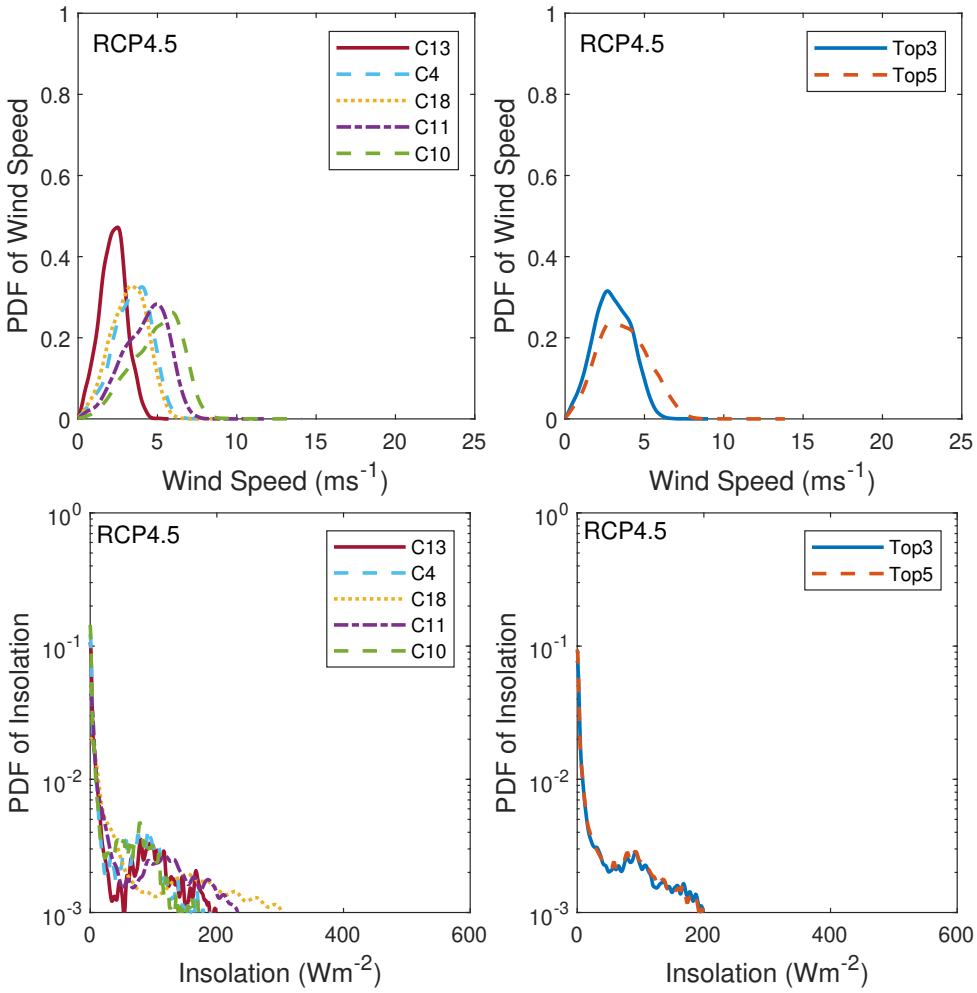

Figure 7.3: Probability density function (PDF) of wind speed (top-left panel) and isolation (bottom-left panel) for the individual Top5-DF clusters, specifically, the 13th, 4th, 18th, 11th, and 10th cluster. The PDF of wind speed (top-right panel) and isolation (bottom-right panel) for Top3-DF and Top5-DF clusters together are also displayed. These plots are for the RMMM model.

7.3.2 Dunkelflaute Event Occurrence under Different RCP Scenarios

Based on the weather pattern clustering, we use the Top3-DF and Top5-DF clusters to examine how frequently Dunkelflaute events occur during the period 2010 to 2050 under different RCP scenarios. The top panel of Figure 7.4 shows the frequency of the Dunkelflaute events from the RMMM simulations forced by the RCP4.5 emission scenario. We can see a possible growing tendency for samples in both Top3-DF and Top5-DF clusters for the period 2010-2050. The bottom panels of Figure 7.4 show the frequency of Dunkelflaute events for the RMMM simulation forced by the RCP8.5 and RCP2.6 emissions scenarios for the period 2010 to 2050. For the RCP8.5 scenario, the number of samples in the Top3-DF and Top5-DF clusters also show a possible increasing, similar to the RCP4.5 scenario. In contrast, the frequency of Dunkelflaute samples for the RCP2.6 scenario is possibly declining. It can thus be speculated that the future occurrence of Dunkelflaute periods can be closely related to pathways of future climate forcing. A low emission scenario, like RCP2.6, can lead to a reduced number of Dunkelflaute periods in the near future. In contrast, a high level of greenhouse gas emission instead will boost the occurrence of Dunkelflaute events and become an increasing concern for the power grid.

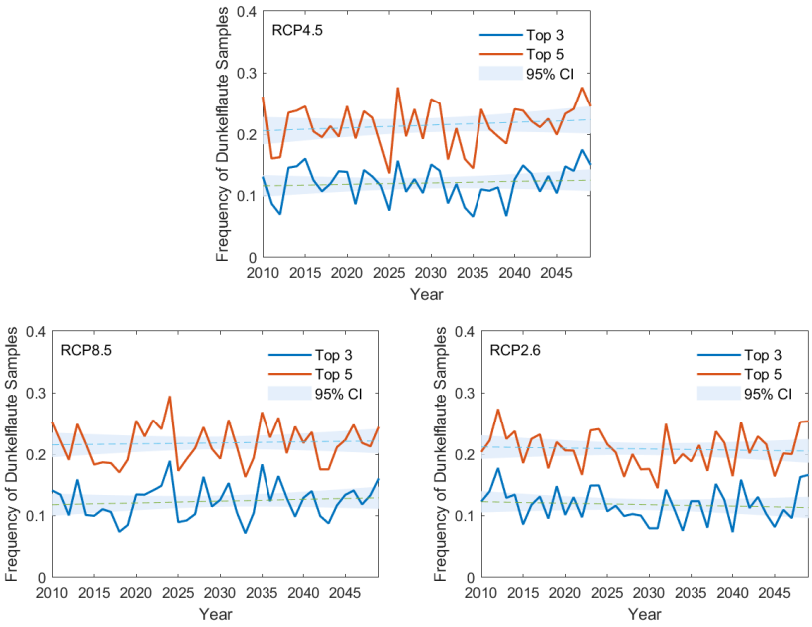

Figure 7.4: Frequency of Dunkelflaute events in the Top3-DF and Top5-DF clusters for the period 2010-2050. The dash lines and the light blue band represent linear trends and 95% confidence interval (labeled as 95% CI), respectively. The clustering is based on the RMMM simulation (RCP4.5 scenario for the top panel, RCP8.5 for the bottom left panel and RCP 2.6 for the bottom right panel) and the Gaussian weight function is centered on Belgium.

7.3.3 Variation in Dunkelflaute Event Occurrence for Different Models

As mentioned above, in addition to clustering Dunkelflaute events from the RMMM simulation forced by three RCP scenarios, events were also clustered according to four additional model simulations: 0HE, 1RE, 2RH, and 3REE forced by the RCP8.5 scenario to investigate model variability. Taking the 0HE simulation as an example, the anomalies of wind speed and insolation for the Top5-DF clusters are shown in Figure 7.5. Similar to the clustering results in Figure 7.2 for the RMMM RCP8.5 simulation, the C13, C4, and C18 clusters also show characteristics of Dunkelflaute. The results are similar for the 1RE, 2RH, and 3REE simulations (maps not shown here).

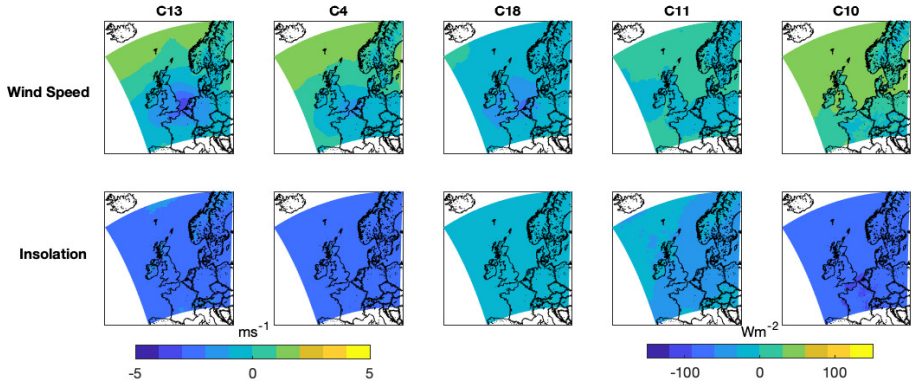

Figure 7.5: Anomalies of wind speed and insolation based on the 40-year mean for the Top5-DF clusters using the 0HE simulation (RCP8.5 scenario). The Gaussian kernel is centered on Belgium.

Based on the weather pattern clustering, the frequency of Dunkelflaute occurrence for the 0HE, 1RE, 2RH, and 3REE simulations (forced by RCP8.5 scenario) is presented in Figure 7.6. Among all the models, the possible growth of Dunkeflaute frequency is similar for the 0HE, 1RE, and 2RH models, while the 3REE model results show a clear increasing. The magnitude for the 0HE model is remarkably higher, as it grows from around 14% in 2010 to 18% in 2050.

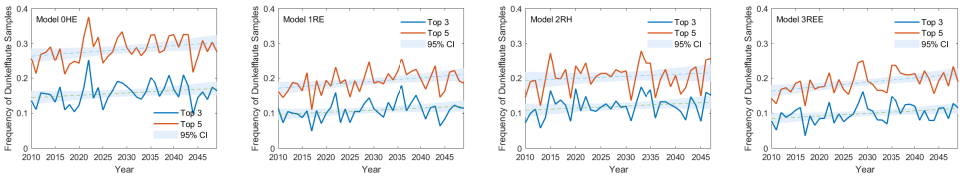

Figure 7.6: Frequency of Dunkelflaute events in the Top3-DF and Top5-DF clusters for the period 2010-2050. The dash lines and the light blue band represent linear trends and 95% confidence interval (labeled as 95% CI), respectively. The clustering is based on four models of 0HE, 1RE, 2RH, and 3REE (RCP8.5 scenario).

7.4 Dunkelflaute Occurrence over the UK

7.4.1 Weather Pattern Clustering Centered over the UK

The proposed framework can also be used for other countries to identify Dunkelflaute periods. Anomalies of wind speed and insolation for the five most representative clusters identified as Dunkelflaute over the UK (Top5-DF clusters) are shown in Figure 7.7. The clustering is based on the RMMM simulation (RCP4.5 scenario) and the Gaussian kernel is centered on the UK. For the Top5-DF clusters, specifically, the C11, C14, C23, C1, and C19 clusters, low winds speeds and low insolation can be seen over the UK.

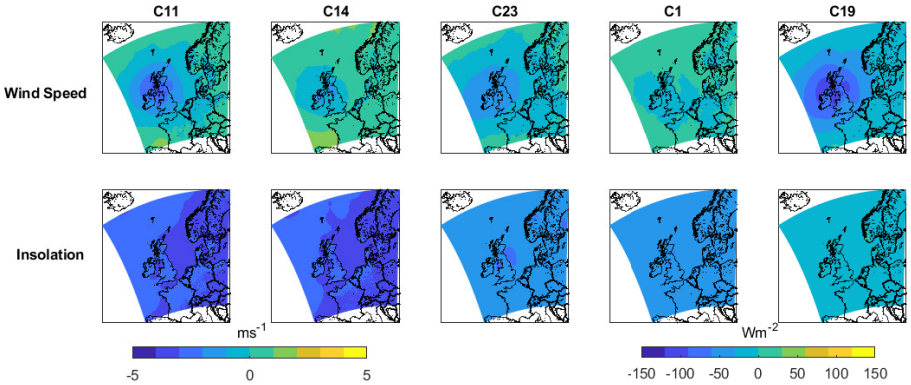

Figure 7.7: Anomalies of wind speed and insolation based on the 40-year mean for the Top5-DF clusters using the RMMM simulations (RCP4.5 scenario). The clustering is centered over the UK.

7.4.2 Dunkelflaute Event Occurrence under Different RCP Scenarios

With the Gaussian kernel centered over the UK, the clustering is implemented on the decoded weather patterns for the RMMM simulation (forced by three RCP scenarios) and the other four simulations, 0HE, 1RE, 2RH, and 3REE (forced by RCP8.5 scenario). The Dunkelflaute occurrence for different RCP scenarios is shown in Figure. 7.8. There is a possible reduction in the frequency of Dunkelflaute occurrence across the 40 years if the RMMM simulation is driven by the RCP2.6 scenario, whereas contrasting results are seen for the higher RCP scenarios. The possible increasing trends of Dunkelflaute frequency for the RCP4.5 and RCP8.5 scenarios collaborate with the previous findings in Belgium. It confirms our inference that a higher level of greenhouse gas emission can foster the occurrence of Dunkelflaute events in the future.

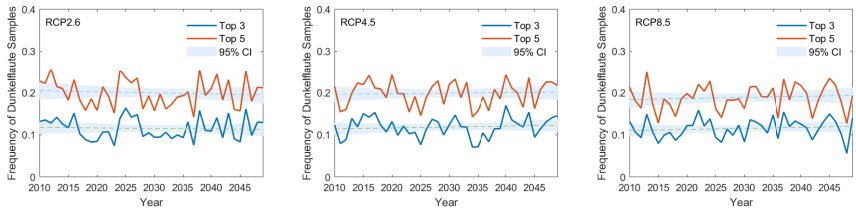

Figure 7.8: Frequency of Dunkelflaute events in the Top3-DF and Top5-DF clusters for the period 2010-2050. The dash lines and the light blue band represent linear trends and 95% confidence interval (labeled as 95% CI), respectively. The clustering is based on the RMMM simulation (RCP4.5, RCP8.5 and RCP 2.6 scenarios). The Gaussian kernel is centered on the UK.

When forced by the RCP8.5 scenario, the other three models show a greater increase than the RMMM. The 0HE and 3REE models suggest significant substantial increases for both the Top3-DF and Top5-DF clusters, while the 1RE and 2RH models exhibit relatively steady growth in the Dunkelflaute frequency.

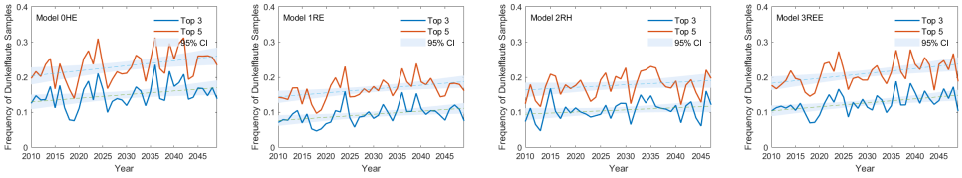

Figure 7.9: Same as Fig 7.6, except that the clustering is centered over the UK.

7

7.5 Concluding Remarks

In this paper, an unsupervised deep learning methodology (WiSRnet) is used to identify Dunkelflaute events from future climate simulations using wind speed and insolation fields. We improve the WiSRnet framework to cluster the weather patterns in both temporal and spatial dimensions, with the focusing area centered over Belgium and the UK. Based on the weather pattern clustering, we identify the top-3 and top-5 clusters closely related to Dunkelflaute periods.

Using the RMMM model, a positive trend in Dunkelflaute frequency is seen for the RCP4.5 and RCP8.5 emission scenarios, while a negative trend is seen for the RCP2.6 emission scenario, however, these trends are not statistically significant given the inter-annual variation. When an ensemble of four further models are forced using the RCP8.5 scenario, all models indicate an increase in the occurrence of Dunkelflaute for Belgium and the UK but this trend is not significant for all models.

A higher occurrence of Dunkelflaute events in the future, may require additional flexibility and storage requirements for a grid with a high penetration of renewables and this risk should be included in the future design and planning of power systems.

In this study, an ensemble of five climate model projections gave insights into the expected effects of climate change on Dunkelflaute. It is tentatively suggested by the models that Dunkelflaute events may increase in the future over Northern Europe, however,

the trends are not always significant given interannual variability. A wider range of global and regional climate projections should be used to improve the reliability of this analysis.

References

[1] European commission Eurostat. *Share of energy from renewable sources*. https://appsso.eurostat.ec.europa.eu/nui/show.do?dataset=nrg_ind_ren&lang=en. Accessed: 2021-11-22.

[2] Commission European. *Report from the Commission to the European Parliament, the Council, the European Economic and Social Committee and the committee of the regions on the implementation of EU macro-regional strategies*. Tech. rep. Technical Report. https://eur-lex.europa.eu/legal-content/EN/TXT/?uri=COM:2019:21:FIN. Accessed June 19, 2019. European Commission. Brussels, 2019.

[3] European Commission. "Energy Roadmap 2050". In: (2012), pp. 1–20.

[4] Hannah C Bloomfield et al. "Quantifying the increasing sensitivity of power systems to climate variability". In: *Environmental Research Letters* 11.12 (2016), p. 124025.

[5] FJ Santos-Alamillos et al. "Analysis of spatiotemporal balancing between wind and solar energy resources in the southern Iberian Peninsula". In: *Journal of applied meteorology and climatology* 51.11 (2012), pp. 2005–2024.

[6] Frank Meinke-Hubeny et al. "Energy transition in Belgium–Choices and costs". In: *EnergyVille in Opdracht van Febeliec: Genk, Belgium* (2017).

[7] D Wetzel. "Die „Dunkelflaute "bringt Deutschlands Stromversorgung ans Limit". In: *Die Welt "vom* 6 (2017). https://www.welt.de/wirtschaft/article161831272/Die-Dunkelflaute-bringt-Deutschlands-Stromversorgung-ans-Limit.html. Accessed December 18, 2021., p. 2017.

[8] Bowen Li et al. "Quantifying the predictability of a 'Dunkelflaute'event by utilizing a mesoscale model". In: *Journal of Physics: Conference Series*. Vol. 1618. 6. IOP Publishing. 2020, p. 062042.

[9] Bowen Li et al. "Mesoscale modeling of a "Dunkelflaute" event". In: *Wind Energy* 24.1 (2021), pp. 5–23.

[10] Bowen Li et al. "A brief climatology of dunkelflaute events over and surrounding the North and Baltic Sea areas". In: *Energies* 14.20 (2021), p. 6508.

[11] Ryo Mizuta. "Intensification of extratropical cyclones associated with the polar jet change in the CMIP5 global warming projections". In: *Geophysical Research Letters* 39.19 (2012).

[12] Richard Davy and Igor Esau. "Differences in the efficacy of climate forcings explained by variations in atmospheric boundary layer depth". In: *Nature Communications* 7.1 (2016), pp. 1–8.

[13] Sara C Pryor and RJ Barthelmie. "Climate change impacts on wind energy: A review". In: *Renewable and sustainable energy reviews* 14.1 (2010), pp. 430–437.

[14] Martin Wild et al. “Projections of long-term changes in solar radiation based on CMIP5 climate models and their influence on energy yields of photovoltaic systems”. In: *Solar Energy* 116 (2015), pp. 12–24.

[15] Isabelle Tobin et al. “Climate change impacts on the power generation potential of a European mid-century wind farms scenario”. In: *Environmental Research Letters* 11.3 (2016), p. 034013.

[16] Idar Barstad, Asgeir Sorteberg, and Michel dos-Santos Mesquita. “Present and future offshore wind power potential in northern Europe based on downscaled global climate runs with adjusted SST and sea ice cover”. In: *Renewable Energy* 44 (2012), pp. 398–405.

[17] Julia A Crook et al. “Climate change impacts on future photovoltaic and concentrated solar power energy output”. In: *Energy & Environmental Science* 4.9 (2011), pp. 3101–3109.

[18] Sonia Jerez et al. “The impact of climate change on photovoltaic power generation in Europe”. In: *Nature communications* 6.1 (2015), p. 10014.

[19] Johannes Müller et al. “CMIP-5 models project photovoltaics are a no-regrets investment in Europe irrespective of climate change”. In: *Energy* 171 (2019), pp. 135–148.

[20] Isabelle Tobin et al. “Assessing climate change impacts on European wind energy from ENSEMBLES high-resolution climate projections”. In: *Climatic Change* 128 (2015), pp. 99–112.

[21] J Scott Hosking et al. “Changes in European wind energy generation potential within a 1.5 C warmer world”. In: *Environmental Research Letters* 13.5 (2018), p. 054032.

[22] S Jerez et al. “Future changes, or lack thereof, in the temporal variability of the combined wind-plus-solar power production in Europe”. In: *Renewable Energy* 139 (2019), pp. 251–260.

[23] HC Bloomfield et al. “Quantifying the sensitivity of european power systems to energy scenarios and climate change projections”. In: *Renewable Energy* 164 (2021), pp. 1062–1075.

[24] Erik Kjellstro
M et al. “21st century changes in the European climate: uncertainties derived from an ensemble of regional climate model simulations”. In: *Tellus A: Dynamic Meteorology and Oceanography* 63.1 (2011), pp. 24–40.

[25] Daniela Jacob et al. “EURO-CORDEX: new high-resolution climate change projections for European impact research”. In: *Regional environmental change* 14.2 (2014), pp. 563–578.

[26] Mark Reyers, Julia Moemken, and Joaquim G Pinto. “Future changes of wind energy potentials over Europe in a large CMIP5 multi-model ensemble”. In: *International Journal of Climatology* 36.2 (2016), pp. 783–796.

[27] Julia Moemken et al. “Future changes of wind speed and wind energy potentials in EURO-CORDEX ensemble simulations”. In: *Journal of Geophysical Research: Atmospheres* 123.12 (2018), pp. 6373–6389.

[28] Yuchen Yang, Kavan Javanroodi, and Vahid M Nik. "Climate Change and Renewable Energy Generation in Europe—Long-Term Impact Assessment on Solar and Wind Energy Using High-Resolution Future Climate Data and Considering Climate Uncertainties". In: *Energies* 15.1 (2022), p. 302.

[29] I Koletsis et al. "Assessment of offshore wind speed and power potential over the Mediterranean and the Black Seas under future climate changes". In: *Renewable and Sustainable Energy Reviews* 60 (2016), pp. 234–245.

[30] Roland B Stull. *An introduction to boundary layer meteorology*. Vol. 13. Springer Science & Business Media, 1988.

[31] Richard Davy et al. "Climate change impacts on wind energy potential in the European domain with a focus on the Black Sea". In: *Renewable and sustainable energy reviews* 81 (2018), pp. 1652–1659.

[32] Bowen Li, Sukanta Basu, and Simon J Watson. "Automated Identification of "Dunkelflaute" Events: A Convolutional Neural Network–Based Autoencoder Approach". In: *Artificial Intelligence for the Earth Systems* 1.4 (2022), e220015.

[33] Gustav Strandberg et al. *CORDEX scenarios for Europe from the Rossby Centre regional climate model RCA4*. SMHI, 2015.

[34] KNMI. *cordex EUR-11 KNMI RACMO22E (This data has been retracted)*. http://cera-www.dkrz.de/WDCC/ui/Compact.jsp?acronym=CXEU11KNRA_retr. 2017.

[35] Ole Bøssing Christensen et al. "The HIRHAM regional climate model. Version 5 (beta)". In: (2007).

[36] Diederik P Kingma and Jimmy Ba. "Adam: A method for stochastic optimization". In: *arXiv preprint arXiv:1412.6980* (2014).

8

Conclusion

8.1 Conclusion

Dunkelflaute events are extreme weather conditions with dramatically reduced renewable power production, which can significantly challenge grid stability. This dissertation concentrates on three aspects to better understand the behavior of Dunkelflaute events and develop physical and ML approaches for its prediction. They are 1) to statistically analyze the frequency, length, seasonal, and spatial characteristics of Dunkelflaute events; 2) to develop different identification and prediction strategies from using models and data in order to improve the predictability of Dunkelflaute events; 3) to detect potential changes in the occurrence of Dunkelflaute in a changing climate. The research sub-questions raised in Chapter 1 have been addressed accordingly.

Q1: What is the frequency, duration, driver, and spatial coherence of Dunkelflaute in Northern Europe?

Chapter 2 provides the answers to the research question Q1. In this chapter, a statistical analysis of Dunkelflaute events in eleven countries in Northern Europe was conducted. By using simulated power production data from Renewables.ninja, as well as actual data from TSOs, the frequency, length, and seasonality of Dunkelflaute were characterized. By using the ERA5 reanalysis dataset, the meteorological drivers giving rise to Dunkelflaute events were identified. A simple assessment of impact on the grid was made which provides insight into maintaining system stability during Dunkelflaute. The main conclusions are summarized as follows:

- By classifying Dunkelflaute events with both wind and solar capacity factors below 0.2 and duration longer than 1h, approximately 5-10 events every year persisted for more than 1 day in Germany, Norway, and the UK. Several events were found to last up to 5 days. The season with this most frequent Dunkelflaute is winter, with 50-100 hours of events each month.

- Through characterizing weather patterns, large stationary high-pressure systems and widespread low cloud coverage are typically associated with Dunkelflaute. Blocked regimes originating from extensive high-pressure systems can prevent oceanic airflow into Northern Europe countries, and reduce wind power production.

- No strong relationships were found of Dunkelflaute between neighboring countries. Due to this low dependency, the interconnection of European grid systems could significantly reduce the impact of Dunkelflaute.

Q2: Can we automatically identify Dunkelflaute events using publicly available meteorological data instead of limited power data?

Chapter 3 provides the answer to the research question Q2. In this chapter, an unsupervised deep learning framework, namely WISRnet, is proposed with two important components, a CNN-AE model for downscaling weather patterns and a region-based k-means model for automatically clustering the Dunkelflaute related patterns. This deep

learning strategy has been validated through aggregated wind and solar power production data from Belgium. The main conclusions are summarized as follows:

- The CNN-AE model downscales the spatial wind speed and insolation patterns with low learning errors, which is effective in extracting internal features and encapsulating spatial information for further clustering.
- The k-means clustering model assisted by a Gaussian convolutional kernel is effective in clustering weather patterns concentrated on one specific region. This enables WISRnet to identify Dunkelflaute events in different countries.
- The WISRnet approach has demonstrated its capability to identify Dunkelflaute events from weather patterns. A good agreement has been achieved between the Dunkelflaute labelling predicted by WISRnet and the observed events. Specially, five out of all twenty-five clusters were identified as Dunkelflaute clusters in Belgium with high true positive ratios.

Q3: Can we reliably model and predict Dunkeflaute events using a contemporary mesoscale model?

Chapter 4 provides the answer to the research question Q3. In this chapter, the WRF model is applied to simulate atmospheric conditions during Dunkelflaute. The model has been validated using a large quantity of observational data. The main conclusions are summarized as follows:

- The WRF model combined with a wind farm parameterization has demonstrated its ability to reliably reproduce and predict wind power production and insolation during Dunkelflaute periods.
- During Dunkelflaute events, the marine boundary layer was observed to be commonly well-mixed, and the boundary layer evolution is well predicted through the WRF model.
- Certain characteristics of Dunkelflaute events, such as hub-height wind speeds and power production, can be accurately modelled. For instance, a grid size of 27 km was found to be reliable in simulating these features. This could significantly reduce computational costs required for simulating such events.

Q4: Can we reliably estimate Dunkeflaute events using contemporary machine-learning methods? How is its performance compared with mesoscale models?

Chapter 5 provides the answer to the research question Q4. In this chapter, a LightGBM-based approach is proposed to estimate the wind and solar power production during Dunkelflaute events. Variables that could affect renewable power production were included for prediction, such as wind speed, insolation, boundary layer height and sensible heat flux. These variables are acquired as input at multiple locations. The main conclusions are summarized as follows:

- The LightGBM model outperformed other machine learning models, including RF and XGBoost, as well as the physical model WRF. It can provide an accurate and reliable estimation of power production during Dunkelflaute events.
- According to the spatial correlations between power data and related variables, choosing weather variables from multiple locations for model input is meaningful. Increasing the locations to two can dramatically increase model accuracy, while the addition of the third location does not improve much.
- Among the input variables, surface downward radiation flux is important for the estimation of solar power, while wind speeds, wind gusts, and boundary-layer-related parameters are important for the estimation of wind power.

Q5: What will Dunkelflaute be like in the future given climate change?

Chapter 6 provides the answer to the research question Q5. In this chapter, WISRnet is improved and used to cluster projected wind speed and insolation patterns and then identify Dunkelflaute events. Three future emission scenarios are analysed. The main conclusions are summarized as follows:

- WISRnet is effective to identify future Dunkelflaute events from projected wind speed and insolation patterns.
- The frequency of future Dunkelflaute events is dependent on future emission scenarios. For the negative emission scenario RCP2.6, Dunkelflaute frequency shows a declining trend over the period 2010-2050, while an increasing trend is seen for the RCP4.5 and RCP8.5 scenarios, abeit that the trends are not significant given the interannual variability.

8

8.2 Applications of research findings

There are multiple approaches proposed in this dissertation to reliably predict wind and solar power production during Dunkelflaute events. The following potential applications are proposed accordingly:

- WISRnet is an effective tool to identify Dunkelflaute events from wind speed and insolation patterns and has the potential to be extended to other types of weather patterns. It can be applied to different regions and countries over the world.
- The LightGBM model has the potential to forecast power production during Dunkelflaute periods using GFS data. In addition, it also has the potential to forecast grid demand.

8.3 Recommendations for future research

This dissertation provides insight into the statistical characteristics of and the prediction strategies for Dunkelflaute events. There are several recommendations for future research.

- Although some meteorological features have been observed along with Dunkelflaute events, the detailed weather conditions to evolve and form this extreme weather are unknown and should be investigated in future research.
- Many potential aspects of ML approaches have not been investigated and should be included in future research. For example, applying the WISRnet structure and feeding other weather pattern data can be used for identifying Dunkelflaute. Using ML models to predict power production with GFS data and using ML models to predict grid demand are also recommended for future researches.
- Since mesoscale and ML models are able to predict power production during Dunkelflaute, a hybrid model is worth investigation to improve the prediction performance.
- Several areas of research have been investigated to predict Dunkelflaute events. It is also important to develop strategies to handle power imbalance during such extreme weather conditions. Different strategies should be investigated regarding their cost, impact, and effectiveness.

Curriculum Vitæ

Bowen Li

1994/04	Born in Liaoning, China
Sep.2012 - July. 2016 Renewable Energy	B.SC student North China Electric Power University, China
Sep.2016 - July. 2018 Hydraulic Engineering	M.SC student Tsinghua University, China
Sep.2018 - Present Civil Enfineering and Geoscience	PhD. candidate Delft University of Technology, The Netherlands

List of Publications

1. Li, B., Basu, S., & Watson, S. J. (2022). Automated Identification of 'Dunkelflaute' Events: A Convolutional Neural Network-Based Autoencoder Approach. Artificial Intelligence for the Earth Systems, 2022 Oct;1(4):e220015.

2. Li, B., Basu, S., Watson, S. J., & Russchenberg, H. W. (2021). Mesoscale modeling of a 'Dunkelflaute' event. Wind Energy, 24(1), 5-23.

3. Li, B., Basu, S., Watson, S. J., & Russchenberg, H. W. (2021). A Brief Climatology of Dunkelflaute Events over and Surrounding the North and Baltic Sea Areas. Energies, 14(20), 6508.

4. Li, B., Basu, S., Watson, S. J., & Russchenberg, H. W. (2020, September). Quantifying the Predictability of a 'Dunkelflaute'Event by Utilizing a Mesoscale Model. In Journal of Physics: Conference Series (Vol. 1618, No. 6, p. 062042). IOP Publishing.

5. Li, B., Baohui, M., Min, G., Zhengda, D., Dongfei, W., & Chengyu, H. (2018). Water Environmental Quality Evaluation of the Karst Water in Beijing. Nature Environment & Pollution Technology, 17(2).

6. Li, B., & Baohui, M. (2016). Study on the Feasibility of Karst Water as a Source of Water Supply in Beijing. Nature Environment and Pollution Technology, 15(1), 135.

Included in this thesis.